ABSTRACTS

International Workshop on Advancing Disaster Resilience through Radio Observations 2026

12–13 November 2026
100th Anniversary Hall, UEC Alliance Center
Chofu, Tokyo, Japan

ORGANIZERS

QuakeInsight Tokyo (QIT)
and
Earth Environment Research Station,
The University of Electro-Communications (UEC)

SUPPORTED BY

Society of Atmospheric Electricity of Japan

Short-Term Prediction of Lightning and Heavy Rainfall Using MP-PAWR and LF/MF Lightning Location System

H. Kikuchi[1], Y. Hobara[2], E. Yoshikawa[3], Y. Nakamura[4], T. Morimoto[5], and T. Ushio[3]
[1] Center for Space Science and Radio Engineering, The University of Electro-Communications, Chofu, Japan
[2] Graduate School of Informatics and Engineering, The University of Electro-Communications, Chofu, Japan
[3] Graduate School of Engineering, The University of Osaka, Osaka, Japan
[4] Kobe City College of Technology, Kobe, Japan
[5] Graduate School of Science and Engineering, Kindai University, Osaka, Japan
Corresponding author: hkikuchi@uec.ac.jp

Three X-band multi-parameter phased array weather radars (MP-PAWR) have been operating in Japan. The MP-PAWR gives us a high temporal resolution, which is less than 30 sec, high-density, and dual-polarization radar observations for precipitations at high altitude as compared with a weather radar with a parabolic antenna. MP-PAWR has been developed in 2018 [1]. It can provide dual polarization variables that reveal detailed microphysics of storms. The MP-PAWR simultaneously transmits pulses of horizontal and vertical polarized waves. The center of frequency and observation range are 9.43 GHz and 60 km, respectively. Additionally, the 114 samples are observed from 0 deg to 90 deg in elevation angles. The angular resolution for the elevation angles is approximately 0.8 deg. For azimuth angles, the spatial resolution is 1.2 deg. As a result, MP-PAWR can obtain highly dense volume scan data every 30 seconds. In 2020, our research group also installed a 13 low frequency (LF)/medium frequency (MF) band sensor network to locate lightning discharges in the Kanto area in Japan. The system provides the three-dimensional locations of lightning discharges using the time-of-arrival location technique. The mean distance between stations is approximately 20–30 km. The electric field antenna bandwidth is broad from 51 Hz to 550 kHz. Its signal is sampled at 5 MHz using the universal software radio peripheral (USRP). Accurate advance prediction of lightning strikes is a crucial task for mitigating meteorological disasters.

In this study, we conducted a comparative analysis of lightning discharge locations and localized variations in polarimetric variables indicating electric field dynamics using synchronized MP-PAWR and LF/MF band lightning location system data. This study investigates a discrete thunderstorm that evolved within the observation domain on August 13, 2020, from 16:00 to 18:00 JST. The convective cell exhibited intense development, characterized by peak radar reflectivity approaching 50 dBZ. The complete life cycle of this storm—from its initial growth to its final dissipation—was continuously monitored within the coverage area of the MPPAWR. Figure 1 illustrates the concurrent data acquired by both the LF/MF Lightning location system and MPPAWR at 17:07:23 JST. Subplots (a) through (d) display the horizontal reflectivity factor (Z_h), differential reflectivity (Z_{dr}), specific differential phase (K_{dp}), and copolar correlation coefficient (ρ_{hv}), respectively. Numerical labels denote the viewing planes: "1" corresponds to the horizontal layout (maximum values mapped along the Z-axis), whereas "2" and "3" delineate the vertical profiles along the X-axis and Y-axis. For the vertical cross-sections, the Z_h (a-2, 3) and Z_{dr} (b-2, 3) fields project maximum intensities onto orthogonal surfaces. In contrast, the K_{dp} (c-2, 3) and ρ_{hv} (d-2, 3) plots illustrate slices extracted precisely along the dashed lines indicated in the panels. This methodological difference is crucial; utilizing maximum projections for these latter polarimetric variables would mask essential microphysical properties, most notably the negative K_{dp} regions. A rectangular boundary highlights the spatial domain chosen for quantifying the volume of the negative K_{dp} signature, while black markers denote the 3D spatial coordinates of lightning events tracked by the LF/MF lightning location system. To match the 30-second temporal resolution of the MP-PAWR, the plotted lightning data aggregates all discharge sources recorded during a 30-second interval immediately following the radar scan timestamp. Panels (a-1, 2, 3) reveal that the thundercloud spanned roughly 5 to 10 km horizontally. The height of the 45 dBZ contour extended up to 8 km, signifying the presence of vigorous updrafts driving the storm's growth. Electrical

activity was primarily clustered between 8 and 10 km in elevation, positioned directly above the intense reflectivity core. As seen in the (b) series panels, elevated Z_{dr} measurements (exceeding 4 dB) stretched significantly upward. This structure, widely recognized as a "Z_{dr} column," serves as a strong indicator of convective updrafts. Our observations verify that electrical discharges cluster near the apex of this column. According to subplot (c-1), the maximum K_{dp} field likewise exhibited substantial magnitudes (approaching 3 deg/km) within the actively growing sectors of the thundercloud. Cross-sections (c-2, 3) reveal that, akin to Z_h and Z_{dr}, an area of enhanced K_{dp} is located directly below the lightning initiation zones. Conversely, upper-level zones (between 8 and 14 km) feature negative K_{dp} readings (highlighted in blue) closely associated with the discharge locations. This specific zone is interpreted as an area where ice particles have oriented themselves vertically, which is the central phenomenon investigated in this paper. Finally, the ρ_{hv} data in the (d) panels indicate high correlation values where precipitation hydrometeors are present. Altogether, these findings demonstrate the successful simultaneous 3D recording of both electrical discharges and polarimetric cloud properties during the event.

These findings demonstrate the successful simultaneous 3D recording of electrical discharges and polarimetric cloud properties, elucidating the physical connections between cloud microphysics and lightning occurrences for improved forecasting.

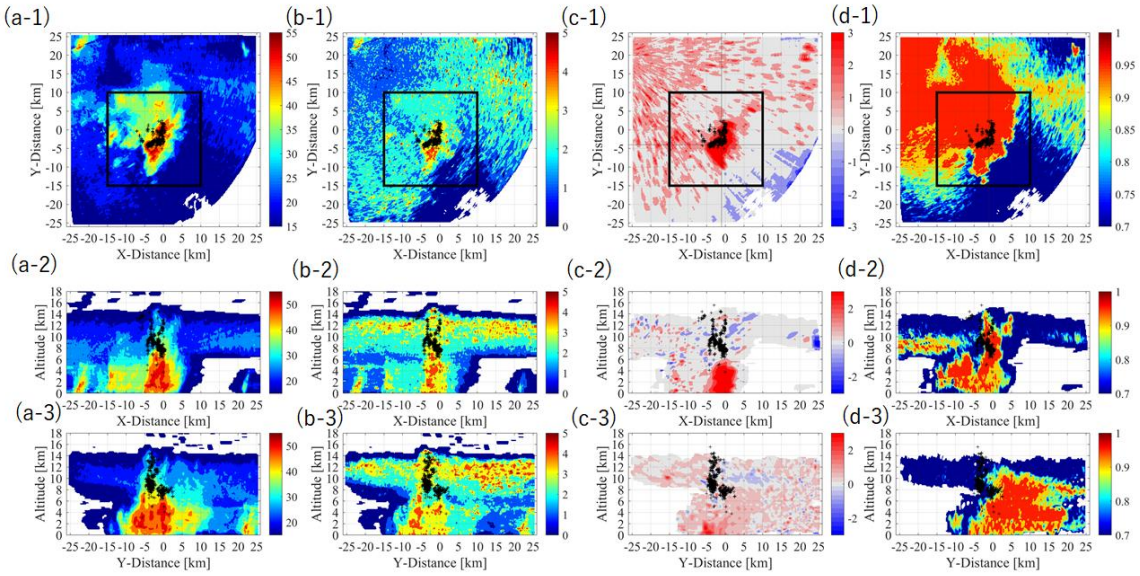


Figure 1. MPPAWR and Lightning observations at 17:07:23 JST, Aug 13, 2020. **(a)** Z_h, **(b)** Z_{dr}, **(c)** K_{dp}, and **(d)** ρ_{hv}. Index 1 denotes horizontal column maximums; 2 and 3 denote vertical distributions (South and North). Vertical plots are orthogonal maximum projections for (a, b) and cross-sections along the dotted lines for (c, d). Black dots: 30-s integrated lightning sources.

References

[1] H. Kikuchi, et. al. (2020), Initial observations for Precipitation Cores with X-band Dual Polarized Phased Array Weather Radar, *IEEE Transactions on Geoscience and Remote Sensing*, 58, 5, 3657-3666.

Technology for Avoiding Aircraft Lightning Strikes

Eiichi Yoshikawa[1,2], Shoichi Horishita[2], Yoshiro Hamada[2], and Tomoo Ushio[1]
[1]The University of Osaka, Osaka, Japan
[2]Japan Aerospace Exploration Agency, Mitaka, Japan
Corresponding author: yoshikawa@eei.eng.osaka-u.ac.jp

To reduce carbon emissions, the commercial aviation industry is introducing technologies such as high-efficiency engines and lightweight carbon fiber-reinforced polymer (CFRP) components. However, damage to some advanced aircraft components can require more costly and labor-intensive repairs than damage to conventional components, increasing the importance of preventing weather-related damage [1]. Aviation weather hazards include turbulence, wind shear, lightning, snow, icing, and fog [2]. This study focuses on identifying aircraft lightning risk areas to support strike avoidance and reduce operational disruptions.

Figure 1 presents two examples of aircraft lightning strikes. Commercial aircraft are designed and certified to withstand lightning strikes and maintain flight safety. Nevertheless, strikes require post-flight inspections and can disrupt subsequent operations. Minor damage may be addressed through temporary repairs, allowing an aircraft to return to service with some delay, whereas more severe damage can ground an aircraft for several days and lead to flight cancellations. Repairs to CFRP components can require more time and labor than repairs to conventional metallic components. Beyond repair costs, airlines face reduced aircraft availability and additional expenses associated with passenger disruption.



Figure 1: Photographs of an actual aircraft lightning strike, provided by Otowa Electric Co. Ltd.

As discussed by Rakov and Uman [3], most aircraft lightning strikes are triggered by the aircraft itself rather than resulting from interception of naturally occurring lightning. The outward branching of the lightning channels in Figure 1 is consistent with initiation from the aircraft. This distinction highlights the importance of identifying atmospheric conditions favorable for aircraft-triggered lightning. Although lightning detection is widely used to support avoidance decisions, it may not adequately identify areas where aircraft can trigger lightning.

Building on these findings, JAXA has developed technology to identify aircraft lightning risk areas by examining relationships between reported strikes and surrounding meteorological conditions. Strike locations and times were analyzed together with corresponding single-polarization weather radar and radiosonde observations. The analysis showed that many strikes occurred near regions with high vertically integrated reflectivity (VIR) and high reflectivity near the −10 °C level (MTR), as illustrated in Figure 2 [4] [5].

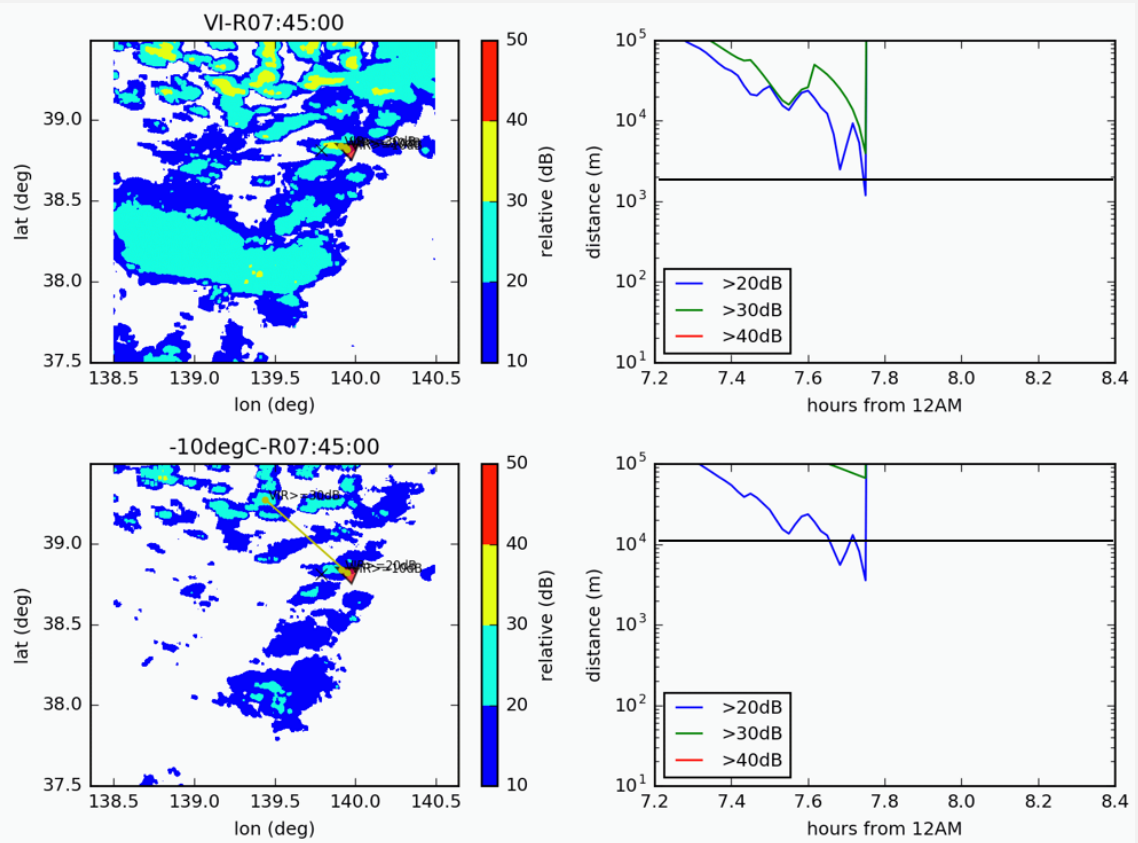


Figure 2: Relationship between a reported aircraft lightning strike and surrounding meteorological conditions. Left panels: horizontal distributions of VIR (top) and MTR (bottom). Right panels: time series of the distances from the aircraft to regions exceeding specified VIR (top) and MTR (bottom) thresholds.

Based on these relationships, we developed a heuristic classification algorithm that applies distance thresholds to regions where VIR and MTR exceed specified levels. Two sets of thresholds define high- and moderate-risk areas, shown in red and yellow, respectively, in Figure 3. In this example, the aircraft experienced a lightning strike within the high-risk area. More recently, we introduced a machine learning classifier that improved classification performance and enabled a wider range of input variables to be incorporated with relatively few tuning parameters [6]. This flexibility facilitates further improvement without requiring increasingly complex, manually defined threshold rules.

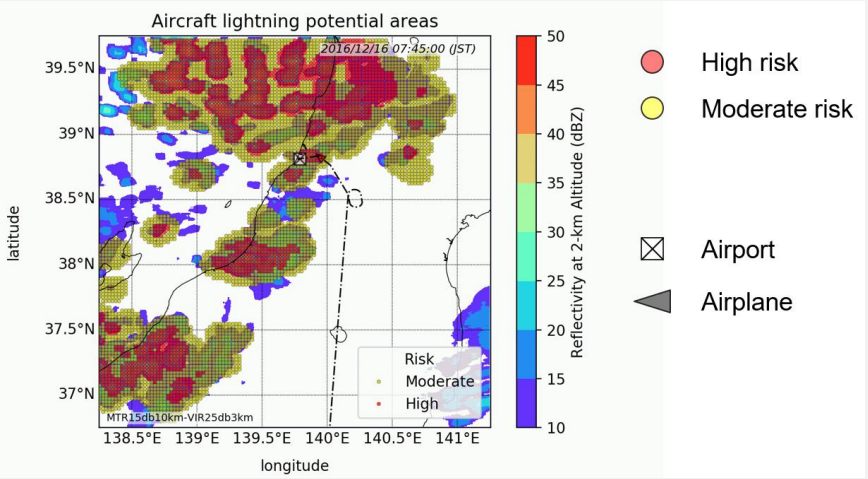


Figure 3: Demonstration of an output of the heuristic algorithm

Further improvements could be achieved by incorporating observations that provide additional information about the relevant atmospheric conditions. Phased array weather radars [7] [8] [9] are particularly promising because their rapid volumetric scanning can capture the evolution of three-dimensional storm structures. Advanced array signal processing methods [10] [11] [12] [13] [14] [15] [16] could further improve measurement accuracy. Doppler wind lidars offer complementary observations in precipitation-free air. Although conventional wind lidars have resolution limitations, emerging technologies [17] [18] [19] may help address these constraints. Combining radar and lidar observations could extend coverage across precipitating and nonprecipitating environments and support the identification and avoidance of lightning and other aviation weather hazards.

References

[1] International Civil Aviation Organization (ICAO), “ICAO Strategic Plan 2026–2050,” 2024.

[2] WEATHER-Eye Consortium, “WEATHER-Eye Vision, 3rd Edition,” 2019.

[3] V. A. Rakov and M. A. Uman, “LIGHTNING: Physics and Effects,” Cambridge University Press, 2003.

[4] Yoshikawa, E., and T. Ushio, 2019: Tactical Decision-Making Support Information for Aircraft Lightning Avoidance: Feasibility Study in Area of Winter Lightning. Bull. Amer. Meteor. Soc., 100, 1443–1452.

[5] E. Yoshikawa, S. Horishita, T. Ushio, “Aircraft Lightning Potential Area Detection Enhanced by Echo Top Height and its Evaluation with Winter Lightning Cases,” Journal of Atmospheric Electricity, vol 39, no 2, 70–78, 2021.

[6] E. Yoshikawa, S. Horishita, Y. Hamada, T. Ushio, and V. Chandrasekar, “ON THE FEASIBILITY OF MACHINE LEARNING-BASED DETECTION,” 35th Congress of the International Council of the Aeronautical Sciences, Sydney, Australia, 2026.

[7] F. Mizutani et al., "Fast-Scanning Phased-Array Weather Radar With Angular Imaging Technique," in IEEE Transactions on Geoscience and Remote Sensing, vol. 56, no. 5, pp. 2664-2673, May 2018.

[8] T. Ushio et al., "Recent Progress on the Phased Array Weather Radar at X Band," 2022 IEEE Radar Conference (RadarConf22), New York City, NY, USA, 2022, pp. 1-4.

[9] E. Yoshikawa, T. Ushio and H. Kikuchi, "Application of Comb Beam Transmission to C-band Phased Array Weather Radar," 2022 IEEE Radar Conference (RadarConf22), New York City, NY, USA, 2022, pp. 1-5.

[10] E. Yoshikawa, T. Ushio and H. Kikuchi, "A Study of Comb Beam Transmission on Phased Array Weather Radars," in IEEE Transactions on Geoscience and Remote Sensing, vol. 59, no. 8, pp. 6346-6356, Aug. 2021.

[11] E. Yoshikawa et al., "MMSE Beam Forming on Fast-Scanning Phased Array Weather Radar," in IEEE Transactions on Geoscience and Remote Sensing, vol. 51, no. 5, pp. 3077-3088, May 2013.

[12] E. Yoshikawa, V. Chandrasekar, K. Nishimura, D. Kitahara, Y. Wada and T. Ushio, "Angular Profile Estimation on Phased Array Weather Radar by Maximizing Marginal Likelihood," 2025 IEEE International Radar Conference (RADAR), Atlanta, GA, USA, 2025, pp. 1-6.

[13] E. Yoshikawa, V. Chandrasekar, D. Kitahara, K. Nishimura, Y. Wada and T. Ushio, "Comparison of Re-Iterative Adaptive Beamformers for Phased Array Radars," 2025 22nd European Radar Conference (EuRAD), Utrecht, Netherlands, 2025, pp. 39-42.

[14] Y. Wada et al., "Mitigation of Ground-Clutter Effects by Digital Beamforming With Precomputed Weighting Matrix for Phased Array Weather Radar," in IEEE Transactions on Geoscience and Remote Sensing, vol. 62, pp. 1-14, 2024.

[15] D. Kitahara, H. Kuroda, A. Hirabayashi, E. Yoshikawa, H. Kikuchi and T. Ushio, "Nonlinear Beamforming Based on Group-Sparsities of Periodograms for Phased Array Weather Radar," in IEEE Transactions on Geoscience and Remote Sensing, vol. 60, pp. 1-19, 2022

[16] H. Kikuchi, E. Yoshikawa, T. Ushio and Y. Hobara, "Adaptive Beamforming Using Steering Vector Correction for Phased-Array Weather Radar," in IEEE Journal of Selected Topics in Applied Earth Observations and Remote Sensing, vol. 14, pp. 8419-8426, 2021.

[17] Eiichi Yoshikawa and Tomoo Ushio, "Wind ranging and velocimetry with low peak power and long-duration modulated laser," Opt. Express 25, 8845-8859 (2017)

[18] Eiichi Yoshikawa, Hiroshi Yamasuge, Makoto Aoki, Hironori Iwai, Takayuki Nakano, Hiroshi Oikawa, Tomoo Ushio, Shoken Ishii, and V. Chandrasekar, "Coherent Doppler LIDAR with long-duration frequency-modulated pulses for wind sensing," Opt. Express 31, 42730-42743 (2023)

[19] E. Yoshikawa, V. Chandrasekar, M. Aoki, H. Iwai, T. Ushio and S. Ishii, "Coherent Doppler Lidar (CDL) for Measuring Wind with Transmission of Frequency-Modulated Pulse or Continuous Wave," IGARSS 2024 - 2024 IEEE International Geoscience and Remote Sensing Symposium, Athens, Greece, 2024, pp. 6242-6245.

Design and Field Verification of a Needle-Tip Electric Field Meter

Kazuki Oobayashi[1], Shunichi Yanagawa[1], and Koichiro Michimoto[2]
[1]SHODEN CORPORATION, Chiba, Japan
[2]Hayakawa Institute of Seismo Electromagnetics, Co., Ltd., Tokyo, Japan
Corresponding author: oobayashika@sdn.co.jp

1. Introduction

In recent years, lightning-related accidents involving people have occurred at schools and other locations. The Japan Meteorological Agency (JMA) provides information such as the Lightning Nowcast and LIDEN (Lightning Detection Network), but because this information is derived from data generated by actual lightning strikes, it is difficult to use for advance countermeasures. In addition, although the LIDEN data distributed by the JMA make it possible to identify the location of a lightning strike, the positional accuracy is not disclosed, and because the information only becomes available after a lightning strike has occurred, it also presents challenges for advance countermeasures.

As a method for detecting the approach of a thundercloud in advance, some studies have examined the use of electrostatic field observations to assess thundercloud approach. [1] However, when observations are made using a field mill (hereafter, EFM), installing units at many locations is difficult because of the cost and the equipment involved.

In wide-area observation, measurement locations can be divided into primary (important) sites and auxiliary (supplementary) sites. Primary sites require high-precision measurement, whereas auxiliary sites are considered acceptable if the sensor simply responds once the electrostatic field exceeds a certain level.

We therefore investigated the construction of a system, suitable for wide-area observation, based on the long-established needle-tip corona current measurement technique.

In this paper, the sensor fabricated using the needle-tip corona current measurement technique is referred to as the needle-tip electric field meter.

For verification, the needle-tip electric field meter was installed at a site where a rotating-vane field mill was already in operation, and field verification was performed.

2. System Configuration

• Needle-Tip Electric Field Meter

As noted above, the EFM offers high precision but is expensive, and because it has rotating parts requiring maintenance, it is cost-prohibitive to install at many locations. In contrast, with the needle-tip corona current measurement technique [2], [3], the sensor element is simply a needle-shaped piece of metal, so the structure is simple and inexpensive. However, it should be noted that, because no output is produced until corona discharge begins, the precision is inferior to that of a rotating-vane field mill.

Because using an expensive metal such as platinum for the needle tip is not practical, a waterproof connector for the power supply and ground line is provided on the lower part of the enclosure. Data are transmitted to a cloud server via Wi-Fi at fixed intervals.

A system overview diagram is shown in Fig. 2.1. A commercially available probe needle, shown in Fig. 2.2(a), is used for the needle tip. Because the signal attenuates if the distance between the probe needle and the circuit board is increased, the needle tip and the circuit board are housed together in the same enclosure, as shown in Fig. 2.2(b), so as to keep them as close together as possible. The corona current flowing through the needle is converted into a voltage via a resistor, the output voltage is adjusted by an amplifier, and the signal is measured by a microcontroller. The sampling

frequency for data acquisition is 1 kHz, and the data transmission interval to the cloud server is 1 minute. The data transmitted to the server consist of the maximum and minimum voltage values recorded during the preceding 1-minute interval, together with the latitude, longitude, and transmission time.

The dashboard screen available on the cloud server is shown in Fig. 2.3. The device connects to the Internet via a dial-up router. An API (Application Programming Interface) is used to send and receive data with the cloud server. The recorded electric field data are automatically plotted as graphs, and, based on the transmitted latitude and longitude, the surrounding LIDEN data are also collected and mapped.

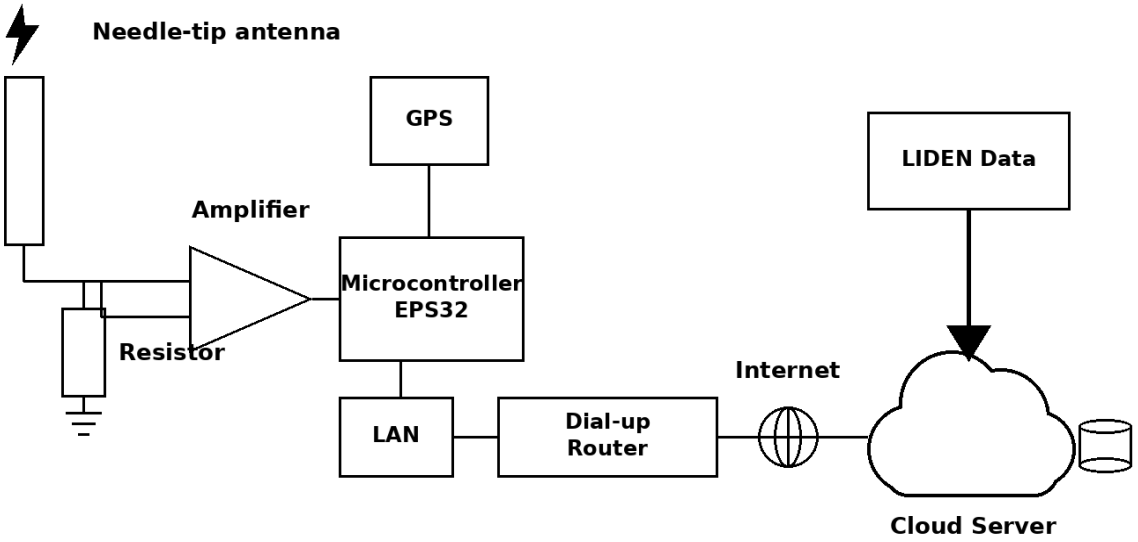
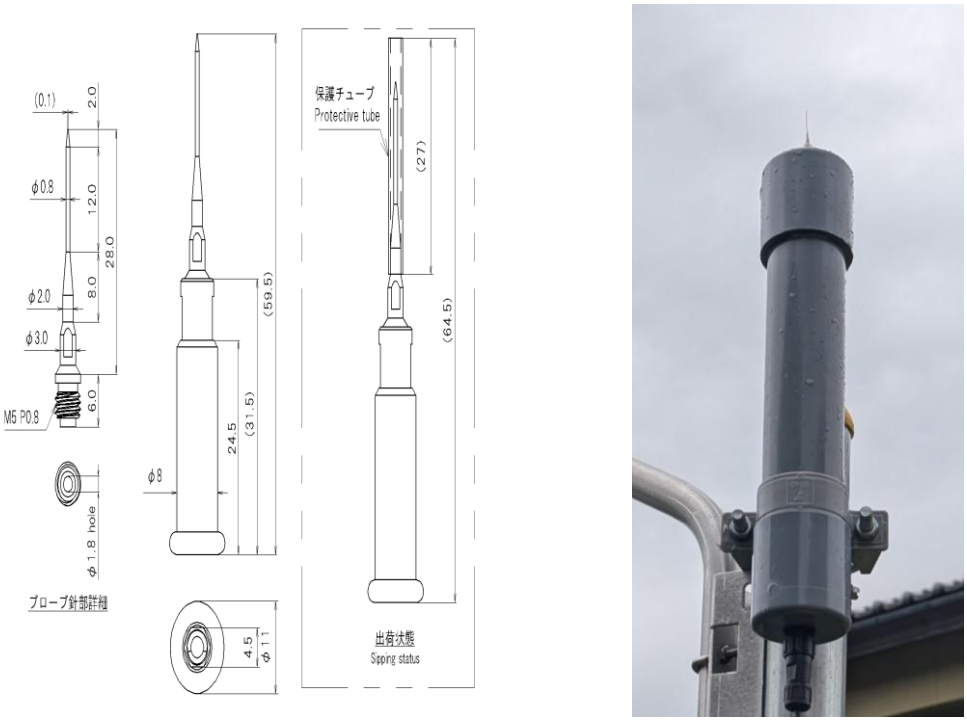


Fig. 2.1. System overview diagram.



(a) Needle tip (b) External appearance

Fig. 2.2. Structure of the needle-tip electric field meter.

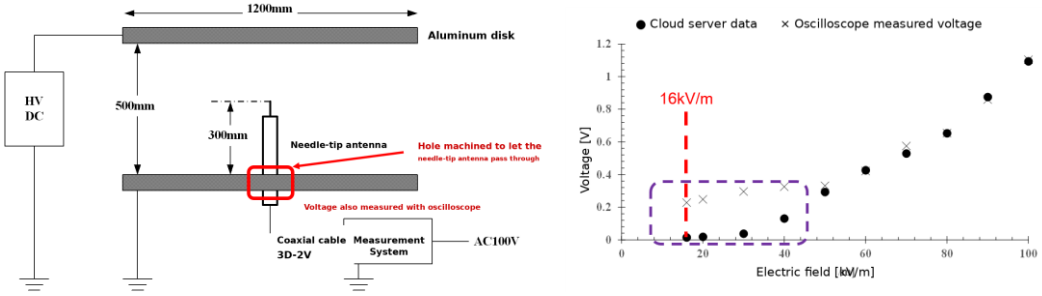


Fig. 2.3. Data monitoring screen.

3. Laboratory Verification [5]

The test setup is shown in Fig. 3.1(a). Two circular aluminum plates, each 1200 mm in diameter, were arranged in parallel, with a spacing of 500 mm between them. A 100-mm-diameter hole was provided at the center of the bottom plate so that the sensor could be passed through it. The test was conducted with the sensor protruding approximately 300 mm above the bottom plate.

The test results are shown in Fig. 3.1(b). The difference between the data sent to the cloud server and the results measured with an oscilloscope is attributed to the sampling period of the device. In this test setup, it was confirmed that the needle-tip electric field meter responds at approximately 16 kV/m. Because the mounting height in an actual field installation is expected to be 1.5 m or more, the device is expected to respond at a somewhat lower electrostatic field value under field conditions.



(a) Test setup (b) Test results

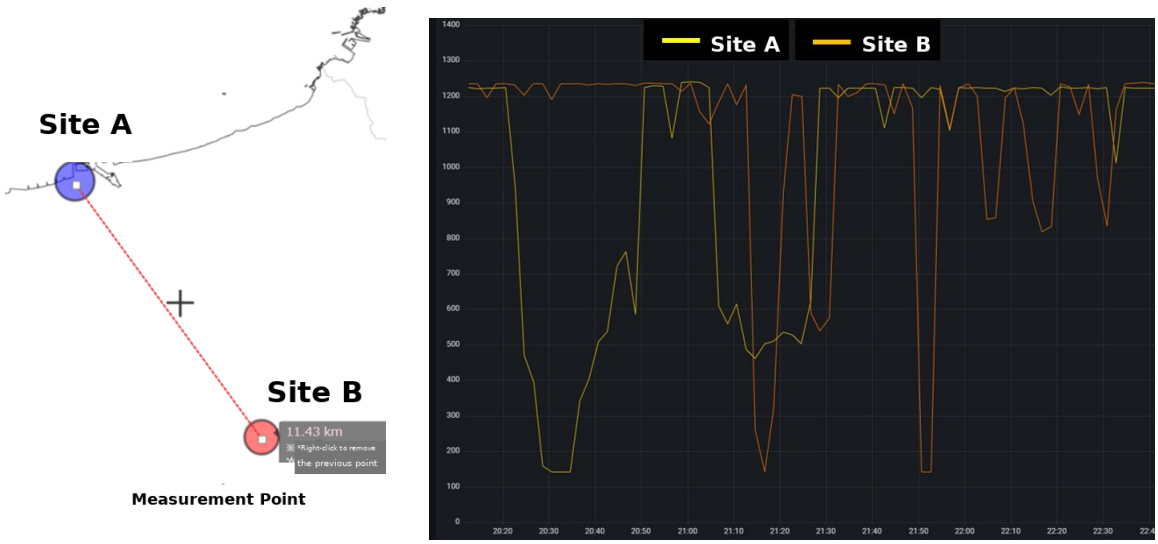
Fig. 3.1. Test setup and results.

4. Field Verification

This section reports the results of verification conducted in an actual field environment. Although the exact location cannot be disclosed, the observation site is located in the eastern part of Tottori Prefecture. A map of the observation site is shown in Fig. 4.1(a).

The needle-tip electric field meters were installed at different heights, but the height was not calibrated for the data reported here. Site A is installed at the height of the second floor of a building, and Site B is installed at the height of the fourth floor of a building. The straight-line distance between Sites A and B is approximately 11 km.

The observation results for a representative day are shown in Fig. 4.1(b). A negative-polarity amplitude was first observed by the needle-tip electric field meter at Site A, followed approximately 30 minutes later by a similar negative-polarity amplitude at Site B.



(a) Map (b) Measured data

Fig. 4.1. Observation data.

5. Countermeasures

When the electrostatic field changes greatly because of the approach of a thundercloud, the change can be confirmed even visually; however, when the electrostatic field is low, it is difficult to distinguish the signal from noise. As a countermeasure, we are therefore investigating an approach based on integrating the waveform.

Because noise produces only transient peaks, it can be removed by integration. In contrast, small changes in the electric field produce continuous peaks, so integrating the waveform allows the signal to be represented as a stable value.

6. Conclusion

This paper has reported on the design of the needle-tip electric field meter and the results of its field testing. Because units incorporating the countermeasure described above are scheduled to be deployed to the field sequentially, we expect them to be effective for data collection during the winter season.

References

[1] K. Oobayashi et al., “Observation of Electric Field around Wind Power Generation Facilities,” IEEJ Technical Meeting Record, FTE-16-011, HV-16-051 (2016).

[2] K. Nakamura et al., “Development of a Lightning Warning Device Using Needle-Tip Corona Current,” IEEJ Transactions on Power and Energy (Trans. IEE Japan, Vol. B), pp. 93–100 (1981).

[3] S. Higashiyama et al., “Characteristics of Needle-Tip Corona Current under Thunderclouds and Detection of Thundercloud Approach,” IEEJ Transactions on Fundamentals and Materials (Trans. IEE Japan, Vol. A), pp. 411–418 (1979).

[4] Sato Parts Co., Ltd., TJ-100-KT, https://www.satoparts.co.jp/products/search/T_TJ/TJ-100-KT

[5] K. Oobayashi et al., “Development of an Electrostatic Field Measurement Device and Network System Using the Needle-Tip Corona Current Measurement Technique,” presented at the National Conference of the Japan Society for Electrical Installation Engineering.

Real-Time 3D Imaging of Lightning Discharges and Charge Distributions in Thunderclouds for Early Warning of Lightning Strikes

M. Akita[1], T. Inaba[1,2], T. Morimoto[3], Y. Takayanagi[3], Z. Kawasaki[4], M. R. Ahmad[5], Zafri Baharuddin[6]
1. The University of Electro-Communications (UEC), Japan, 2. Inaba Radar Technology Laboratory, Japan
3. Kindai University, Japan, 4. Osaka University, Japan, 5. Universiti Teknikal Malaysia Melaka (UTeM), Malaysia
6. Universiti Tenaga Nasional (UNITEN), Malaysia
Corresponding author: aki ta.manabu@uec.ac.jp

1. Introduction

Lightning activity is closely related to the electrical charge structure inside thunderclouds, which plays an important role in the initiation and propagation of lightning discharges [1]. In particular, intracloud (IC) discharges often occur before cloud-to-ground (CG) lightning. Therefore, monitoring the temporal evolution of charge distributions inside thunderclouds is important not only for understanding lightning development but also for providing fundamental information for future lightning forecasting and early-warning applications [2]. We have developed a VHF broadband digital interferometer (VHF DITF) that images lightning discharge channels by locating VHF radiation sources with high temporal resolution. For scientific investigations of lightning physics, the system is operated in a continuous-recording mode, which allows lightning processes accompanied by VHF radiation to be observed in detail. To improve these observations, we have also developed an advanced direction-finding method capable of resolving multiple radiation sources occurring within the same analysis interval [3]. This improvement enables weak positive breakdowns to be detected even when they are masked by much stronger negative breakdowns, providing more detailed information on bidirectional leader development. These detailed continuous-recording observations have also provided scientific knowledge that can be utilized for real-time monitoring. In particular, positive leaders generally produce weak VHF radiation, whereas recoil leaders produce stronger VHF radiation and propagate backward along previously developed positive-leader channels. Thus, recoil leaders can provide information on the locations of positive-leader channels and the associated negative-charge regions [2]. For real-time monitoring, however, continuous recording is not suitable because of the large amount of waveform data and computational load. We therefore employ a triggered-recording mode, which substantially reduces the amount of data to be processed but generally fails to detect weak positive-leader radiation. By incorporating the scientific knowledge obtained from continuous-recording observations, the missing positive-leader information can be inferred from recoil-leader observations. The three-dimensional (3D) locations of neutralized charge are reconstructed from multi-site VHF observations, while the amount of neutralized charge is estimated by combining the reconstructed lightning channels with ground-based electric-field-change measurements [4]. This approach makes real-time 3D imaging of thundercloud charge distributions possible using triggered VHF observations [2]. Thus, the present development follows a stepwise approach: **continuous recording → improved scientific observation → scientific knowledge → triggered recording → real-time charge imaging**. In this study, we present this framework and demonstrate its application to real-time monitoring of the temporal evolution of thundercloud charge distributions. This study is conducted as part of the SATREPS project “Real-Time Lightning 3D Imaging and Forecasting Project for Sustainable and Reliable Supply of Energy and Storm Disaster Early Warning,” supported by JST and JICA.

2. Methods

2.1 Real-Time 3D Charge Imaging System

VHF DITF estimates the azimuth and elevation of VHF radiation sources associated with lightning discharges. Direction finding is performed independently at each observation site, and the results from two or more sites are combined to reconstruct 3D lightning channels. Figure 1 shows the overall processing flow of the proposed system. Each site performs two-dimensional (2D) direction finding and transfers the processed results to a central data server. At the server, 3D reconstruction, automatic charge-polarity identification, and neutralized-charge estimation are performed. Ground-based electric-field-change measurements are also used to estimate the amount of neutralized charge.

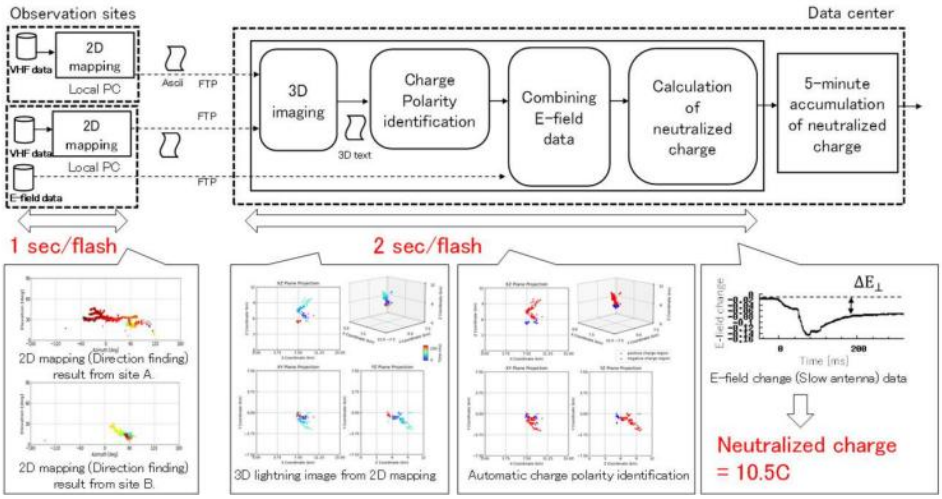


Fig. 1. Processing flow for real-time 3D imaging of thundercloud charge distributions.

2.2 From Scientific Observation to Real-Time Monitoring

For scientific investigations of lightning physics, the VHF DITF is operated in continuous-recording mode. This mode enables detailed observation of negative leaders, positive leaders, and recoil leaders, but requires relatively large computational resources and is therefore not suitable for real-time operation. To improve these scientific observations, we introduced a multi-source direction-finding method based on maximum-likelihood estimation. This method enables weak positive-breakdown radiation to be separated from stronger negative-breakdown radiation occurring simultaneously. Such observations provide more complete information on bidirectional leader development and the relationship between positive leaders and subsequent recoil leaders. For real-time monitoring, the system is operated in triggered-recording mode, which substantially reduces the amount of waveform data and processing load. However, weak VHF radiation from positive leaders is generally not detected in this mode. The characteristics of the two recording modes are summarized in Table 1. Continuous-recording observations show that recoil leaders propagate backward along previously developed positive-leader channels and produce relatively strong VHF radiation. Therefore, recoil leaders can be detected in triggered recordings and used to infer the locations of the preceding positive-leader channels. Fig. 2 illustrates how recoil leaders are used as substitutes for positive leaders to estimate negative-charge regions. In the proposed

Table 1 Continuous- and Triggered-recording modes of VHF DITF

	Continuous Mode	Triggered Mode
Negative leader	○	○
Positive leader	○	×
Recoil leader	○	○
Main purpose	Scientific observation	Real-time monitoring



Fig. 2. Estimation of negative-charge regions using recoil leaders as proxies for positive leaders.

method, recoil-leader information is used to identify negative-charge regions that cannot be directly obtained from positive-leader radiation in triggered mode.

2.3 Estimation of Thundercloud Charge Distribution

The reconstructed 3D lightning channels provide the spatial locations of charge neutralization. Negative-leader sources are associated with positive-charge regions, whereas recoil-leader information is used to identify negative-charge regions. The total neutralized charge for each flash is estimated by combining these 3D source locations with the corresponding electric-field change measured on the ground [4]. By accumulating the estimated neutralized charge from successive lightning discharges, a 3D charge distribution inside the thundercloud is obtained. Repeating this procedure sequentially enables real-time monitoring of the temporal evolution of the thundercloud charge structure.

3. Results

3.1 Real-Time Estimation of Neutralized Charge for Individual Flashes

Fig. 3 shows two examples of individual lightning flashes processed by the proposed real-time system. For each flash, 3D lightning channels were reconstructed from the 2D direction-finding results

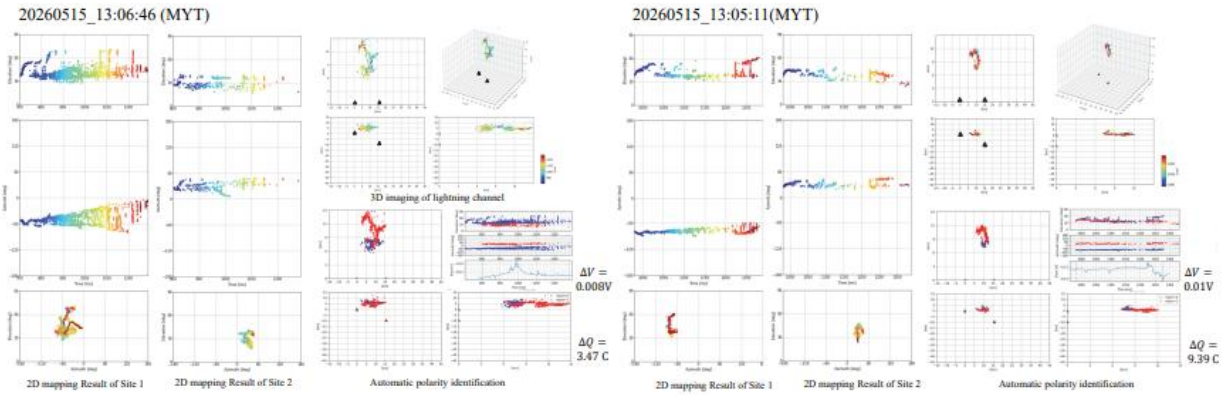


Fig. 3. Examples of real-time estimation results. Two examples of individual IC lightning flashes, showing reconstructed 3D lightning channels, automatic polarity identification, and the estimated neutralized charge for each flash.

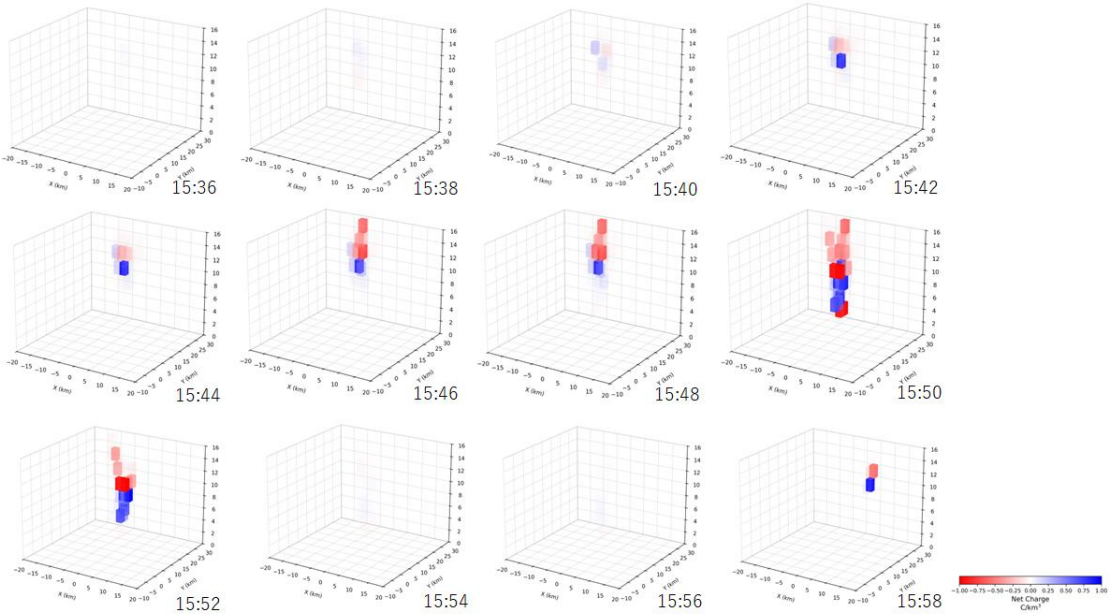


Fig. 4. Charge distribution accumulated over 10 minutes from individual flashes, showing good agreement with the growth process of the thundercloud charge structure on 2026/05/15 in Malaysia.

obtained at multiple VHF observation sites, and the charge polarity was identified automatically by using the relationship between negative leaders and recoil leaders. The neutralized charge was then estimated by combining the reconstructed 3D channel with the corresponding electric-field change measured on the ground. The results demonstrate that the proposed method can estimate the neutralized charge of individual IC discharges in real time. In both examples, the system successfully identified the discharge structure and provided physically reasonable values of neutralized charge. These results indicate that the proposed framework is capable of converting real-time radio observations into quantitative information on lightning charge transfer.

3.2 Temporal Evolution of Thundercloud Charge Structure

Fig. 4 shows the accumulated charge distribution obtained by integrating the charge estimated for individual flashes over a 10-minute interval. The accumulated distributions clearly show the temporal development of a vertically separated thundercloud charge structure. These results demonstrate that the proposed method is useful not only for analyzing individual flashes but also for monitoring the evolution of thundercloud electrical structures in real time. Because the distributions are derived from IC discharges, which often precede CG lightning, they may provide important information for future lightning forecasting and lightning-strike warning.

4. Conclusion

We developed a real-time framework for 3D imaging of thundercloud charge distributions using VHF broadband interferometry and ground-based electric-field measurements. Detailed continuous-recording observations were first used to improve the scientific understanding of lightning discharge processes, including weak positive breakdowns and recoil leaders. The resulting knowledge was then incorporated into the triggered-recording mode, enabling real-time charge-polarity identification and neutralized-charge estimation despite the difficulty of directly detecting positive leaders. The proposed system successfully estimated neutralized charge for individual IC discharges and reproduced the temporal development of thundercloud charge structures by accumulating the estimated charge. These results demonstrate the feasibility of transferring knowledge obtained from detailed scientific observations to real-time thundercloud monitoring. Such information can provide a useful basis for future lightning forecasting and lightning-strike warning.

Acknowledgements

This study was supported by the Science and Technology Research Partnership for Sustainable Development (SATREPS), a collaborative program between the Japan Science and Technology Agency (JST) and the Japan International Cooperation Agency (JICA).

References

[1] M. Akita, S. Yoshida, Y. Nakamura, T. Morimoto, T. Ushio, Z. Kawasaki, and D. Wang, “Effects of charge distribution in thunderstorms on lightning propagation paths in Darwin, Australia,” Journal of the Atmospheric Sciences, vol. 68, no. 4, pp. 719–726, 2011.

[2] M. Akita, T. Inaba, T. Morimoto, Y. Takayanagi, Z. Kawasaki, M. R. Ahmad, and F. H. B. Nordin, “Real-time 3D imaging of charge distributions in thunderclouds along the Malacca Strait based on VHF broadband interferometry,” XVIII International Conference on Atmospheric Electricity (ICAE 2026), Barcelona, Spain, 2026.

[3] M. Akita, T. Inaba, T. Morimoto, Y. Takayanagi, Z. Kawasaki, M. R. Ahmad, and F. H. Nordin, “Imaging of positive part of bi-directional leader of lightning discharge based on VHF broadband interferometer,” Proc. URSI Asia-Pacific Radio Science Conference (AP-RASC 2025), Sydney, Australia, Aug. 17–22, 2025.

[4] M. Akita, Z. Kawasaki, S. Yoshida, T. Morimoto, and T. Ushio, “Estimation for charge distributions related with individual lightning discharges using VHF broadband digital interferometer,” Journal of Atmospheric Electricity, vol. 32, no. 2, pp. 55–63, 2012.

Challenges and Application of the X-Band Phased-Array Weather Radar

Tomoo Ushio and Eiichi Yoshikawa
The University of Osaka, Japan
Corresponding author: ushio@eei.eng.osaka-u.ac.jp

1. Introduction

In recent years, weather-related disasters have occurred frequently in Japan and worldwide, highlighting the need for rapid and detailed observations of hazardous convective storms. Weather radar, a remote-sensing technology that uses electromagnetic waves, is one of the most effective tools for observing the atmospheric phenomena associated with these disasters. Most operational weather radars use parabolic antennas to form narrow pencil beams. They mechanically rotate in azimuth while sequentially changing the elevation angle. Although such systems provide reliable observations, a near-surface scan typically takes approximately 1–5 min, and a full volumetric scan may require 5–10 min or longer, depending on the scan strategy. In contrast, cumulonimbus clouds that produce localized heavy rainfall can develop substantially within about 10 min, while tornado-producing circulations can evolve and move on timescales of only a few minutes. Consequently, conventional mechanical scanning may not fully resolve the life cycle of rapidly evolving convective phenomena. Phased-array technology addresses this limitation by enabling rapid electronic scanning in elevation.

Unlike conventional weather radars that use parabolic antennas to form pencil beams, phased-array radars employ array antennas composed of multiple transmit and receive elements. Their system characteristics differ in several respects, including the use of a broad fan beam for transmission and digitally formed narrow beams for reception. These characteristics enable rapid volumetric observations but also introduce specific technical challenges. This paper discusses the principal advantages and limitations of X-band phased-array weather radar.

2. Phased Array Weather Radar

Toshiba Corporation, the National Institute of Information and Communications Technology (NICT), and Osaka University developed an X-band phased-array Doppler weather radar capable of observing detailed three-dimensional precipitation structures in approximately 10–30 s by combining electronic scanning in elevation with mechanical scanning in azimuth [1], [2]. Figure 1 shows the phased-array weather radar installed at the Suita Campus of The University of Osaka. The hexagonal antenna contains 128 vertically arranged antenna elements. A broad fan beam is transmitted in elevation, and the backscattered signals are received by the full array. Digital beamforming then forms multiple narrow receive beams with an angular spacing of approximately 1°, thereby resolving the elevation dimension. Mechanical rotation in azimuth completes the rapid three-dimensional scan.



Fig. 1. Phased-array weather radar at the Suita Campus of The University of Osaka.

The first single-polarization system was installed on the roof of the Department of Electrical Engineering building at Osaka University's Suita Campus in May 2012. A dual-polarization multiparameter phased-array weather radar was subsequently installed in the Tokyo metropolitan area in December 2017 and was operated during the Tokyo 2020 Olympic and Paralympic Games. The single-polarization radar at Osaka University was replaced by a dual-polarization system in December 2022. Figure 2 presents observations of linearly organized convective storms on July 13, 2013, and August 17, 2022. In both cases, dense sampling at approximately 100 elevation angles captures the three-dimensional storm structure at high spatial and temporal resolution. Because full-volume observations can be obtained every 30–60 s, the formation and descent of precipitation cores can be monitored in detail. Such observations can support more accurate short-term precipitation forecasting and data assimilation [3], [4], representing a major advantage of phased-array weather radar.

The observational accuracy of the dual-polarization system was evaluated against an X-band dual-polarization radar equipped with a parabolic antenna [5]. At low elevation angles and for observations separated by no more than 15 s, the two systems showed correlations of 0.77–0.99 for radar reflectivity factor, differential reflectivity (ZDR), specific differential phase (KDP), and Doppler velocity. These results indicate broadly comparable performance under the conditions examined. However, the level of agreement depends on the parameter, elevation angle, temporal separation, calibration, and quality-control procedure; therefore, the results should not be interpreted as demonstrating universally identical accuracy for all observing conditions.

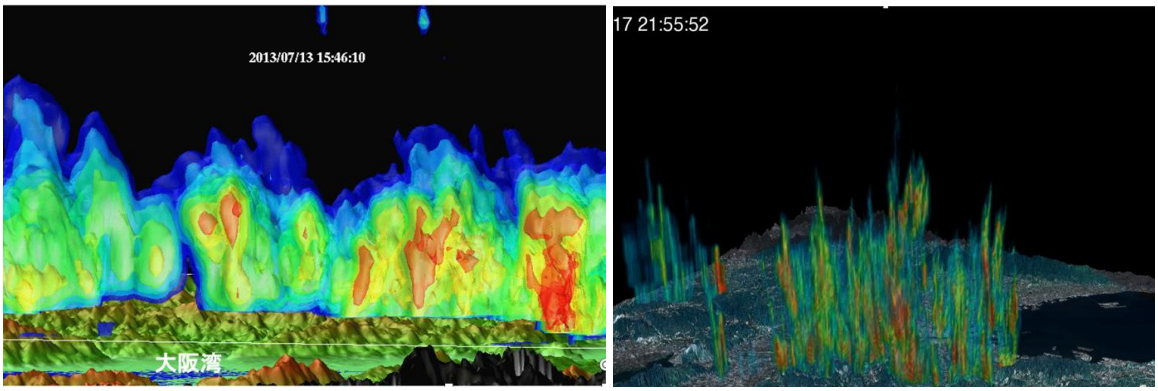


Fig. 2. Examples of convective storm systems observed by the phased-array weather radar at The University of Osaka on July 13, 2013 (upper), and August 17, 2022 (lower).

A technical limitation of phased-array weather radars using digital beamforming is contamination through relatively high sidelobes associated with fan-beam transmission. Figure 3 [6] shows the received-power distribution for a receive beam steered to an elevation angle of 5°. Central Osaka lies approximately 10 km south of the radar and contains many tall buildings. At a range of 10 km, the center of a 5° receive beam is approximately 0.87 km above the radar level, well above most buildings. Nevertheless, echoes from ground targets enter through sidelobes and can obscure precipitation echoes. The circular discontinuity near the radar indicates the transition between short- and long-pulse observations used with pulse compression; it reflects a difference in sensitivity rather than a processing error. The upper panel of Figure 4 shows a range–height cross section in which ground-clutter contamination extends to apparent elevation angles above 10°. The lower panel shows the corresponding result after adaptive digital beamforming based on the minimum mean-square-error (MMSE) criterion is applied to place an antenna-pattern null toward the ground-clutter direction [6]. The method substantially suppresses the clutter contribution, allowing the precipitation echo to be more clearly recovered.

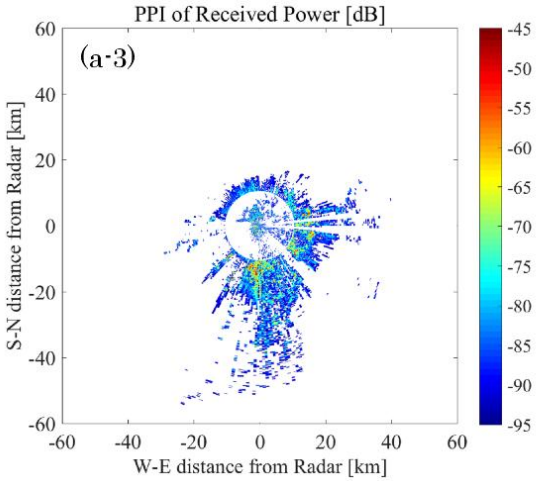


Fig. 3. Example of the horizontal distribution of received power for a beam steered to an elevation angle of 5° [6].

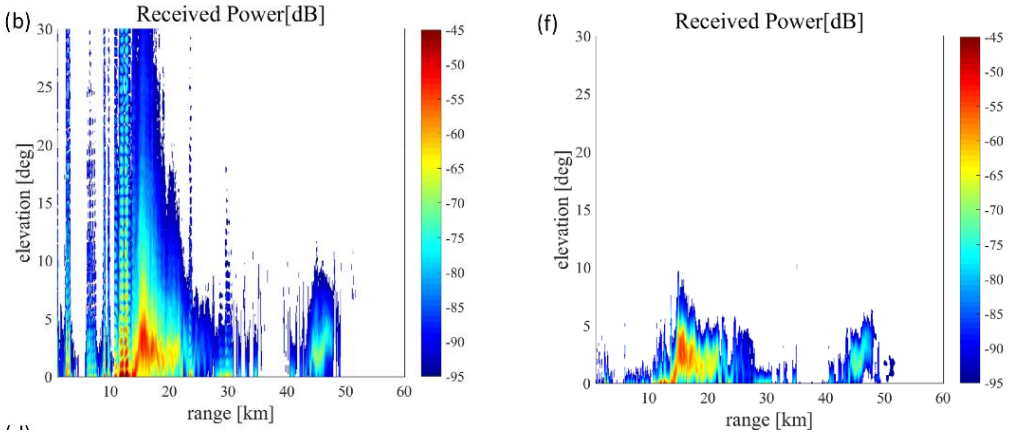


Fig. 4. Range–height cross sections of received power under rainy conditions. The upper panel was obtained using conventional Fourier beamforming, whereas the lower panel was obtained using MMSE adaptive beamforming [6].

3. Summary

The rapid, high-density volumetric observations provided by phased-array weather radar offer substantial advantages for monitoring rapidly evolving convective storms and for short-term precipitation prediction. Available intercomparison results indicate that, under the evaluated conditions, dual-polarization phased-array measurements can achieve accuracy broadly comparable to that of an X-band radar with a parabolic antenna. A key limitation is ground-clutter contamination caused by relatively high sidelobes associated with broad fan-beam transmission. Adaptive digital beamforming based on the MMSE criterion can substantially mitigate this contamination. Continued evaluation across a wider range of precipitation regimes, elevation angles, and clutter environments is required to quantify performance and operational robustness.

References

[1] E. Yoshikawa, T. Ushio, Z.-I. Kawasaki, S. Yoshida, T. Morimoto, F. Mizutani, and M. Wada, "MMSE beam forming on fast-scanning phased array weather radar," IEEE Trans. Geosci. Remote Sens., vol. 51, no. 5, pp. 3077–3088, 2013.

[2] F. Mizutani, T. Ushio, E. Yoshikawa, S. Shimamura, H. Kikuchi, M. Wada, S. Satoh, and T. Iguchi, "Fast-scanning phased array weather radar with angular imaging technique," IEEE Trans. Geosci. Remote Sens., vol. 56, no. 5, pp. 2664–2673, 2018, doi: 10.1109/TGRS.2017.2780847.

[3] P. Baron, K. Kawashima, D. Kim, H. Hanado, S. Kawamura, T. Maesaka, K. Nakagawa, S. Satoh, and T. Ushio, "Nowcasting multiparameter phased-array weather radar echoes of localized heavy precipitation using a 3D recurrent neural network trained with an adversarial technique," J. Atmos. Oceanic Technol., vol. 40, no. 7, pp. 803–821, 2023.

[4] T. Miyoshi, M. Kunii, J. Ruiz, G. Lien, S. Satoh, T. Ushio, K. Bessho, H. Seko, H. Tomita, and Y. Ishikawa, "Big data assimilation revolutionizing severe weather prediction," Bull. Amer. Meteor. Soc., vol. 97, no. 8, pp. 1347–1354, 2016, doi: 10.1175/BAMS-D-15-00144.1.

[5] K. Asai, H. Kikuchi, T. Ushio, and Y. Hobara, "Validation of X-band multiparameter phased-array weather radar by comparing data from Doppler weather radar with a parabolic dish antenna," J. Atmos. Oceanic Technol., vol. 38, no. 9, pp. 1561–1570, 2021, doi: 10.1175/JTECH-D-20-0213.1.

[6] H. Kikuchi, E. Yoshikawa, T. Ushio, F. Mizutani, and M. Wada, "Application of adaptive digital beamforming to Osaka University phased array weather radar," IEEE Trans. Geosci. Remote Sens., vol. 55, no. 7, pp. 3875–3884, 2017, doi: 10.1109/TGRS.2017.2682886.

Radio Observations of the Strongest Lightning Discharges in Winter Thunderstorms

Ting Wu[1], and Daohong Wang[1]
[1]Department of Electrical, Electronic and Computer Engineering, Gifu University, Gifu, Japan
Corresponding author: wu.ting.x4@f.gifu-u.ac.jp

1. Introduction

Winter thunderstorms in the Hokuriku region of Japan are well known for producing extremely powerful positive cloud-to-ground (CG) flashes, which have been linked to transient luminous events such as sprites and elves [1]. Strong negative CG flashes in winter, by contrast, have remained a puzzle: a handful of earlier studies reported strange, strong low-frequency (LF) pulses of negative discharges, but their origin was variously attributed to upward lightning from transmission lines [2] or to energetic in-cloud pulses (EIPs) [3], never to ordinary return strokes. In this paper, we will review our related studies in the past few years and will show that (1) the strongest negative discharges in winter are return strokes with anomalous waveforms, which we call Energetic Compact Strokes (ECSs); (2) ECSs are the dominant source of downward terrestrial gamma-ray flashes (TGFs) in winter; (3) ECSs have a distinct seasonal and spatial climatology; and (4) the strongest positive return strokes, despite having even larger peak currents, retain normal waveforms and a different physical origin. Together, these results provide a complete picture of the most extreme lightning discharges in winter thunderstorms based on radio observations.

2. Observation and Data

All lightning data are observed by the Fast Antenna Lightning Mapping Array (FALMA), an LF (500 Hz–500 kHz) lightning observation network in the Hokuriku region providing 2-D lightning locations and peak-current estimates [4]. Downward TGFs were identified using three independently operated gamma-ray detector systems operated by three different groups [5], with sub-microsecond

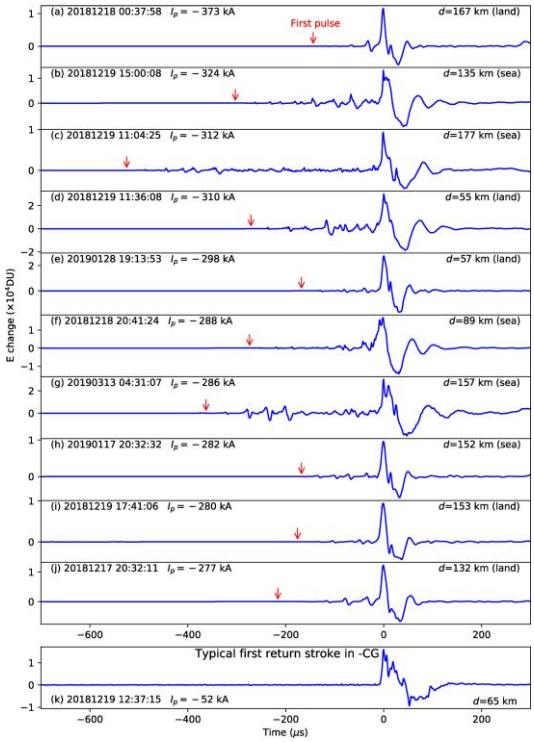


Figure 1. (a–j) E-change waveforms of the 10 strongest ECSs. The red arrow indicates the first identified pulse before each ECS. (k) Typical waveform of the first return stroke in a negative cloud-to-ground flash. Adapted from [6].

timing accuracy. Superbolt records from the World Wide Lightning Location Network (WWLLN) were also used to compare with FALMA waveforms.

3. Energetic Compact Strokes: The Strongest Negative Return Strokes

Using data recorded by FALMA from December 2018 to March 2019 in Hokuriku region, we analyzed negative discharges with peak currents larger than 150 kA. We found that almost all these strong discharges produce E-change waveforms fundamentally different from ordinary first return strokes. Waveforms of the strongest 10 events are shown in Figures 1a~1j, along with the waveform of a typical negative first return stroke in Figure 1k [6]. Compared with normal negative first strokes, these events have the following special characteristics:

(1) A preceding leader with total duration typically shorter than 500-700 μs, with no clear division into two distinct stages of preliminary breakdown and stepped leader;

(2) Leader pulses that are unusually large and readily visible, rather than the barely detectable stepped-leader pulses of ordinary flashes;

(3) A largely symmetric, bipolar return-stroke pulse with comparable rise and fall times and no fine structure on the falling edge;

(4) A frequent small secondary pulse superimposed on the negative half-cycle of the main pulse.

Because their waveforms differ so strongly from regular return strokes, these strokes cannot be easily identified as CG strokes. As a result, their existence had been unknown for many years.

We have shown several pieces of evidence that these strong discharges are negative return strokes [6]. Particularly, a −335 kA stroke was recorded simultaneously by FALMA and LAPOS, a high-speed optical system. The optical observation of this stroke showed a downward negative leader descending with a speed of 4-5×10^6 m/s, immediately followed by an upward-propagating return-stroke wave with a speed of 1.5×10^8 m/s, a typical return-stroke speed. The speed of the downward leader is an order of magnitude faster than ordinary stepped leaders but is typical for downward leaders in ECSs.

Because these discharges combine extreme intensity with an extremely short preceding leader, we named them Energetic Compact Strokes (ECSs).

4. ECSs as the Major Source of Downward TGFs

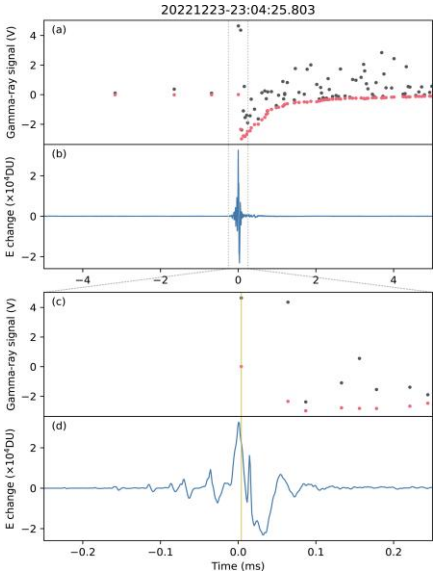


Figure 2. Gamma-ray signals associated with an ECS. (a) and (c) Gamma-ray signals. (b) and (d) FALMA waveforms of the ECS. Time zero corresponds to the peak of the ECS pulse. The yellow line indicates the onset of the TGF. Adapted from [5].

Coordinated observations between FALMA and the three independent gamma-ray detector networks show that ECSs occurring within roughly 4 km of a detector are essentially always coincident with a downward TGF, whose onset consistently falls between the main return-stroke peak and the secondary pulse. One example is shown in Figure 2 [5]. During five winter seasons, 12 of 19 downward TGFs (63%) observed by the three TGF detectors were associated with ECSs; a subsequent observing period (Nov. 2023~Jan. 2025) confirmed this with 9 of 15 (60%) TGFs linked to ECSs. Percentages varied by detector site (80% and 88% for two gamma-ray-triggered systems, but only 17% for a VHF-triggered system located near a tower), suggesting the true fraction of downward TGFs associated with ECSs nationwide may be even higher than 60~63%. These results establish ECSs as the major source of downward TGFs winter thunderstorms in Japan and show that a purely radio-based ECS detection can serve as an effective TGF proxy.

5. Climatology of ECSs in Japan

To characterize when and where ECSs occur, a three-year FALMA survey (Nov. 2021–Oct. 2024) within a 500-km radius in Japan identified 2567 ECSs. Their occurrence is overwhelmingly concentrated in winter, peaking in November and December, with essentially none in June to September despite these months having the highest overall flash rates in Japan. Spatially, ECSs cluster along the west coast of Japan as shown in Figure 3, and preferentially occur over moderate elevations of a few hundred meters. A smaller population of ECSs occurs in May and June, almost exclusively on the top of high mountains (~2000 m), likely because short cloud-to-ground distances can be achieved on the high mountain tops.

ECSs also tend to be temporally isolated: the median time separation to the nearest other lightning discharge (within 20 km) is ~4 minutes for ECSs versus ~1.5 minutes for ordinary negative strokes, and no ECS at all occurred within the 77 highest-flash-rate spatiotemporal grid cells examined (a cumulative 38.5 hours of intense storm activity), indicating that ECSs cannot be easily produced in thunderstorms with frequent lightning activities.

Finally, comparison with WWLLN shows that 9 of 10 superbolts observed near Japan are negative CG strokes whose FALMA waveforms satisfy all ECS criteria, suggesting that a substantial fraction

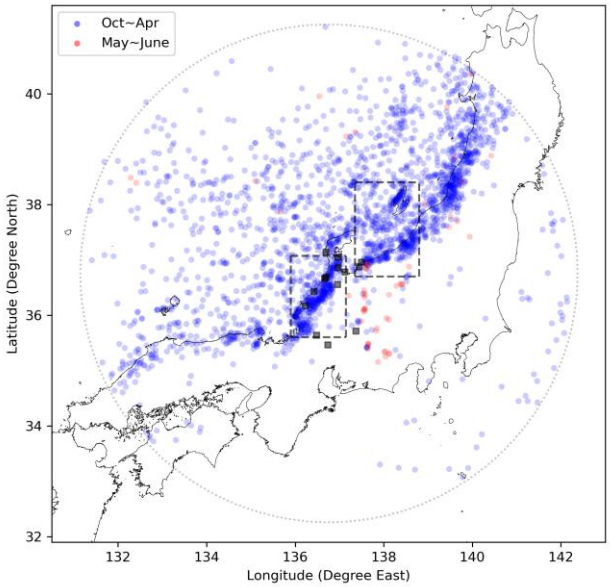


Figure 3. Locations of ECSs in an area with a radius of 500 km. Blue dots represent ECSs in winter seasons (October~April), and red ones in May and June. Black squares represent observation sites of FALMA.

of WWLLN superbolts worldwide may in fact be ECSs. The so-called mountain-top energetic pulses (MEPs) [7] observed in high mountains in the western United States may also be ECSs.

6. The Strongest Positive Return Strokes

Different from ECSs, an analysis of about 690 first positive return strokes (peak currents 5-476 kA, mean 82 kA, median 63 kA) shows that even the strongest positive strokes produce conventional return stroke waveforms. Interestingly, peak currents of positive return strokes are positively correlated with rise time, fall time, pulse width, and half-peak width, with the strongest correlation for rise time. [8]

The defining feature of the strongest positive strokes is the short time difference between flash initiation and return stroke. The strongest strokes almost always occurred within 10 ms of flash initiation. We also observed a positive CG case with a peak current of 160 kA, in which the first return stroke occurred only 1.28 ms after the flash initiation, which is the shortest interval ever reported for a positive CG flash. Mapping of discharge sources before and after the ten strongest events indicates an initiating downward positive leader propagating at speeds on the order of 10^6 m/s, comparable to the downward leaders in ECSs. We speculate that strong positive strokes require a large, low-altitude positive charge region generating a strong downward electric field.

7. Discussion

Both extreme polarities of winter lightning point to the same underlying requirement: a strong, horizontally extensive charge layer situated close to the ground, which is more common in winter thunderstorms in the Hokuriku region. However, the two polarities produce very different waveforms. ECSs produce abnormal return stroke waveforms that can be easily misclassified. On the other hand, very strong positive strokes retain normal radio signatures. This asymmetry has practical consequences: nationwide lightning location systems such as JLDN and NLDN can reliably classify even the strongest positive strokes, but may still misclassify or miss ECSs.

The demonstration that ECSs are the major source of downward TGFs is particularly significant. Because ECSs can be identified from simple LF observations, existing LF lightning networks can be used to remotely monitor a large fraction of downward TGF activity without dedicated gamma-ray instrumentation. The tendency of ECSs to cluster in specific coastal, moderate-elevation "hotspots" further implies that some regions and their residents may experience significant doses of gamma radiation over the years, and it is necessary to carry out a thorough evaluation of radiation doses from downward TGFs in winter thunderstorms.

References

[1] T. Suzuki, M. Hayakawa, Y. Matsudo, and K. Michimoto, "How do winter thundercloud systems generate sprite-inducing lightning in the Hokuriku area of Japan?" Geophysical Research Letters, vol. 33, no. 10, 2006.

[2] M. Ishii and M. Saito, "Lightning electric field characteristics associated with transmission-line faults in winter," IEEE Transactions on Electromagnetic Compatibility, vol. 51, no. 3, pp. 459–465, 2009.

[3] F. Lyu, S. A. Cummer, and L. McTague, "Insights into high peak current in-cloud lightning events during thunderstorms," Geophysical Research Letters, vol. 42, no. 16, pp. 6836–6843, 2015.

[4] T. Wu, D. Wang, and N. Takagi, "Lightning mapping with an array of fast antennas," Geophysical Research Letters, vol. 45, no. 8, pp. 3698–3705, 2018.

[5] T. Wu, D. M. Smith, Y. Wada, K. Nakazawa, M. Oguchi, M. Kamogawa, et al., "Energetic compact strokes as the major source of downward terrestrial gamma-ray flashes in winter thunderstorms," Geophysical Research Letters, vol. 52, no. 6, p. e2024GL113194, 2025.

[6] T. Wu, D. Wang, H. Huang, and N. Takagi, "The strongest negative lightning strokes in winter thunderstorms in Japan," Geophysical Research Letters, vol. 48, no. 21, p. e2021GL095525, 2021.

[7] F. Lyu, S. A. Cummer, P. R. Krehbiel, W. Rison, E. C. Bruning, and S. A. Rutledge, "A distinct class of high peak-current lightning pulses over mountainous terrain in thunderstorms," Geophysical Research Letters, vol. 48, no. 14, p. e2021GL094153, 2021.

[8] T. Wu, D. Wang, and N. Takagi, "On the intensity of first return strokes in positive cloud-to-ground lightning in winter," Journal of Geophysical Research: Atmospheres, vol. 127, p. e2022JD037282, 2022.

Equivalent Source Strengths of Earthquake-Associated ULF Magnetic Anomalies from Three-Dimensional Simulations

Yoshiaki Ando[1]
[1]Department of Computer and Network Engineering, Graduate School of Informatics and Engineering, The University of Electro-Communications, Chofu, Tokyo, Japan
Corresponding author: y-ando@uec.ac.jp

We estimate the relative strengths of source currents required to reproduce reported ultra-low-frequency (ULF) electromagnetic anomalies associated with 13 earthquakes using three-dimensional electromagnetic field simulations. The simulations account for the event-specific source and observation station locations and the three-dimensional conductivity structure of the ground and seawater. For each event, we adopt the Loma Prieta reference spectral shape corresponding to its classification as preseismic or imminent-seismic and estimate its overall amplitude. For the 12 preseismic cases, the estimated source strengths show a weak positive correlation with moment magnitude, although the correlation is not statistically significant.

1. Introduction

Over the past several decades, many studies have reported ultra-low-frequency (ULF) electromagnetic anomalies possibly associated with earthquakes(EQs)[1-11]. These signals are commonly referred to as EQ-associated ULF emissions. Their possible association with EQs has generally been evaluated from their spatial locality, such as detection at a station near the epicenter but not at remote reference stations, and from their temporal proximity to the corresponding mainshock[1-3]. When anomalous signals were not readily apparent in the observed magnetic field time series, signal processing techniques, including polarization[3,4], fractal[4], and principal component analyses[11], were used to identify candidate anomalous changes.

Although these techniques have revealed potentially relevant signatures, each method has been applied to only a limited number of EQ events. Moreover, the quantities obtained using different techniques are not necessarily comparable, and no common analysis method has been applied consistently to a sufficiently large set of events. Consequently, systematic event-to-event comparisons remain difficult, and the physical characteristics and generation mechanisms of EQ-associated ULF emissions remain poorly understood.

In this study, we analyze 13 EQs using a unified procedure to estimate the relative source current strength required to reproduce each reported ULF signal. The estimates are obtained using three-dimensional simulations based on the weighted Laguerre polynomial finite-difference time-domain (WLP-FDTD) method[12], accounting for source-observer geometry, ground-conductivity structure, observation frequency band, and electromagnetic field component[13]. The dataset includes reported candidate ULF anomalies associated with EQs in California, Armenia, Guam, Indonesia, Japan, Italy, India, Peru, and Slovenia[1-10]. According to the original reports, eleven events are classified as preseismic, with ULF signals observed more than 24 hours before the mainshock, whereas Spitak is classified as imminent-seismic, with the signal observed during the 24 hours preceding the mainshock. We examine whether the estimated relative source current strengths exhibit a systematic dependence on moment magnitude Mw.

2. Source Current Estimation

We estimate the source current strengths for each event from the reported anomalous magnetic field amplitudes. The simulations account for the event-specific geometry including the hypocenter and observation station locations, and for the three-dimensional electrical conductivity distribution of the ground and seawater. Each source is modeled as a horizontal current dipole with a length of 1 km, located at the hypocenter, and oriented parallel to the nearby active fault. We assume that each event shares the Loma Prieta current spectral shape corresponding to its temporal class and differs

from the reference only in overall amplitude. For each event, a three-dimensional WLP-FDTD simulation [14,15] yields the magnetic transfer function $\hat{B}_k(f)$, defined as the component k at the observation site produced by a unit current moment. Detailed discretization parameters are omitted here because the present study focuses on comparing the inferred source strengths among events.

We first estimate the source current spectra for the Loma Prieta event[1] and use them as the reference spectra $I_{LP}(f)$. This event is selected because both preseismic and imminent-seismic ULF signals were reported over a broad frequency range. The magnetic field amplitudes were extracted from Fig. 2 of Ref. [1] and converted into source current spectra using the simulated transfer functions. The resulting spectra are shown in Fig. 1. Power-law fits yield $I_{LP}^{\mathrm{pre}}(f) \propto f^{-1.190}$ for the preseismic case and $I_{LP}^{\mathrm{im}}(f) \propto f^{-1.898}$ for the imminent-seismic case.

For a magnetic field amplitude reported at a single frequency f_s, the relative equivalent source strength α is determined from

$$B_{obs,k} = \left|\hat{B}_k(f_s)\right| \alpha I_{LP}(f_s) \Delta l$$

When an anomalous field amplitude is reported over a finite frequency band $f_1 \le f \le f_2$, we treat it as the root mean square amplitude over that band, where $\Delta f = f_2 - f_1$, and determine α from

$$B_{obs,k} = \left[\frac{1}{\Delta f}\int_{f_1}^{f_2} \left|\hat{B}_k(f)\alpha I_{LP}(f)\Delta l\right|^2 df\right]^{\frac{1}{2}}$$

Here, $B_{obs,k}$ denotes the reported anomalous magnetic field amplitude and $\Delta l = 1$ km is the prescribed dipole length. Because the inversion constrains the source current moment $I\Delta l$, α represents a relative source strength. Under the adopted Loma Prieta reference spectrum, differences in α quantify the event-to-event amplitude scaling required to reproduce the reported magnetic field amplitudes after accounting for the event-specific geometry.

3. Results and Discussion

Table 1 summarizes the EQ parameters and observation conditions used in this study, together with the estimated α. The EQ parameters were obtained from the International Seismological Centre (ISC) catalogue[16], whereas the station locations, observation frequency ranges, and anomalous magnetic field amplitudes were taken from the original reports[1-10]. The station distances were calculated from the corresponding event and station locations. The Loma Prieta preseismic spectrum was used as the reference for the 12 preseismic cases, while the imminent-seismic spectrum was used only for Spitak.

The estimated relative source current strengths are shown in Fig. 2. The Loma Prieta event is plotted as an open square because it defines the reference. The circles represent the other 11 preseismic cases, whereas the diamond represents the imminent-seismic Spitak case. Filled and open circles indicate broadband or multiband observations and narrowband or single-frequency observations, respectively. Vertical bars indicate ranges arising from reported amplitude bounds or differences among observed magnetic field components.

A least-squares fit to the logarithmic representative values gives

$$\log_{10}\alpha = 0.57\, M_w - 5.02$$

Although the correlation does not reach statistical significance for the present dataset (Pearson $r = 0.41, p = 0.19$), the positive slope is consistent with a physically plausible tendency for the relative source strength to increase with moment magnitude.

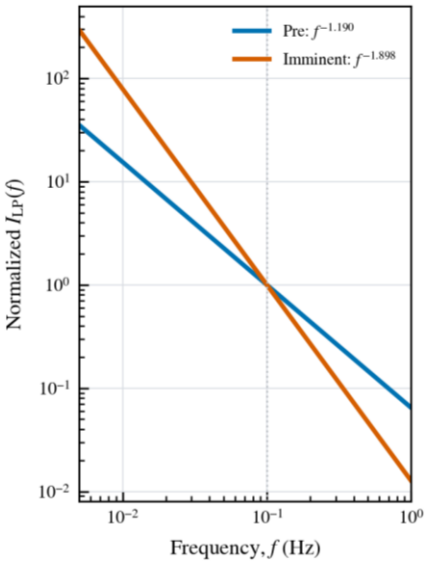


Figure 1. Loma Prieta reference spectral shapes normalized at 0.1 Hz.

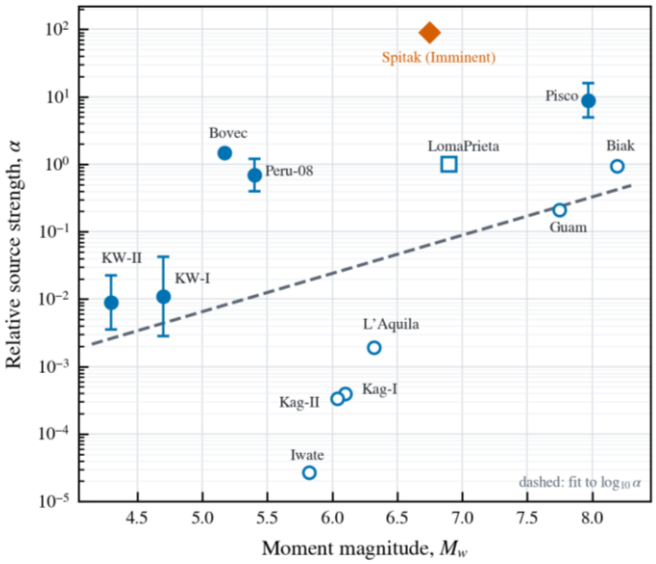


Figure 2. Relative equivalent source strength versus Mw. Vertical bars represent reported amplitude/component ranges; the dashed line is fitted to logarithmic midpoints of the 12 preseismic cases. Spitak is an imminent case and is not included in the fit. Filled circles represent broadband observations, while open circles represent narrowband or single frequency observations.

Table 1. Earthquake parameters, observation conditions, and estimated relative source strengths

Event	YYYYMMDD	Mw	Depth[km]	Distance[km]	Class	f [Hz]	α
Loma Prieta[1]	19891018	6.89	12	6.6	Pre/Im	0.01-1	1
Guam[3]	19930608	7.75	59	66	Pre	0.01	0.208
Biak[4]	19960217	8.19	20	100	Pre	0.01	0.937-0.941
Kagoshima 1[5]	19970326	6.10	25	62	Pre	0.01	3.99×10^{-4}
Kagoshima 2[5]	19970513	6.04	15	63	Pre	0.01	3.38×10^{-4}
Iwateken[6]	19980903	5.82	15	11	Pre	0.01	2.66×10^{-5}
L'Aquila[7]	20090406	6.32	10	20	Pre	0.010-0.015	0.00179-0.00205
Koyna-Warna 1[8]	20060417	4.70	17	28.0, 90.3	Pre	0.001-0.032	0.00285-0.0423
Koyna-Warna 2[8]	20060521	4.30	16.7	23.8, 94.8	Pre	0.001-0.032	0.00353-0.0226
Pisco[9]	20070815	7.97	38.7	188.2	Pre	0.022-0.1	4.96-15.8
Peru[9]	20080329	5.40	51.4	44.8	Pre	0.022-0.1	0.393-1.2
Bovec[10]	20040712	5.17	9.5	150.8	Pre	0.01-0.05	1.46
Spitak[2]	19881207	6.75	10	140	Im	0.1-1	89.5

For the two Koyna-Warna events, the anomalous component was not directly isolated in the magnetic field time series. The original report indicated that signals in the range of 1-80 pT could have been masked by stronger fields from other sources. The resulting amplitude bounds give $\alpha = 0.00285 - 0.0423$ and $0.00353 - 0.0226$ for Koyna-Warna I and II, respectively. For the Pisco and Peru events, three magnetic field components were available. Their component-wise estimates give $\alpha = 4.96 - 15.8$ for Pisco and $0.39 - 1.20$ for Peru. These intervals therefore represent different sources of uncertainty.

An apparent separation according to the reported observation bandwidth is also found in Fig. 2. The filled circle cases —Koyna-Warna, Bovec, Pisco, and Peru— were reported over frequency bands with fractional bandwidths of approximately 128-188%. In contrast, L'Aquila was analyzed over 0.010-0.015 Hz, corresponding to a fractional bandwidth of 40%, while Guam, Biak,

Kagoshima, and Iwate were observed at a single frequency of 0.01 Hz. At comparable magnitudes, the broadband estimates generally lie above the narrowband or single-frequency estimates.

The apparent separation may arise from the estimation of the reference current spectrum. The Loma Prieta reference spectrum was estimated by reading magnetic field amplitudes from a published figure. If the resulting spectral slope of -1.190 differs from the true slope, the estimated α becomes dependent on the observation frequency range. An overestimate of the spectral slope could therefore produce systematically smaller α values for the 0.01 Hz cases than for the broadband cases, as observed in Fig. 2. Alternatively, the source spectral shape may evolve with time during the preseismic stage. In this case, the magnetic field amplitudes should be extracted from event-specific time windows corresponding to comparable stages of the earthquake preparation process.

4. Conclusion

We estimated the relative source current strengths required to reproduce reported ULF magnetic anomalies for 13 earthquakes using the three-dimensional WLP-FDTD method. The strengths were normalized to the Loma Prieta reference spectra. For the 12 preseismic cases, the estimates showed a weak positive correlation with moment magnitude, although the correlation was not statistically significant. The estimates exhibited an apparent separation according to the reported observation bandwidth: the broadband cases had fractional bandwidths greater than 100%, while the other group comprised one narrowband case with a fractional bandwidth of 40% and several single-frequency cases. This apparent separation may reflect uncertainty in the source current spectral shape inferred from the Loma Prieta event, because an error in the reference spectral slope affects estimates. Temporal evolution in the source current spectral shape remains an alternative explanation.

Acknowledgments

The author thanks Ms. Shinno and Mr. Shimizu for their contributions to the numerical simulations and source strength estimation.

References

[1] A. C. Fraser-Smith et al., Geophys. Res. Lett., 17, 1465–1468, 1990.

[2] O. A. Molchanov et al., Geophys. Res. Lett., 19, 1495–1498, 1992.

[3] M. Hayakawa et al., Geophys. Res. Lett., 23, 241–244, 1996.

[4] M. Hayakawa et al., Geophys. Res. Lett., 27, 1531–1534, 2000.

[5] K. Hattori et al., In M. Hayakawa and O. A. Molchanov (Eds.), *Seismo Electromagnetics*, TERRAPUB, 19–28, 2002.

[6] K. Hattori et al., Phys. Chem. Earth, 29, 481–494, 2004.

[7] G. Prattes et al., Nat. Hazards Earth Syst. Sci., 11, 1959–1968, 2011.

[8] F. Dudkin et al., Nat. Hazards Earth Syst. Sci., 10, 1513–1522, 2010.

[9] E. M. Takla et al., Tectonophysics, 524–525, 29–36, 2012.

[10] G. Prattes et al., Nat. Hazards Earth Syst. Sci., 8, 501–507, 2008.

[11] K. Hattori et al., Phys. Chem. Earth, vol. 31, pp. 281–291, 2006.

[12] Y. S. Chung et al., IEEE Trans. Microw. Theory Tech., 51, 697–704, 2003.

[13] R. Kimura et al., Radio Science, vol. 59, doi:10.1029/2023RS007923, 2024.

[14] R. Shinno, Master's thesis, The University of Electro-Communications, 2024 (in Japanese).

[15] Y. Shimizu, Bachelor's thesis, The University of Electro-Communications, 2026 (in Japanese).

[16] The International Seismological Centre, ISC-GEM earthquake catalogue, https://www.isc.ac.uk/iscgem/

Spatiotemporal Distribution of Geomagnetic Discrepancies and Their Link to Major Earthquakes

Chieh-Hung Chen[1], and Xuemin Zhang[2]

[1] State Key Laboratory of Geohazard Prevention and Geoenvironment Protection (Chengdu University of Technology), Chengdu, China

[2]Institute of Earthquake Forecasting, China Earthquake Administration, Beijing, China

Corresponding author: nononochchen@gmail.com

Seismo-electromagnetic satellites represent a modern technology used to monitor seismo-ionospheric anomalies on a global scale. However, significant discrepancies in geomagnetic anomaly areas have been observed even from the same satellite magnetic data. Numerous scientists have reported that electromagnetic anomalies cover a wide area with a radius of thousands of kilometers associated with the preparation zone of major earthquakes. In contrast, the geomagnetic difference determined by two different magnetometers loaded on the satellites is mainly distributed across a limited half of the preparation zone. To investigate this discrepancy in the size of areas, we collected the spatiotemporal distribution of differences between the two magnetometers and further examined their relationship with major earthquakes ($M \geq 6.0$) that occurred during 2024–2025. These major earthquakes were classified into three groups based on their locations, and the differences were found to occur mainly on the land side rather than the ocean side. Based on the similar discrepancy observed in geomagnetic data retrieved on land as seismic waves propagated through, the discordance appears to be caused by ground vibrations that clearly affect the fluxgate-type magnetometers, which are highly sensitive to such vibrations. This suggests that seismo-ground-vibrations trigger acoustic waves and/or standing waves that propagate upward to the ionosphere, thereby triggering ionospheric perturbations before major earthquake occurrence. In contrast, ground vibrations before earthquakes are difficult to propagate through seawater and are therefore less likely to produce the observed magnetic difference on the ocean side of an earthquake. On the other hand, acoustic and/or standing waves can excite ionospheric currents, driving changes in the electrogeomagnetic field—which can explain why we often observe transient electromagnetic anomalies over a wide area. This also accounts for why traditional electromagnetic anomalies are mainly confined to the frequency range of 0.001–0.01 Hz. In short, ground vibrations before earthquakes that trigger acoustic waves and/or standing waves appear to be the causal mechanism driving pre-earthquake changes in the ionosphere. These vibrations can produce distinct measurement results from different magnetometers and affect the geomagnetic field, particularly in terms of the electromagnetic field as recorded by common magnetometers.

Statistical Relationship between Anomalous VHF Broadcast Wave propagation and Earthquake Occurrence

Kuniyuki Motojima[1]
[1]Gunma University
Corresponding author: motojima@gunma-u.ac.jp

Abstract: Short-term earthquake prediction is an important challenge for earthquake disaster mitigation. In this study, we statistically investigate the relationship between anomalous propagation of line-of-sight VHF broadcast waves and earthquakes with epicenters near the radio propagation paths. The results reveal a statistically significant relationship between anomalous VHF propagation and subsequent earthquake occurrence, suggesting that VHF propagation anomalies may be associated with processes occurring prior to earthquakes.

1. Introduction

Research on geophysical electromagnetic phenomena associated with seismic activity is important for developing effective earthquake hazard mitigation strategies[(1)-(3)]. The purpose of this research is to investigate the relationship between earthquake occurrences and anomalous line-of-sight propagation of VHF broadcast waves. We have been monitoring FM broadcast waves transmitted from broadcasting stations located within the line-of-sight region for several years. Our observations have revealed occasional anomalous propagation events that appear to be associated with earthquake occurrence[(4)].

In this report, we first introduce an monitoring system designed to continuously monitor VHF broadcast waves transmitted by FM broadcasting stations located within the line-of-sight region in the Kanto area of Japan. We then identify anomalous propagation events from broadcast-wave data collected over an extended period and statistically investigate their relationship with earthquakes that occurred near the radio propagation paths. Our analysis revealed a statistically significant relationship between anomalous propagation of line-of-sight VHF broadcast waves and subsequent earthquake occurrence.

2. Monitoring system

The purpose of this research is to investigate the relationship between anomalous line-of-sight propagation of VHF band radio waves and the occurrence of earthquakes near the propagation paths.

To investigate this relationship, we established a multidirectional VHF-band monitoring system. A unique feature of this monitoring system is its line-of-sight observation method, in which VHF radio waves transmitted from line-of-sight FM broadcasting stations in multiple directions are continuously monitored. The monitoring system is located in Kiryu, Japan, approximately 90 km north of Tokyo ($36°25'26''N, 139°20'58''E$). The locations of the Kiryu monitoring site and the FM radio broadcasting stations are shown in Fig. 1.

Kiryu is located near the outer limits of the line-of-sight ranges from the transmitting stations. Therefore, variations in the refractive index can directly affect the strength of the received waves. This indicates that the monitoring site in Kiryu is highly sensitive to anomalous propagation in the troposphere. For long-term observation, an automatic, around-the-clock monitoring system was developed. The system consists of multiple antennas, an automatic antenna selector, a spectrum analyzer used as a radio receiver, a PC for storing monitoring data, and a web server for publishing the data. The monitoring system uses four five-element Yagi antennas to receive signals from broadcasting stations in multiple directions. Each antenna is horizontally oriented toward one of four directions: north, south, east, and west. The antennas are installed on the roof of a five-story building. The spectrum analyzer serves as the receiver and provides the wide bandwidth and high sensitivity required for continuous monitoring. The data-storage PC records the received signal strength approximately every 40s. Each raw data set of the received broadcast waves is plotted and

uploaded to the web server at 30-minute intervals. The resulting plots can then be accessed online at any time. A schematic block diagram of the monitoring system is shown in Fig. 2.

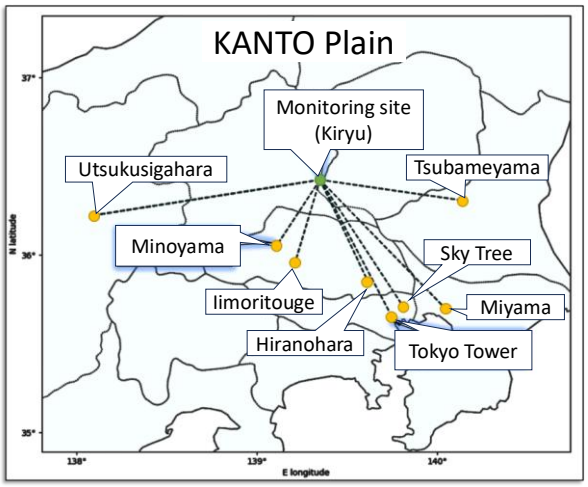


Figure 1. Monitoring site and FM stations

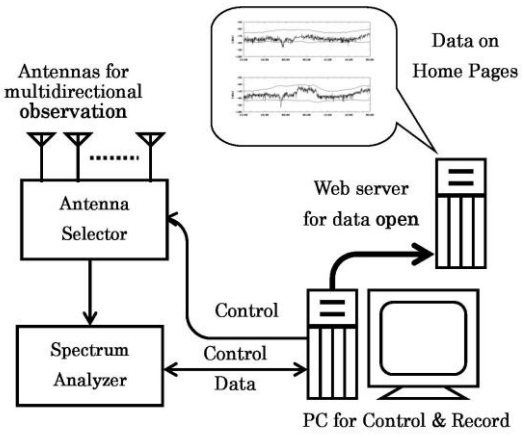


Figure 2. Monitoring system

3. Anomalous line-of-sight propagation in the VHF band

In previous studies, VHF radio waves from over-the-horizon broadcasting stations were monitored, and the mere reception of such signals was regarded as evidence of anomalous propagation[5],[6]. In contrast, our system monitors VHF radio waves under line-of-sight conditions. Since transmitted waves can normally reach the monitoring site within the line-of-sight range, a criterion is required to distinguish anomalous propagation from normal propagation. For this purpose, we adopted the following statistical procedure.

(a) Periods when the broadcast signal is off-air are excluded from the raw data.
(b) The data are subjected to STL decomposition (Seasonal-Trend decomposition using Loess), and the residual component is extracted. The mean (μ) and standard deviation (σ) of the residual component are then calculated.
(c) The thresholds for distinguishing anomalous variations from normal variations are defined as $\mu \pm N\sigma$, where N is a variable parameter, and the threshold level can be adjusted by varying N.
(d) An event is identified as an "anomalous propagation event" when the anomalous values detected using the criterion described in Step (c) occur at least twice within a five-minute period and this condition persists for at least one hour.

Using the above method to identify anomalous propagation, variations in line-of-sight VHF broadcast waves can be clearly identified while minimizing the effects of seasonal and daily variations.

As an example of anomalous propagation, the following figure shows the temporal variations in the received signal strengths of line-of-sight VHF broadcast waves arriving from multiple directions within the Kanto region. Fig. 3 shows the temporal evolution of the received signal strengths from 28 to 30 April 2012. The received signal strengths from Tokyo Tower and Miyama Station exhibited two distinct anomalies that occurred almost simultaneously: the first from 10:00 p.m. LT on 28 April to 11:00 a.m. LT on 29 April, and the second from 7:00 p.m. LT on 29 April to 6:00 a.m. LT on 30 April. Both anomalies lasted approximately half a day. The other two signals from Hiranohara and Tsubamesan Stations exhibited short-duration anomalies at around 11:30 p.m. LT on 28 April. During the second simultaneous anomaly, an earthquake occurred at 7:28 p.m. LT on 29 April 2012, with a magnitude of 5.8 and an epicenter at 35°42′ N, 140°36′ E in northeastern Chiba Prefecture. The anomalous propagation observed in these data may have been a precursor to the earthquake.

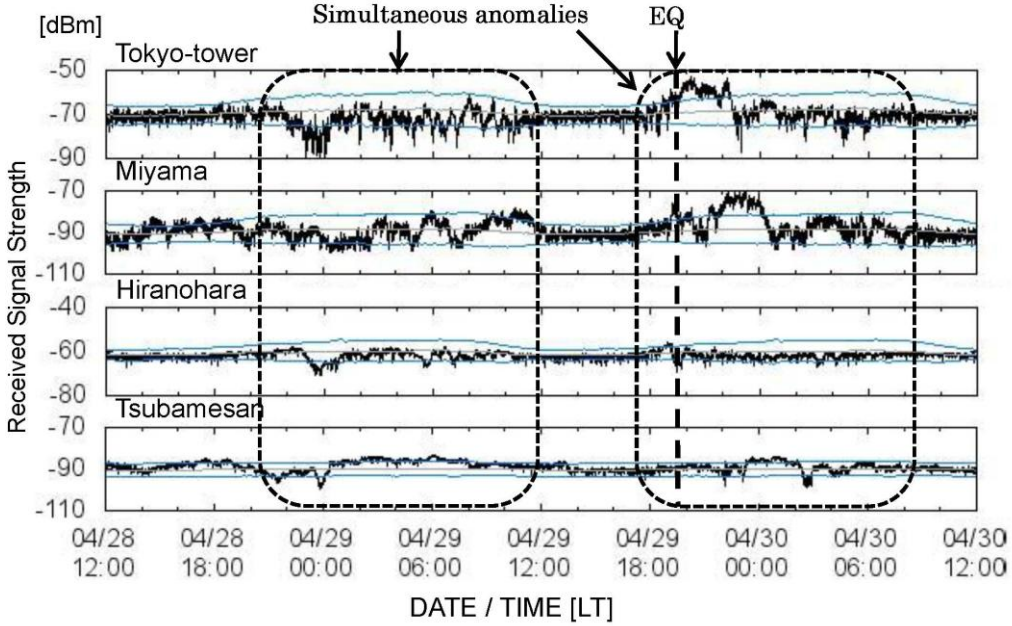
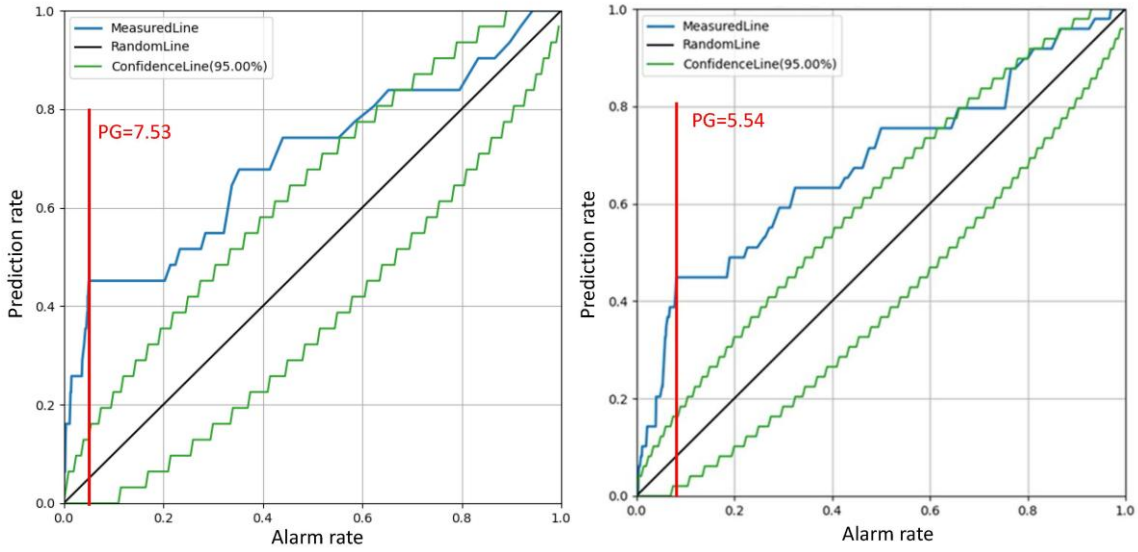


Figure 3. Temporal evolution from April 28 to 30, 2012. The dashed line indicates the earthquake associated with the anomaly.

4. Evaluation of the statistical relationship using Molchan's diagram



(a) NACK5 from Minoyama St., Saitama Pref. (b) Tokyo FM from Tokyo Tower St.

Figure 4. Results of Molchan's Diagrams

In this study, Molchan's diagram[7] is used to evaluate the relationship between anomalous propagation of line-of-sight VHF broadcast waves and earthquake occurrence. Molchan's diagram is a plot in which the alarm rate is shown on the horizontal axis and the prediction rate on the vertical axis. The alarm rate is defined as the ratio of the total duration of the warning periods, during which an earthquake is expected to occur following the detection of anomalous propagation, to the total observation period. Because the total duration of the warning periods varies depending on the degree of anomaly defined as anomalous propagation (i.e., the threshold used to identify anomalous propagation), the alarm rate ranges from 0 to 1. The prediction rate is defined as the ratio of the number of earthquakes that occurred during the warning periods to the total number of earthquakes that occurred during the target observation period.

The statistical analysis using the aforementioned Molchan's diagram revealed statistically significant relationships for most of the broadcast waves analyzed. The lead time between the appearance of anomalous propagation of line-of-sight VHF-band broadcast waves and subsequent earthquake occurrence was approximately 1–2 days for most of the broadcast waves. A statistically significant relationship between anomalous propagation and subsequent earthquake occurrence was observed when the alarm period was set to 2–6 days.

Fig. 4(a) shows the results of evaluating the relationship between anomalous propagation and earthquake occurrence for FM broadcast waves (NACK5, 77.5 MHz) transmitted from Mt. Minoyama, Saitama Prefecture, using Molchan's diagram. The results exceed the confidence line (p-value = 0.05) for most alarm rates, with a maximum probability gain of 7.53. Fig. 4(b) shows the results of a similar evaluation for FM broadcast waves (FM Tokyo, 80.0 MHz) transmitted from Tokyo Tower using Molchan's diagram. In this case, the results also exceed the confidence line (p-value = 0.05) for alarm rates of 0.6 or less, with a maximum probability gain of 5.54.

These results indicate that, following the appearance of anomalous propagation in line-of-sight VHF-band broadcast waves, the probability of an earthquake with a magnitude of 4.0 or greater occurring within 75 km of the radio propagation path increases several days later.

5. Conclusions

To contribute to earthquake disaster mitigation, we statistically investigated the potential use of anomalous propagation of line-of-sight VHF-band broadcast waves for short-term earthquake prediction. We analyzed the statistical relationship between anomalous propagation of line-of-sight VHF-band broadcast waves observed in the Kanto region and earthquakes with epicenters located near the radio propagation paths. The results suggest that anomalous propagation of VHF-band broadcast waves is more likely to occur several days before an earthquake.

An important subject for future research is to clarify the physical mechanisms responsible for the anomalous propagation observed in VHF-band broadcast waves. In addition, because meteorological phenomena can also affect VHF-band propagation, it is necessary to develop a method for determining whether an observed propagation anomaly is associated with an earthquake or caused by meteorological phenomena.

References

[1] Hayakawa, M., Kawate, R., Molchanov, O. A., and Yumoto, K., “Results of ultra-low-frequency magnetic field measurements during the Guam earthquake of 8 August 1993,” Geophys. Res. Lett., 23, 241–244, doi:10.1029/95GL02863, 1996.

[2] Molchanov, O. A. and Hayakawa, M., “Subionospheric VLF signal perturbations possibly related to earthquakes,” J. Geophys. Res., 103, 17489–17504, doi:10.1029/98JA00999, 1998.

[3] Hayakawa, M., Kasahara, Y., Nakamura, T., Muto, F., Horie, T., Maekawa, S., Hobara, Y., Rozhnoi, A. A., Solovieva, M., and Molchanov, O. A., “A statistical study on the correlation between lower ionospheric perturbations as seen by subionospheric VLF/LF propagation and earthquakes, J. Geophys. Res., 115, A09305, doi:10.1029/2009JA015143, 2010.

[4] K. Motojima and N. Haga, “Stochastic relation between anomalous propagation in the line-of-sight VHF radio band and occurrences of earthquakes,” Nat. Hazards Earth Syst. Sci., 14, 2119–2124, 2014, doi:10.5194/nhess-14-2119-2014, 2014.

[5] Yasuda, Y., Ida, Y., Goto, T., and Hayakawa, M., “Interferometric direction finding of over-horizon VHF transmitter signals and natural VHF radio emissions possibly associated with earthquakes,” Radio Sci., 44, RS2009, doi:10.1029/2008RS003884, 2009.

[6] Yonaiguchi, N., Ida, Y., and Hayakawa, M., “On the statistical correlation of over-horizon VHF signals with meteorological radio ducting and seismicity,” J. Atmos. Sol-terr. Phys., 69, 661–674, doi:10.1016/j.jastp.2007.01.007, 2007.

[7] Peng Han, Katsumi Hattori, Jiancang Zhuang, Chieh-Hung Chen, Jann-Yenq Liu, and Shuji Yoshida, “Evaluation of ULF seismo-magnetic phenomena in Kakioka, Japan by using Molchan’s error diagram,” Geophysical Journal International, doi: 10.1093/gji/ggw404, 2017.

Lithosphere-Atmosphere-Ionosphere (LAI) Coupling during Extreme Geophysical Events: Atmospheric Gravity Waves and Implications for Disaster Risk Reduction (DRR)

Y. Hobara[1,2,3,4], A. D. Setiawan[1], S. Sasmal[5], and A. Shvets[6]
[1] Graduate School of Informatics and Engineering, The University of Electro-Communications (UEC), Japan
[2] Earth Environment Research Station, UEC, Japan
[3] Center for Space and Radio Engineering (SSRE), UEC, Japan
[4] Research Center for Realizing Sustainable Societies, UEC, Japan
[5] Institute of Astronomy Space and Earth Science, India
[6] O. Ya. Usikov Institute for Radio physics and Electronics, Ukraine
Corresponding author: hobara@ee.uec.ac.jp

This paper presents recent multi-instrumental observational findings on the coupling mechanisms among the lithosphere, atmosphere, and ionosphere (LAI coupling), aiming to contribute to Disaster Risk Reduction (DRR). We analyze three distinct types of geophysical hazards: (1) earthquakes, (2) volcanic eruptions, and (3) tropical cyclones (TCs). The University of Electro-Communications (UEC) operates an extensive electromagnetic observation network across Japan, utilizing a dense VLF/LF transmitter signal network to monitor lower ionospheric perturbations in the D and E regions. These observations are integrated with lightning data from the Japanese Total Lightning Network (JTLN, connected to ENTLN), atmospheric electric field (AEF) measurements, and infrared sensor data from the Himawari-8 satellite. Notably, our analysis reveals Internal Gravity Waves (IGWs) as a dominant component of atmospheric gravity waves (AGWs) excited during these extreme events. By synthesizing these multi-parameter datasets, this study identifies unique ionospheric signatures originating from lithospheric and atmospheric drivers. These insights into vertical coupling processes provide a scientific foundation for developing novel monitoring and early-warning capabilities, ultimately advancing Disaster Risk Reduction (DRR) for extreme geophysical events.

Pre-seismic Gravity Wave Activity before the 2024 Noto Peninsula Earthquake

Shih-Sian Yang [1,2,3], Yasuhide Hobara [4,5,6], Sudipta Sasmal [2,3,7], Stelios M. Potirakis [8], and Masashi Hayakawa [2,3,9]

[1]Solar Sharing, Co. Ltd., Jhongli, Taoyuan City 320953, Taiwan
[2]Hayakawa Institute of Seismo Electromagnetics, Co., Ltd. (Hi-SEM), Chofu, Tokyo 182-0026, Japan
[3]QuakeInsight Tokyo, Chofu, Tokyo 182-0026, Japan
[4]Graduate School of Informatics and Engineering, The University of Electro-Communications (UEC), Chofu, Tokyo 182-8585, Japan
[5]Center for Space Science and Radio Engineering, UEC, Chofu, Tokyo 182-8585, Japan
[6]Research Center for Realizing Sustainable Societies, UEC, Chofu, Tokyo 182-8585, Japan
[7]Institute of Astronomy Space and Earth Science, Kolkata 700054, India
[8]Department of Electrical and Electronics Engineering, University of West Attica, 12241 Athens, Greece
[9]Advanced Wireless and Communication Research Center (AWCC), UEC, Chofu, Tokyo 182-8585, Japan
Corresponding author: yang.sirius.sian@gmail.com

This study aims to identify the possible atmospheric gravity wave (AGW) activities in the stratosphere and upper ionosphere before the magnitude 7.6 Noto Peninsula earthquake (EQ) on 1 January 2024. For the stratospheric part, we employed the temperature profiles from the ERA5 reanalysis dataset to evaluate the potential energy (E_P) of AGW activity. We found AGW activity around the EQ epicenter enhanced at 19 km altitude 15, 11, and 10 days before the EQ, as well as at multiple altitudes of 20, 24, 28, and 33 km 1 day before the EQ (31 December 2023). For the ionospheric part, we used oblique ionosonde data sounding at Wakkanai and Yamagawa with an assumed one-hop reflection point (ORP) only 169 km away from the EQ epicenter, which was not covered by vertical ionosonde observations. The NmF2 at ORP was analyzed. We found a long-lasting negative anomaly from the preceding day (31 December 2023) to the EQ occurrence, which was 3.37 standard deviations below the previous 30-day mean. We also found a positive anomaly 2 days before the EQ. In addition, we observed a new type of NmF2 anomaly around midday, which has not yet been reported in the literature. The midday NmF2 was anomalous for 10, 8 days, and a few hours before the EQ, implying possible pre-seismic modifications of the mesospheric meridional neutral wind. Since both positive and negative anomalies were observed before the EQ, pre-seismic atmospheric gravity wave (AGW) activity shall be the main agent driving lithosphere-atmosphere-ionosphere coupling (LAIC) processes. This supposition is supported by abnormal stratospheric AGW activity observed 10 and 1 day before the EQ, consistent with ionospheric NmF2 anomalies on the same days. Unfortunately, the solar and geomagnetic activity was relatively high 11–15 days before the EQ, so we cannot verify the upper ionospheric abnormality, as pre-seismic AGW activity was also found in the stratosphere 15 days before the EQ. In summary, both the stratosphere and ionosphere show anomalous behaviors related to AGW activities before the EQ. We can conclude that pre-seismic AGWs play an important role in the LAIC process before the 2024 Noto Peninsula EQ.

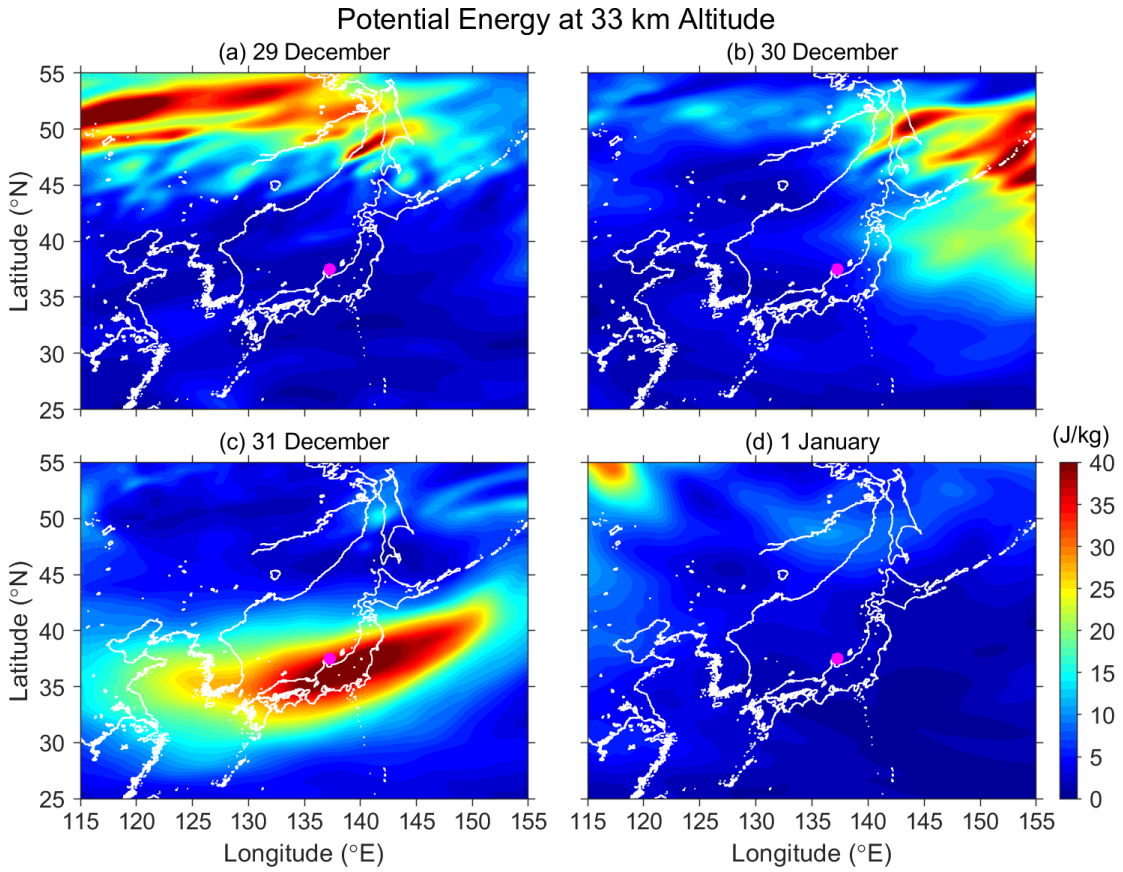


Figure 1. The atmospheric gravity wave (AGW) potential energy (E_P) at 33 km altitude from 29 December 2023 to 1 January 2024 (the earthquake (EQ) day). Strong AGW activity was found at this altitude 1 day before the EQ.

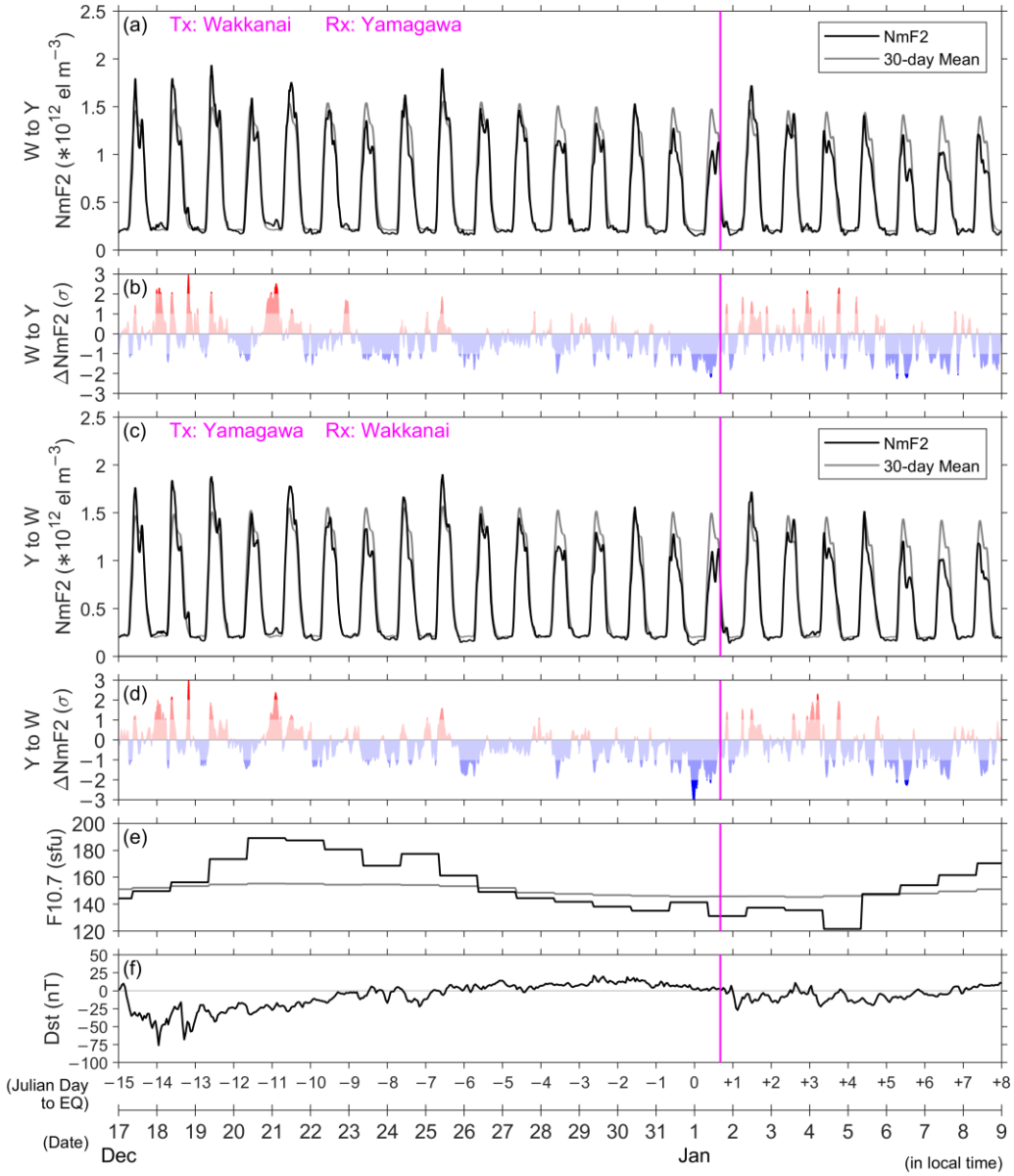


Figure 2. The time series from 17 December 2023 to 8 January 2024, which is from 15 days before to 7 days after the EQ. Panels (**a**,**b**) plot the NmF2 and normalized deviation of NmF2 (ΔNmF2) sounded by radio waves transmitted at Wakkanai and received at Yamagawa (W to Y), whereas panels (**c**,**d**) plot the same parameters sounded by radio waves transmitted at Yamagawa and received at Wakkanai (Y to W); panels (**e**,**f**) plot the F10.7 and Dst indices, respectively. In each panel, the vertical magenta line indicates the occurrence of the EQ. In panels (**a**,**c**), the gray curve plots the reference value, which is the mean NmF2 of the preceding 30 days. In panels (**b**,**d**), the red and blue areas represent positive and negative deviations, respectively, and different shades of color are used to emphasize the degree of deviation. In panel (**e**), the gray curve plots the mean F10.7 of the preceding 30 days. In panel (**f**), the horizontal gray line plots 0 nT for reference.

References

[1] Yang, S.-S., Hobara, Y., Sasmal, S., Potirakis, S. M., & Hayakawa, M. (2026). Anomalies on ionospheric electron density before the 2024 Noto Peninsula earthquake using oblique ionosondes. *Atmosphere*, *17*(7), 671. https://doi.org/10.3390/atmos17070671

[2] Yang, S.-S., Hobara, Y., Sasmal, S., Potirakis, S. M., & Hayakawa, M. (2026). Stratospheric gravity wave activity before the 2024 Noto Peninsula earthquake. Unpublished paper.

Multiparameter Lithosphere–Atmosphere–Ionosphere Coupling Signatures Associated with Three 2026 Earthquakes in Japan

Sudipta Sasmal[1,2,3], Kousik Nanda[1,4], Masashi Hayakawa[2,5,6], Stelios M. Potirakis[3,7]
Hideaki Hinata[2] and Yasuhide Hobara[8]

[1]Institute of Astronomy Space and Earth Science, Kolkata, India
[2]QuakeInsight Tokyo, UEC Alliance Center, Tokyo, Japan
[3]Department of Electrical and Electronics Engineering, University of West Attica, Egaleo, Greece
[4]Department of Computer Science and Application, Prabhat Kumar College, Contai, India
[5] Hayakawa Institute of Seismo Electromagnetics, Co., Ltd., UEC Alliance Center, Tokyo, Japan
[6]Department of Information and Networking, The University of Electro-Communications, Tokyo, Japan
[7]Institute for Astronomy, Astrophysics, Space Applications and Remote Sensing, National Observatory of Athens, Athens, Greece
[8]Center for Space and Radio Engineering, The University of Electro-Communications, Tokyo, Japan
Corresponding author: meet2ss25@gmail.com

The Lithosphere–Atmosphere–Ionosphere Coupling (LAIC) framework provides a physical basis for investigating whether earthquake preparation is accompanied by temporally organized disturbances extending from the lower atmosphere to the mesosphere, thermosphere, and ionosphere. This study examines three 2026 Japanese earthquakes using a common multiparameter methodology: the 16 June 2026 Ibaraki earthquake (M 5.3; 36.171°N, 139.699°E; depth 10 km), the 18 April 2026 Nagano earthquake (M 4.9; 36.6°N, 137.9°E; depth 10 km), and the paired 26 June 2026 Yokaichiba–Yamanashi earthquakes (M 5.8 and M 5.2; depths 43 km). The observational framework combines lower-atmospheric thermal parameters, atmospheric-gravity-wave activity, VLF/LF nighttime propagation anomalies, Global Ionospheric Map and GPS/IGS total electron content, and TIMED/SABER mesosphere–thermosphere measurements. Temperature, relative humidity, and atmospheric chemical potential are used to characterize thermal anomalies; atmospheric-gravity-wave activity is treated as a dynamical/acoustic proxy; VLF/LF propagation is quantified using normalized Trend, Dispersion, and Nighttime Fluctuation indices; and ionospheric disturbances are evaluated using regional and station-based TEC measurements. We examine geomagnetic conditions as an essential environmental control so we can interpret near-event ionospheric and VLF changes in the context of quiet or disturbed space-weather conditions.

The Ibaraki earthquake shows the clearest short-lead multiparameter sequence. About 10–11 days before, a geomagnetic disturbance occurred with Kp at 6.2, 3-hourly Ap at 82, daily Ap at 32, IMF Bz at 18, and Dst around -60 nT. The immediate pre-earthquake period was quieter, with Kp dropping to 1 a day before and Ap staying low. In this interval, the surface-temperature difference sharply fell to -7 K the day before and stayed near -6 K on the day. Humidity modestly decreased by 5–10%, while ACP remained steady without a clear precursor.

In Ibaraki, atmospheric and ionospheric responses occurred at different times. AGW structures of about 16–18 in the proxy appeared days before the event at 41–48 km altitude, followed by a broader 14–16 feature that persisted through the earthquake and peaked near 46.3 km. VLF/LF data showed an electromagnetic precursor, with the Nighttime Fluctuation parameter peaking around +4σ on 12 June 2026, four days before

the quake, and a nearby negative Trend. Dispersion was below the anomaly threshold, indicating enhanced nighttime signals rather than a uniform VLF anomaly. Ionospheric changes lagged: six IGS stations peaked about two days before the quake, with TEC anomalies of 6.2–8.9 TECU, and a GIM point near the epicenter reached 8 TECU a day prior. TIMED/SABER data revealed a minimum mesospheric temperature of 165 K at 83 km on quake day, with OH reaching 3.6 units at 86 km and O3 1.7 units at 91 km a day before. Overall, these findings show a sequence: VLF and atmospheric changes days ahead, regional TEC perturbations closer to the quake, followed by mesospheric variability around and after the mainshock.

The Nagano earthquake displays an earlier multiparameter anomaly cluster. The final 1–2 days before the earthquake were comparatively quiet, with Kp reaching 0, 3-hourly Ap near 0–10, and daily Ap approximately 5–8, whereas the earthquake day became strongly geomagnetically disturbed, with Kp near 6, Ap reaching 60, daily Ap around 35, IMF Bz approximately 15, and Dst decreasing to about -100 nT. Thermal anomalies were strongest earlier: temperature reached about +7 K seven days before, relative humidity increased by +10–20% three days before after an earlier dry period, and ACP reached about +0.04 eV seven days before.

The Nagano VLF/LF response was clear. On the Osaka–JJY path, normalized Dispersion increased to +3σ, and Nighttime Fluctuation reached about +3 to +3.5σ around 13 April 2026, 5 days before the earthquake, while the Trend stayed within statistical limits. This DP–NF enhancement coincides with elevated AGW, thermal, and ionospheric parameters. The AGW field was up to about 14, 5–7 days before, and the GIM grid point 5.57 km from the epicenter reached 9 TECU seven days before. MSSA00JPN and USUD00JPN showed maxima of approximately 12 and 11 TECU, respectively. SABER measurements showed a temperature minimum of 195 K at 86 km two days before, then a maximum of 209 K one day after, with OH increasing from 2.0 to 3.3 units. Nagano exhibits a coherent anomaly cluster 5–7 days before the earthquake involving lower-atmospheric, VLF, AGW, and TEC parameters. The long lead time and disturbed geomagnetic conditions on the earthquake day warrant caution in interpreting observations.

The paired Yokaichiba–Yamanashi earthquakes show a more complex response. The thermal field shifted from an earlier positive temperature anomaly of about +3 K to a pronounced negative anomaly of approximately -6 K in the days immediately preceding the earthquakes. Relative humidity shifted from about 10–20% below the reference to about 15–20% above it on the earthquake day, while ACP reached its strongest positive pre-event difference of approximately 0.01–0.015 eV two to three days before, then decreased to about -0.02 eV on the event day. AGW activity persisted across the earthquake interval, with a long-lived 12–18 feature between approximately 42 and 48 km, rather than a short, isolated pre-event enhancement.

The VLF/LF observations for this case differ markedly from those for Ibaraki and Nagano. On the Chofu–NWC path, none of the normalized Trend, Dispersion, or Nighttime Fluctuation parameters clearly exceeded the adopted ±3σ anomaly threshold. Several moderate enhancements approached +2 to +2.5σ, but no robust, coherent threshold-level pre-earthquake VLF anomaly was identified. The GIM TEC response was stronger: the grid point located 2.71 km from the midpoint of the two epicenters reached approximately 8 TECU one day before, with continuous anomalies of about 6–8 TECU spanning the near-event interval. However, the six GPS/IGS stations did not show a common pre-event temporal pattern, and their largest anomalies were predominantly post-event, reaching up to 10.5 TECU at MSSA00JPN. SABER observations showed a minimum mesospheric temperature of approximately 165 K at 86 km two days before and one day after the earthquakes, while the maximum temperature, approximately 178 K at 86 km, occurred one day before. O3 also reached a pre-event maximum, whereas OH and NO enhancements were mainly post-event. Enhanced geomagnetic activity

immediately before the earthquakes further complicates interpretation of the ionospheric response, with Kp near 4.9, 3-hourly Ap near 48, and IMF Bz approximately 15–18.

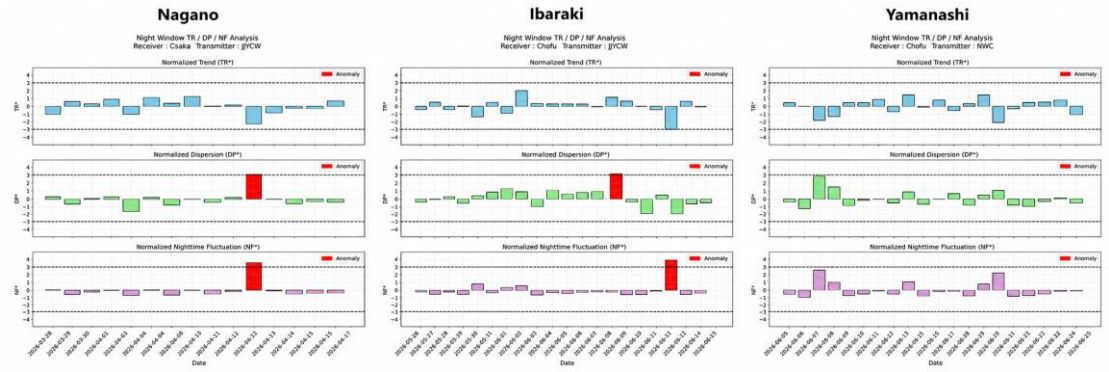


Figure 1. Normalized Trend, Dispersion, and NF anomaly as recorded from the QIT VLF network.

Comparison of the three cases shows that the strongest evidence comes from the temporal coherence across independent channels, not any single parameter. Ibaraki exhibits a compact sequence with a VLF NF anomaly (~+4σ) about 4 days prior, followed by station-based TEC anomalies (~2 days before), and an GIM anomaly (8 TECU) a day prior under quiet geomagnetic conditions. Nagano features an earlier, broader sequence with a VLF DP–NF anomaly (~+3 to +3.5σ) around 5 days before, plus thermal, AGW, GIM, and GPS/IGS anomalies around 5–7 days prior. Yokaichiba–Yamanashi shows a thermal and GIM response but lacks a strong VLF anomaly or coherent multi-station GPS response, with increased geomagnetic activity complicating interpretation.

The three earthquakes demonstrate the event-dependent nature of LAIC responses, showing variations in thermal changes, AGW structures at ~40–50 km, VLF/LF anomalies, TEC perturbations, and mesospheric temperature and composition. VLF results support a multiparameter view, especially for Nagano and Ibaraki, with anomalies matching atmospheric and ionospheric disturbances. The lack of strong VLF responses in Yamanashi emphasizes the value of negative or weak signals in cross-channel analysis. These findings endorse a probabilistic, event-dependent LAIC framework, relying on cross-layer timing, spatial coherence, geomagnetic screening, and independent confirmation across thermal, acoustic, electromagnetic, and plasma data for reliable earthquake disturbance assessment.

Parameter / Domain	Nagano	Ibaraki	Yokaichiba–Yamanashi
Geomagnetic conditions	Pre-event comparatively quiet during final 1–2 d: Kp = 0 at −2 d, 3-h Ap ~0–10, daily Ap ~5–8. Earlier disturbance: Kp up to 6.1, Ap up to 90, Dst ~−90 nT at ~−14 d. EQ day strongly disturbed: Kp ~6, Ap 60, daily Ap 35, IMF Bz 15, Dst ~−100 nT.	Immediate pre-event period comparatively quiet: Kp = 1 at −1 d with low Ap. Earlier disturbance ~10–11 d before: Kp 6.2, 3-h Ap 82, daily Ap 32, IMF Bz 18, Dst ~−60 nT.	Enhanced geomagnetic activity close to event: Kp 4.9, 3-h Ap 48, daily Ap reported 25, IMF Bz 15–18 at −1 d; Dst ~−30 to +20 nT. Daily-Ap summary internally inconsistent and should be treated cautiously.
Thermal parameters (Temperature + RH + ACP)	Temperature: ~+7 K at −7 d, approaching ~0 before event. RH: ~20–30% lower at −7 to −5 d, then +10–20% at −3 d; ~−15% on event day. ACP: +0.04 eV at −7 d, decreased and then recovered.	Temperature: sharp decrease to ~−7 K at −1 d; ~−6 K on event day. RH: modest ~−5 to −10% pre-event decrease; no clear event-day anomaly. ACP: no distinct pre-event maximum.	Temperature: ~+3 K at −5 d, then ~−6 K during −4 to −1 d; ~−4 K on event day. RH: ~−10 to −20% at −3 d, then +15–20% on event day. ACP: +0.01–0.015 eV at −2 to −3 d; ~−0.02 eV on event day.
AGW	Pre-event enhancement ~8–14 at ~39–48 km, strongest ~−5 to −7 d; stronger co-/post-event	Pre-event ~16–18 J kg^{-1} at ~41–48 km, ~−4 to −7 d; persistent 14–16 feature across	Long-lived 12–18 patch at ~42–48 km spanning pre-, co-, and post-

Parameter / Domain	Nagano	Ibaraki	Yokaichiba–Yamanashi
	feature followed.	event interval.	event periods.
VLF/LF anomalies	Osaka–JJY: TR* no robust threshold anomaly; DP* ∼+3σ at −5 d; NF* ∼+3 to +3.5σ at −5 d. Overall: clear coupled DP*–NF* anomaly.	Chofu–JJY: TR* pronounced negative excursion near anomaly interval; DP* no clear threshold anomaly; NF* nearly +4σ at −4 d. Overall: clear dominant NF* anomaly.	Chofu–NWC: TR* no robust threshold anomaly; DP* moderate enhancement <+3σ; NF* ∼+2 to +2.5σ, below threshold. Overall: no robust ±3σ VLF anomaly.
VTEC / TEC	GIM: 9 TECU at −7 d; post-event maximum 10.2 TECU. GPS/IGS: 12 TECU at MSSA00JPN and 11 TECU at USUD00JPN at −7 d. Two-station common early response.	GIM: 8 TECU at −1 d; 4.2 TECU on event day. GPS/IGS: coherent six-station response at −2 d, maximum 8.9 TECU at TKBG00JPN. Strongest regional ionospheric coherence.	GIM: 8 TECU at −1 d; continuous ∼6–8 TECU around event. GPS/IGS: no common pre-event maximum; largest anomalies mainly post-event, up to 10.5 TECU at MSSA00JPN.
TIMED/SABER outputs	Temperature: 195 K at 86 km, −2 d; 209 K at +1 d. OH: 2.0 units at 88 km, −2 d → 3.3 at 86 km, +1 d. O_3: no distinct pre-event maximum reported. NO: maximum mainly post-event.	Temperature: 165 K at 83 km on event day; ∼180 K at 85 km, +1 d. OH: 3.6 units at 86 km, −1 d → 0.8 on event day. O_3: 1.7 units at 91 km, −1 d. NO: ∼0.75 near event → ∼1.0 at +2 d.	Temperature: 165 K at 86 km at −2 d and +1 d; 178 K at −1 d. OH: maximum 3.7 units at +1 d. O_3: 1.18 units at 91 km, −1 d → 0.79 on event day. NO: 0.88 on event day → 1.2 at +1 d.
Dominant anomaly window	∼5–7 d before.	∼1–4 d before.	∼1–5 d before, but mixed.
Cross-channel coherence	High–moderate: thermal + ACP + AGW + VLF + TEC cluster in similar early window.	High: VLF → coherent GPS/IGS TEC → GIM TEC close to event under comparatively quiet geomagnetic conditions.	Moderate/complex: thermal + ACP + AGW + GIM, but weak VLF and no common IGS precursor; geomagnetic activity complicates interpretation.
Overall interpretation	Early multiparameter precursor-like cluster; event-day geomagnetic disturbance mainly affects co-/post-event interpretation.	Most coherent short-lead multiparameter sequence, with strong temporal ordering and relatively quiet immediate pre-event geomagnetic conditions.	Mixed multiparameter response; thermal/GIM changes are clear, but geomagnetic activity and weak VLF/IGS coherence reduce confidence.

Table 1. Compact integrated comparison of various parameters for the three earthquake cases.

References

[1] S. Sasmal, S. Chowdhury, S. Kundu, D. Z. Politis, S. M. Potirakis, G. Balasis, et al., "Pre-seismic irregularities during the 2020 Samos (Greece) earthquake (M = 6.9) as investigated from multi-parameter approach by ground and space-based techniques," Atmosphere, vol. 12, Art. no. 1059, 2021.

[2] M. Hayakawa, O. A. Molchanov, T. Ondoh, and E. Kawai, "The precursory signature effect of the Kobe earthquake on VLF sub-ionospheric signals," Journal of the Communications Research Laboratory, vol. 43, pp. 169–180, 1996.

[3] S. Sasmal, S. Chowdhury, S. Kundu, S. Ghosh, D. Politis, S. Potirakis, et al., "Multi-parametric study of seismogenic anomalies during the 2021 Crete earthquake (M = 6.0)," Annals of Geophysics, vol. 66, Art. no. SE646, 2023.

[4] M. Hayakawa, A. Schekotov, J. Izutsu, S. Yang, M. Solovieva, and Y. Hobara, "Multi-parameter observations of seismogenic phenomena related to the Tokyo earthquake (M = 5.9) on 7 October 2021," Geosciences, vol. 12, Art. no. 265, 2022.

[5] M. Hayakawa, M. Solovieva, G. Kopylova, S. Hirooka, S. Sasmal, K. Nanda, et al., "Multi-parameter and multi-layer observations of electromagnetic precursors to a huge Hokkaido earthquake (M = 6.7) on 5 September 2018, and lithosphere–atmosphere–ionosphere coupling channel," Atmosphere, vol. 16, Art. no. 1372, 2025.

[6] S. Sasmal, K. Nanda, M. Hayakawa, M. Solovieva, G. Kopylova, and S. M. Potirakis, "Towards understanding earthquake preparatory dynamics: A multi-parametric investigation of the 2025 Kamchatka Mw 8.8 event," Atmosphere, vol. 16, Art. no. 1328, 2025.

Meteorological anomalies associated with earthquakes with the use of AMeDAS data, and Lithosphere-Atmosphere-Ionosphere Coupling channels

M. Hayakawa[1,2], H. Hinata[1], S. Hirooka[3,4,1], S. M. Potirakis[5,6,1], and Y. Hobara[2,7]

[1] QuakeInsight Tokyo, UEC Alliance Center #501, 1-1-1 Kojima-cho, Chofu Tokyo, 182-0026, Japan
[2] Department of Computer and Network Engineering, The University of Electro-Communications (UEC), 1-5-1 Chfugaoka, Chofu Tokyo, 182-8585, Japan
[3] HiSR Inc., 1-33 Yayoi-cho, Inage-ku, Chiba 263-8522, Japan
[4] Graduate School of Science, Chiba University, Chiba, Japan
[5] Department of Electrical and Electronics Engineering, Ancient Olive Grove Campus, University of West Attica, Athens, Greece
[6] Institute for Astronomy, Astrophysics, Space Applications and Remote Sensing, National Observatory of Athens, Metaxa and Vasileos Pavlou, Athens, Greece
[7] Center for Space Science and Radio Engineering, UEC, Tokyo, Japan
Corresponding author: hayakawa@quakeinsight.tokyo

Abstract

The purpose of this paper is to discuss the effect of earthquake (EQ) preparation on changes in meteorological parameters with the use of ground-based data. The two physical quantities of temperature (T)/relative humidity (RH) and atmospheric chemical potential (ACP) have been investigated with making full use of the Japanese meteorological "open" data of AMeDAS (Automated Meteorological Data Acquisition System), which is a very dense "ground-based" network of meteorological stations with higher temporal and spatial resolutions than the satellite remote sensing open data. In order to obtain a clearer identification of any seismogenic effect, we have used the AMeDAS station data at local midnight (LT = 01 h) and our initial target EQ was chosen to be the famous 1995 Kobe EQ of 17 January 1995 (M = 7.3). Initially, we performed conventional statistical analysis with confidence bounds and it was found that the Kobe station (very close to the EQ epicenter) exhibited conspicuous anomalies in both physical parameters on 10 January 1995, just one week before the EQ, exceeding m (mean) + 3σ (standard deviation) in T/RH and well above m + 2σ in ACP within the short-term window of one month before and two weeks after an EQ. When looking at the whole period of over one year including the day of the EQ, only in the case of T/RH we detected three additional extreme anomalies, except in winter, but with unknown origins. On the other hand, the anomalous peak on 10 January 1995 was the largest for ACP. Further, the spatial distributions of the anomaly intensity of the two quantities have been presented using about 40 stations to provide a further support to the close relationship of this peak with the EQ. The above statistical analysis has been compared with an analysis with recent machine/deep learning methods. We have utilized a combinational use of NARX (Nonlinear Autoregressive model with eXogenous inputs) and Long Short-Term Memory (LSTM) models, which was successful in objectively re-confirming the anomalies in both parameters on the same day prior to the EQ. The combination of these analysis results elucidates that the meteorological anomalies on 10 January 1995 are considered to be a notable precursor to the EQ. Finally, we suggest a joint examination of our two meteorological quantities for their potential use in real short-term EQ prediction, as well as in the future lithosphere–atmosphere–ionosphere coupling (LAIC) studies as the information from the bottom part of LAIC.

Further re-examination studies on the precursors to the 1995 Kobe EQ have been performed, and we then aim to combine the detailed temporal evolution of these meteorological anomalies with earlier results on lower ionospheric perturbations observed via VLF propagation and sporadic E layer formation (together with other electromagnetic precursors). And we come to a conclusion that a diffusion-type "slow channel" in the LAIC exists for this Kobe EQ, with Earth's surface

meteorological anomalies preceding ionospheric perturbations by 3 - 5 days, possibly related to radon exhalation. Further discussions have been performed on further details of the mechanism of this LAIC channel for the Kobe EQ, and other EQ events.

References

[1] M. Hayakawa, S. Hirooka, K. Michimoto, S. M. Potirakis, and Y. Hobara, "Meteorological Anomalies during Earthquake Preparation: A Case Study for the 1995 Kobe Earthquake (M = 7.3) Based on Statistical and Machine Learning-Based Analyses," *Atmosphere*, vol. 16, Article 88, 2025. https://doi.org/10.3390/atmos16010088

[2] M. Hayakawa and Y. Hobara, "Integrated Analysis of Multi-Parameter Precursors to the Fukushima Offshore Earthquake (M = 7.3) on 13 February 2021 and Lithosphere-Atmosphere-Ionosphere Coupling Channels," *Atmosphere*, vol. 15, Article 1015, 2024. https://doi.org/10.3390/atmos15081015

[3] M. Hayakawa, S. M. Potirakis, S. Hirooka, and Y. Hobara, "Meteorological Anomalies Based on Ground-Based AMeDAS Data for the 1995 Kobe Earthquake: Critical Natural Time Analysis," *Open Journal of Earthquake Research (OJER)*, vol. 14, no. 2, pp. 67–84, 2025. https://www.scirp.org/journal/ojer

[4] H. Hinata, K. Michimoto, Y. Ozawa, and M. Hayakawa, "A Study on Lithosphere-Atmosphere-Ionosphere Coupling Channel for the 1995 Kobe Earthquake, by Including Ground-Based Meteorological Anomalies," *Open Journal of Earthquake Research (OJER)*, vol. 14, no. 2, pp. 85–105, 2025. https://www.scirp.org/journal/ojer

Ionospheric Anomalies Preceding the 1944 Tonankai and 1945 Mikawa Earthquakes Revealed by Handwritten Ionogram Analysis

Ken Umeno
Kyoto University, Kyoto, Japan
Corresponding author: umeno.ken.8z@kyoto-u.ac.jp

We report quantitative evidence of pre-seismic ionospheric anomalies prior to two major historical earthquakes in Japan: the 1944 Tonankai Earthquake (M7.9) and the 1945 Mikawa Earthquake (M7.1). By digitizing and analyzing handwritten ionograms archived by NICT from Kokubunji and Hiratsuka observatories, we discovered significant enhancements in electron density (calculated via critical frequency $N = 1.24 \times 10^{10}\ f_c^2$) occurring 1 to 2 hours before mainshocks. These ionospheric anomalies correlate temporally with pre-seismic ground tilt changes recorded during leveling surveys in 1944 by A. Imamura and K. Mogi, providing direct evidence of pre-slip activity. Furthermore, these historical findings exhibit remarkable physical consistency with recent observations during the 2011 Tohoku-Oki (M9.1) and 2024 Noto Peninsula (M7.6) earthquakes, as well as the proposed electrostatic lithosphere-ionosphere coupling model. This retrospective study validates pre-seismic ionospheric anomaly detection as a robust physical marker for mega-thrust earthquake early warning systems.

1. Introduction and Background

Pre-seismic ionospheric anomalies have drawn significant attention over the past two decades. Advanced GNSS-TEC networks and digital ionosondes have detected distinct precursors prior to major earthquakes, such as the 2011 M9.1 Tohoku-Oki earthquake (Bletery & Nocquet 2023; Tanaka & Umeno 2025; Ikeda & Umeno 2025) and the 2024 M7.6 Noto Peninsula earthquake. However, whether such ionospheric precursors consistently occurred prior to historical mega-thrust events before the satellite era remained unverified. In this study, we re-examine WWII-era ionospheric observations in Japan to test the reproducibility of pre-seismic coupling mechanisms across an 80-year horizon.

2. Historical Observational Network and Geodetic Data

During World War II, Japan established an extensive ionospheric observation network across Asia and the Pacific, including 14 operational stations such as Kokubunji, Hiratsuka, and Manila (Ishii et al., 2021). On December 7, 1944, the M7.9 Tonankai earthquake struck the Nankai Trough. Geodetic leveling conducted near Kakegawa by the Land Survey Department—initiated by Akitsune Imamura—recorded anomalous ground tilt starting 3 hours prior to the mainshock, accelerating 10 minutes before failure (Mogi 1982). This provided rare direct geodetic evidence of pre-slip.

Event / Date	Mag.	Primary Pre-Seismic Data Source	Lead Time	Geodetic / Physical Signature
1944 Tonankai (Dec 7)	M7.9	Handwritten Ionograms (Kokubunji/Hiratsuka)	1–2 hours	Ground tilt (Imamura/Mogi pre-slip)
1945 Mikawa (Jan 13)	M7.1	Handwritten Ionograms (Hiratsuka Station)	1–2 hours	Coseismic surface faulting & waveforms
2011 Tohoku-Oki (Mar 11)	M9.1	GNSS-TEC (GEONET) & Oblique Ionograms	~80 min	Correlation Analysis (CRA) pre-slip signal
2024 Noto Peninsula (Jan 1)	M7.6	Digital Ionosondes (Wakkanai - Yamagawa)	~1.5 hours	Dual F-layer structure & 20km height drop

3. Analysis of Handwritten Ionograms (1944 & 1945)

We digitized and analyzed archival frequency-height (f-h) curves recorded at Kokubunji and Hiratsuka for December 7, 1944 (Tonankai) and January 12–13, 1945 (Mikawa). The plasma density is directly proportional to the square of the critical frequency f_c: $N_{max} = 1.24 \times 10^{10} f_c^2$ [electrons/m^3].

For the 1944 Tonankai earthquake (13:36 JST), ionograms recorded at 12:00 and 12:30 JST exhibit a sudden upward shift in f_oF2, indicating a localized electron density surge 1–2 hours prior to the mainshock. This surge coincides precisely with the time window of ground tilt acceleration documented by Imamura. Similarly, for the 1945 Mikawa earthquake (03:38 JST), Hiratsuka ionograms around 02:30 JST reveal an elevated critical frequency relative to baseline days, confirming pre-seismic ionospheric perturbations.

Key Finding: Reproducible Pre-Seismic Ionospheric Signatures

Handwritten ionograms from 1944 and 1945 demonstrate that pre-seismic ionospheric anomalies are intrinsic physical phenomena preceding large earthquakes, rather than modern instrumental artifacts. The observed 1–2 hour lead time in historical records matches modern GNSS/ionosonde observations for M7.6–M9.1 events.

4. Electrostatic Lithosphere-Ionosphere Coupling

The observed concurrence of pre-slip and ionospheric anomalies aligns with the physical model of electrostatic lithosphere-atmosphere-ionosphere coupling (Mizuno, Kao, & Umeno 2026). Under high temperature and pressure in the focal region prior to mainshock rupture, deep fluids transition into supercritical water, forming an effective subsurface capacitive layer. Pre-slip generates positive charge accumulation at the surface, producing electric fields that draw electrons downward from the F-layer and alter total electron density profiles. This mechanism explains both the historical 1944/1945 ionospheric spikes and the dual F-layer altitude drops observed prior to the 2023 and 2024 Noto earthquakes.

5. Conclusion and Applications to Nankai Trough Early Warning

This retrospective analysis establishes that pre-seismic ionospheric anomalies preceded the 1944 Tonankai and 1945 Mikawa earthquakes by 1 to 2 hours. By validating these anomalies against 1944 geodetic leveling data, we confirm that integrating real-time ionospheric monitoring with geodetic network analysis can provide actionable early warnings for future Nankai Trough mega-thrust earthquakes (M8–9 class), significantly contributing to disaster mitigation.

References

[1] M. Ishii et al., *Radio Science*, vol. 56, DOI: 10.1029/2020RS007162, 2021.

[2] A. Mizuno, M. Kao, and K. Umeno, *Int. J. Plasma Environ. Sci. Technol.*, 20(1), 01003, 2026.

[3] H. Tanaka and K. Umeno, AGU24 Presentation, 2024 and *Preprint*, 2025, https://essopenarchive.org/doi/abs/10.22541/essoar.176296628.85631921/v3 ; S. Ikeda and K. Umeno, *AGU25 Presentation*, 2025.

[4] K. Mogi, *Bull. Earthq. Res. Inst. Univ. Tokyo*, 1982.

[5] Q. Bletery and A. Nocquet, *Science*, 381, 186–189, 2023.

An Automated Software Framework for the QuakeInsight Tokyo (QIT) Earthquake Dashboard

Sudipta Sasmal[1,2,3], Arnab Bhattacharyya[1], Kousik Nanda[1,4], Masashi Hayakawa[2,5,6], Hideaki Hinata[2] and Yasuhide Hobara[7]

[1]Institute of Astronomy Space and Earth Science, Kolkata, India
[2]QuakeInsight Tokyo, UEC Alliance Center, Tokyo, Japan
[3]Department of Electrical and Electronics Engineering, University of West Attica, Egaleo, Greece
[4]Department of Computer Science and Application, Prabhat Kumar College, Contai, India
[5] Hayakawa Institute of Seismo Electromagnetics, Co., Ltd., UEC Alliance Center, Tokyo, Japan
[6]Department of Information and Networking, The University of Electro-Communications, Tokyo, Japan
[7]Center for Space and Radio Engineering, The University of Electro-Communications, Tokyo, Japan
Corresponding author: meet2ss25@gmail.com

The QuakeInsight Tokyo (QIT) earthquake dashboard uses a distributed software framework for unattended acquisition, transport, processing, normalization, fusion, and visualization of diverse geophysical observations. It is designed for real-time monitoring of lithosphere-atmosphere-ionosphere coupling (LAIC) signatures, not retrospective analysis. The system ensures deterministic execution despite incomplete, delayed, or asynchronous data streams. It integrates Python for acquisition and orchestration, FTP for data transport, Linux crontab for scheduling, MATLAB for signal processing, a database for state management, and automated dashboard generation. This architecture supports various parameters like meteorological, VLF/LF, GNSS-TEC, geomagnetic, ionosonde, and satellite data, each with different cadences, latencies, and quality-control rules.

Open-source data are acquired automatically through dedicated Python downloader scripts. Each source-specific module encapsulates endpoint information, station or grid identifiers, expected temporal cadence, remote naming conventions, parsing rules, retry limits, timeout control, and local archive structure. The scripts are state-aware: before each execution they determine the latest successfully validated timestamp and request only the missing interval, avoiding unnecessary full-archive downloads. HTTP/HTTPS, FTP, API, and direct-file retrieval can be handled through separate adapters. Downloaded objects are initially written to a temporary staging area and are promoted to the immutable raw archive only after file-size checks, timestamp validation, duplicate detection, parser verification, and temporal-continuity tests. Partially transferred, malformed, or zero-length files are quarantined and logged. This architecture allows delayed source products to be backfilled automatically during subsequent runs without operator intervention.

Field-instrument data are transmitted to QIT via a Python-controlled FTP system with a server buffer. Receiver computers place files in an outbound queue. The transfer program manages file states like pending, transferring, uploaded, verified, or failed, and uploads only closed files. Temporary filenames are used during transfer and renamed after success to prevent partially transferred data entering analysis. Byte-count or checksum verification can be used before releasing a queue item. Failed transfers stay queued and are retried automatically. The server decouples instrument recording from the QIT workstation, allowing data collection to continue during maintenance or connectivity issues, with successful transfers available for later synchronization.

On the QIT side, Python synchronization services periodically inspect the back-end server, compare available files with the central archive, retrieve only unprocessed objects, validate them locally, and register their status in the processing database. Server and local directory structures follow deterministic instrument/station/date hierarchies, enabling idempotent synchronization and straightforward audit of missing intervals. This transport layer is common to VLF/LF

receiver data and can be extended to GNSS receivers, meteorological sensors, ionosonde products, or future instrumentation without modifying higher-level analysis logic.

Linux crontab is the main process scheduler. The production pipeline is broken into multiple short, recoverable jobs instead of one large executable. Typical cron groups include data acquisition, server sync, file validation, database ingestion, parameter generation, VLF/LF analysis, GNSS-TEC processing, geomagnetic screening, figure creation, dashboard refresh, archive upkeep, and health reports. Modules run at different cadences based on data availability; for example, meteorological processing is hourly after data release, while daily VLF products follow nighttime observation. Wrapper scripts set environment, directory, and logs; lock files prevent overlaps; output, errors, status, time, and module info are logged for diagnostics. After reboot, cron resumes the pipeline, and modules continue from the last validated timestamp.

The atmospheric analysis engine processes a dense regional meteorological network hourly. It ingests temperature, relative humidity, pressure (when available), geographic position, and elevation for each station, applying quality control. Derived diagnostics include specific humidity, lifting condensation level (LCL), atmospheric chemical potential (ACP), and temperature-relative-humidity indicators. Pressure can be read directly or estimated from station elevation in standard-atmosphere mode. Missing observations remain null; invalid zeros are excluded; statistical windows are accepted only if their minimum valid samples are met. The system never substitutes missing data with normal values to avoid bias and false stability.

Anomaly detection operates on multiple timescales. A 30-day moving Z-score serves as a broad screening statistic, while a 15-day robust estimator based on local median and median absolute deviation confirms detections under non-Gaussian and outlier-prone conditions. Interquartile-range limits serve as a secondary diagnostic for comparison. The engine also supports fixed-local-time residuals, allowing tracking of specific hours independently of the all-hour background, important for signals that could be diluted by diurnal variability. Thresholds, valid-sample count, window length, and timestamp are included in metadata rather than only in plotting code.

The software applies physical classification after statistical normalization. It retains sign information in specific-humidity anomalies, separating drying from moistening. Temperature and relative-humidity departures are evaluated together to classify drying, humidity-dominated drying, warming, and normal behavior. LCL acts as an environmental gate for moist or convective conditions. ACP and temperature-relative-humidity diagnostics are correlated and not counted as independent anomaly votes. The dashboard classification separates statistical extremeness from physical relevance, downgrading or excluding anomalies linked to wet or convective environments.

The VLF/LF subsystem is path-oriented. Each transmitter-receiver link is represented by transmitter frequency, receiver identifier, nominal azimuth, nighttime window, hardware capability, and analysis mode. The current architecture supports amplitude-only systems and GPS-disciplined MSK receivers. Python routines extract transmitter components, segment nighttime, normalize data, and generate trend, dispersion, and nighttime-fluctuation indices. Standardized TR*, DP*, and NF* products are computed using moving reference windows and stored with anomaly amplitude, persistence, lead time, and path identifier. For GPS-enabled systems, phase is treated as an independent observable, enabling long-term propagation monitoring with stable timing. Systems without absolute timing are explicitly flagged as amplitude-only and cannot generate phase-derived products. This prevents heterogeneous receiver configurations from being treated as analytically equivalent.

GNSS and ionospheric processing are modular. Regional GIM values and ground-station TEC estimates are kept as separate data types due to differences in resolution and uncertainty. Station processing yields vertical or residual TEC with receiver, satellite, elevation, mapping, and time metadata. Event analysis compares GIM behavior near sources with multiple GNSS stations, emphasizing multi-station timing over isolated excursions. High-rate data can analyze traveling ionospheric disturbances for period, spectral power, direction, phase speed, and inter-station coherence. Continuous wavelet transforms help identify transient oscillations in residual TEC from background variations.

Geomagnetic conditions are incorporated as a formal confidence-control layer. Kp, 3-hourly Ap, daily Ap, Dst, IMF Bz, and solar activity indices are automatically collected and synchronized to the same timeline as the atmospheric and ionospheric modules. Configurable thresholds categorize intervals as quiet, enhanced, or storm-disturbed. When an TEC or VLF anomaly occurs during active space weather, it is not removed; instead, the dashboard maintains the observation while decreasing its interpretive confidence. This approach is vital for cases where local and external forces may operate simultaneously. Satellite data such as TIMED/SABER and others can be processed via the same time-altitude interface, and low-Earth-orbit particle measurements can serve as independent validation for lightning-induced electron precipitation studies, using coincident VLF disturbances and magnetospheric particle bursts.

Cross-domain fusion is feature-based rather than a simple summation of standardized values. Observables are grouped into lower-atmospheric thermodynamics, acoustic/gravity-wave activity, subionospheric propagation, ionospheric electron content, upper-atmosphere variability, and geomagnetic forcing. Correlated variables from a common source are grouped before ranking so that several derivatives of the same temperature-humidity pair cannot artificially increase confidence. The integrated event state retains anomaly magnitude, lead time, persistence, spatial coherence, station multiplicity, receiver capability, data-quality flags, and geomagnetic context as separate attributes. If an upstream module is unavailable, the integrated state is marked incomplete or indeterminate rather than normal. This missing-state propagation is a fundamental requirement for reliable unattended monitoring.

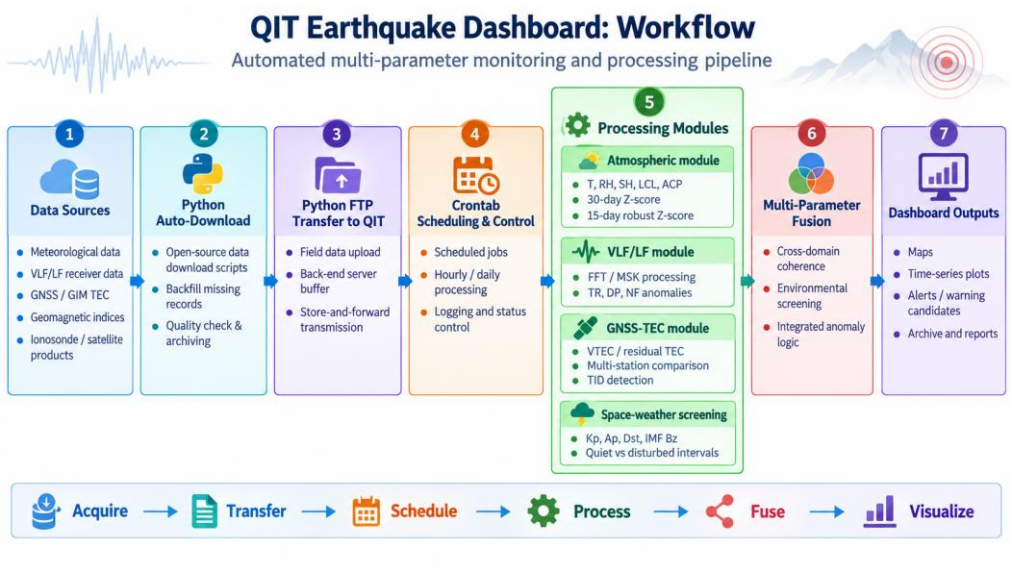


Figure 1. QIT Earthquake workflow.

In the operational QIT earthquake dashboard, the full chain therefore runs continuously as a production software service: Python scripts download external open-source data; local instruments transmit observations through the Python/FTP back-end architecture; cron jobs trigger synchronization and parameter-specific processing; numerical modules generate statistical and physical diagnostics; database records preserve provenance and process status; and dashboard routines regenerate maps, station plots, VLF products, TEC summaries, geomagnetic-context panels, and integrated alert states. Incremental processing limits computational cost because only newly arrived observations and affected rolling windows are recalculated. Historical reprocessing is invoked only when configuration, calibration, or analysis logic changes.

The principal SoftwareX contribution is the operational architecture connecting heterogeneous geophysical data sources to a reproducible, fault-tolerant, and scientifically constrained dashboard. The software formalizes the complete chain from remote data source or field instrument to QIT decision-support product, including acquisition, buffered transmission, scheduling, validation, provenance, robust statistics, signal processing, environmental screening, multi-domain integration, visualization, and recovery from missing or delayed data. Although

currently deployed for the QIT earthquake dashboard project, the architecture is sufficiently generic for monitoring thunderstorms, lightning, tropical cyclones, atmospheric gravity waves, traveling ionospheric disturbances, and magnetospheric particle-precipitation events. Future development will extend containerized deployment, process-health telemetry, checksum-based integrity control, event-driven scheduling, uncertainty propagation, automatic delayed-data reprocessing, expanded GNSS and satellite ingestion, and probabilistic machine-learning ranking applied only after deterministic quality control and physically interpretable feature extraction.

References

[1] S. Sasmal, S. Chowdhury, S. Kundu, D. Z. Politis, S. M. Potirakis, G. Balasis, et al., "Pre-seismic irregularities during the 2020 Samos (Greece) earthquake (M = 6.9) as investigated from multi-parameter approach by ground and space-based techniques," Atmosphere, vol. 12, Art. no. 1059, 2021.

[2] M. Hayakawa, A. Schekotov, J. Izutsu, S. Yang, M. Solovieva, and Y. Hobara, "Multi-parameter observations of seismogenic phenomena related to the Tokyo earthquake (M = 5.9) on 7 October 2021," Geosciences, vol. 12, Art. no. 265, 2022.

[3] M. Hayakawa, M. Solovieva, G. Kopylova, S. Hirooka, S. Sasmal, K. Nanda, et al., "Multi-parameter and multi-layer observations of electromagnetic precursors to a huge Hokkaido earthquake (M = 6.7) on 5 September 2018, and lithosphere–atmosphere–ionosphere coupling channel," Atmosphere, vol. 16, Art. no. 1372, 2025.

[4] S. Sasmal, K. Nanda, M. Hayakawa, M. Solovieva, G. Kopylova, and S. M. Potirakis, "Towards understanding earthquake preparatory dynamics: A multi-parametric investigation of the 2025 Kamchatka Mw 8.8 event," Atmosphere, vol. 16, Art. no. 1328, 2025.

Capacitive Coupling Model between the Earth's Crust and the Ionosphere: Electrification in Pre-seismic Charged Fractured Layer with Supercritical Water

Akira Mizuno, Minghui Kao, and Ken Umeno

Department of Applied Mathematics and Physics, Graduate School of Informatics, Kyoto University, Kyoto, Japan
Corresponding author: mizuno.akira.5c@kyoto-u.ac.jp

Abstract — This paper proposes a unified capacitive coupling model between the Earth's crust and the ionosphere to explain ionospheric anomalies observed prior to major earthquakes. According to the rock dilatancy model, tectonic stress builds up in weak parts of the fault zone, creating a network of micro-fractures and fissures. High-temperature and high-pressure water containing dissolved ions penetrates these micro-gaps and becomes supercritical, transitioning into an electrical insulator. Due to abrupt pressure changes during penetration, dissolved ions precipitate as ultrafine charged particles. Driven by flow electrification, triboelectric charging, and thermionic emission, these water and particles acquire dense positive charge, generating voltage across the thin fractured layer (thickness d < 10 micrometers). This pre-seismic charged layer behaves as a massive capacitor, altering the local electric field up to the ionospheric boundary. Quantitative calculations demonstrate that a potential rise of approximately 300 V on the ground surface can reduce the global-circuit current and induce a rapid descent of the lower ionosphere (approximately 14.4 km), which perfectly reconciles with continuous atmospheric current measurements at Kwasan Observatory and oblique ionosonde data prior to the 2011 Tohoku-Oki and 2024 Noto Peninsula earthquakes. Preliminary high-pressure experimental results of clay-water mixtures in near-supercritical conditions validate the physical plausibility of the positive charge generation process.

Keywords: Supercritical water, Dilatancy model, Capacitive coupling, Ionospheric anomalies, Atmospheric current reduction.

1. Introduction

A wide range of anomalous seismo-electromagnetic phenomena in the upper atmosphere, such as changes in Total Electron Content (TEC), the lowering of the bottomside ionosphere, and the deceleration of Medium-Scale Traveling Ionospheric Disturbances (MSTIDs), have been widely reported as precursory indicators before large earthquakes (M > 6.0) [1, 2]. To explain these lithosphere-atmosphere-ionosphere coupling (LAIC) precursors quantitatively, we propose a novel physical mechanism where a pre-seismic highly charged fractured layer in the crust couples electrostatically with the lower ionosphere [3]. Our model integrates rock mechanics, high-pressure physical chemistry of supercritical fluids, and electrostatic parallel-plate circuit theory.

While traditional coupling mechanisms suggest chemical pathways or acoustic gravity waves, our capacitive coupling framework establishes that pre-seismic micro-cracking of weak fault interfaces generates massive charge separation. The physical feasibility is validated through the phase transition of underground water and geological boring evidence showing smectite-rich slippery fault gouges that squeezed out moisture upon sliding [4]. Here we detail the charging dynamics under the dilatancy framework and the resulting electrostatic responses of the global circuit and ionospheric boundary.

2. Dilatancy Framework and Electrification of Supercritical Water

Prior to a major tectonic rupture, rocks at the fault zone undergo micro-cracking and expansion—known as the dilatancy model [5]. Deep in the seismogenic crust (depths > 10–15 km), geothermal gradients establish high ambient temperatures. When sliding begins under tectonic stress, frictional heat instantly

elevates the temperature in the localized sheared zones to exceed 374 °C, under pressures of several hundred atmospheres. Under these conditions, water squeezed from minerals like smectite transitions into a supercritical state.

Supercritical water exhibits a physical phase change: its relative permittivity (dielectric constant) drops precipitously from 80 down to 2–5 [6]. Under this low-dielectric condition, supercritical water behaves as an electrical insulator. Furthermore, the ion product of water reaches a peak of approximately 10^-10.5 mol^2 kg^-2 at around 250 °C, facilitating the rapid dissolution of minerals such as Al and Si from smectite. However, as the fluid expands and transitions into the supercritical state, the ion product drops sharply, causing the dissolved metal ions to precipitate as ultrafine nanoparticles [7].

Inside the microscopic, high-temperature fault cracks, three concurrent processes positively charge the precipitated nanoparticles: (a) Flow/fluid electrification during explosive penetration, (b) Triboelectric charging (friction) between nanoparticles and crack walls, and (c) Thermionic electron emission from metal-oxide nanoparticles (e.g., SiO_2, Al_2O_3) at temperatures exceeding 400 °C. Because the conductivity of supercritical water is extremely small, and high-mobility electrons quickly dissipate into the surrounding quasi-conductive crust, a high-density positive ionic space charge is structurally stabilized inside the insulating fractured layer.

3. Capacitive Coupling and Electrical Breakdown Limits

Before total macroscopic failure occurs, the thickness of the pre-seismic micro-fractured layer is extremely thin, generally less than 10 micrometers ($d < 10$ μm). The capacitance per unit area of this thin crustal capacitor ($C_0 = \varepsilon_s \varepsilon_0 / d$) is approximately 4.4 x 10^-6 F/m^2 (assuming $\varepsilon_s = 5$). This value is roughly eleven orders of magnitude larger than the air-gap capacitance between the ground surface and the ionosphere (C_a = 8.8 x 10^-17 F/m^2 for H = 1 x 10^5 m) [3].

As charge accumulates, the potential difference across the micro-gap increases. When the voltage exceeds the dielectric breakdown threshold of the microscopic gap, electrical discharges occur. Following field emission mechanisms for micro-gaps (Paschen's law limit), the maximum sustainable potential difference across the 10 μm fractured layer is restricted to approximately 300 V (electric field strength of 3 x 10^7 V/m) [8]. This 300 V potential rise of the ground surface directly reduces the potential difference in the global electric circuit, decreasing the downward atmospheric current (normally 2 pA/m^2) [9].

Concurrently, the local electric field ($E_z \fallingdotseq 300$ V/H) alters the boundary of the upper atmosphere. High-mobility diffusive electrons are drawn down from the lower ionosphere, attaching to neutral gas molecules to form a negative space charge that screens the crustal electric field. The upper plasma layer descends to maintain charge neutrality, causing a physical lowering of the ionosphere. Our transient response model predicts an initial descent velocity of 66 m/s and an asymptotic saturation descent distance of 16.5 km, with a time constant of 250 seconds, demonstrating quantitative agreement with oblique ionosonde observations [10].

4. Experimental Validation and Field Observations

To evaluate the physical feasibility of the positive charge generation process, a preliminary experiment was conducted using a stainless steel tube to heat a clay-water mixture (ceramics clay containing 70% SiO_2, 20% Al_2O_3) up to 400 °C under pressurized conditions. Upon breaking of the aluminum foil seal, the clay-water mixture was ejected explosively into a Faraday cage connected to a Keithley electrometer. The measurements recorded a stable positive charge of approximately 22 x 10^-9 C/g [3], confirming that clay-water mixtures become positively charged near supercritical conditions.

Physical Parameter	Assumed Value	Physical Significance / Outcome
Fractured Layer Thickness (d)	10 micrometers (μm)	C_0 = 4.4 x 10^-6 F/m^2 (Extremely large)
Relative Permittivity (ε_s)	2 to 5	Supercritical insulator, stabilizes charges
Max Breakdown Voltage (V_max)	300 V	Constrained by micro-gap field emission
Ionospheric Descent (Noto 2024)	14.4 km (Observed)	Theory predicts 16.5 km limit (Within 360s)

Table 1. Unified physical parameters of the capacitive coupling model between crust and ionosphere.

5. Conclusions

We have proposed a comprehensive capacitive coupling model based on the pre-seismic rock dilatancy process. Frictional heating under tectonic pressure transforms fault water into an insulating supercritical state, leading to positive charge accumulation on nanoparticles via flow, triboelectric, and thermionic emission. The breakdown limit of 300 V restricts the ground potential rise, which quantitatively matches the observed reductions in atmospheric current and oblique ionosonde descent of 14.4 km prior to the 2024 Noto Peninsula earthquake. Furthermore, the model suggests a reversible mechanism where solar flare-induced ionospheric space charges can exert a multi-atmospheric electrostatic trigger back onto the critical crust. This interdisciplinary framework provides a robust physical foundation for seismo-electromagnetics and advances predictive forecasting.

References

[1] M. Hayakawa et al., "Monitoring of ULF geomagnetic variations associated with earthquakes," Sensors, vol. 7, pp. 1108–1122, 2007.

[2] K. Heki, "Ionospheric disturbances related to earthquakes," in Ionosphere Dynamics and Applications, pp. 511–526, 2021.

[3] A. Mizuno, M. Kao, and K. Umeno, "A capacitive coupling model between the ionosphere and a fault layer in the crust with supercritical water," Int. J. Plasma Environ. Sci. Technol., vol. 18, p. e01003, 2024.

[4] G. Kimura et al., "Deformation process and mechanism of the frontal megathrust at the Nankai subduction zone," Geochem. Geophys. Geosystems, vol. 23, e2021GC009855, 2022.

[5] F. T. Freund, "Pre-earthquake signals: Underlying physical processes," J. Asian Earth Sci., vol. 41, pp. 383–400, 2011.

[6] T. Ono and H. Inomata, "Supercritical water - properties and applications," OYO BUTURI, vol. 80, no. 10, pp. 875–880, 2011.

[7] A. Yoko et al., "Continuous flow synthesis of nanoparticles using supercritical water," KONA Powder Particle J., vol. 37, pp. 28–41, 2020.

[8] Y. Yamano, "Characteristics of breakdown between electrodes with micro-gap in atmosphere," J. Inst. Electrostat. Jpn., vol. 36, pp. 146–151, 2012.

[9] A. Mizuno and K. Takashima, "Continuous measurement of current in air and possible relation with intense earthquake," J. Electrostat., vol. 71, pp. 529–532, 2013.

[10] A. Mizuno, M. Kao, and K. Umeno, "Mechanism of ionospheric descent prior to intense earthquakes by electrostatic coupling with an electrically charged fractured layer," Int. J. Plasma Environ. Sci. Technol., vol. 19, p. e01010, 2025.

Pre-Earthquake Ionospheric Anomalies Associated with the 2025 Kamchatka M8.8 Earthquake: Toward Data-Driven Short-Term Earthquake Forecasting

Katsumi Hattori[1,2,3], Jann-Yenq Liu[4], Peng Han[5], Dimitar Ouzounov[6], Qinghua Huang[7], Chinatsu Sasanuma[8], Chie Yoshino[1], Wenchao Li[8], Rui Song[1], Takumi Ono[8], Jumpei Najima[8], Yoichi Noda[8], Keigo Saeki[8], Slava Pillipenko[9]

1. Center for Environmental Remote Sensing, Chiba University, Japan
2. Graduate School of Science, Chiba University, Japan
3. Research Institute of Disaster Medicine, Chiba University, Japan
4. National Central University, Taiwan,
5. Southern University of Science and Technology, China,
6. Hellenic Mediterranean University, Greece,
7. Peking University, China,
8. Graduate School of Science and Engineering, Chiba University, Japan
9. Schmidt Institute of Physics of the Earth, Russian Academy of Sciences, Moscow, Russia

Corresponding author: khattori@faculty.chiba-u.jp

Despite remarkable advances in seismology and geophysics, reliable short-term earthquake forecasting remains one of the greatest challenges in Earth science. Many earthquakes, such as the 2004 Sumatra earthquake, the 2008 Sichuan earthquake, and the 2011 Tohoku earthquake, have caused devastating damage to human society. While short-term earthquake forecasting is expected to mitigate damage, it has not yet been realized. In recent years, statistically significant ULF magnetic field variations, ionospheric anomalies, and satellite thermal infrared anomalies have been reported preceding earthquakes, raising hopes for the realization of short-term earthquake forecasting. Our group focuses on multi-parameter electromagnetic and geophysical observations and is developing data-driven methods for short-term earthquake forecasting based on statistically validated precursory phenomena.

This study investigated the pre-earthquake ionospheric anomalies (PEIAs) during the preparation phase of the M8.8 Kamchatka earthquake in Russia that occurred on July 29, 2025. Multiple ionospheric parameters derived from both ground-based and space-borne observations were used, including total electron content from the Global Navigation Satellite System, the F2 layer critical frequency from ionosondes, electron density, and three geomagnetic components recorded by the Swarm satellite. After excluding the influences of geomagnetic and solar activities, abnormal disturbances in the near-field region within 1000 km of the epicenter and those in the far-field region within 3000 km on July 20 and 21 were identified as PEIAs associated with a sequence of moderate foreshocks and the mainshock. Furthermore, to explore the possible lithosphere-atmosphere-ionosphere coupling mechanisms, we examined the Ultra-Low-Frequency (ULF) geomagnetic field in the lithosphere, as well as the chemical potential, outgoing long-wave radiation, and surface skin temperature in the atmosphere. The presence of anomalous geomagnetic ULF variations in the near-field region, together with their absence in the far-field region, suggests a possible contribution of electromagnetic emissions to the near-field PEIAs. In contrast, the preceding anomaly in atmospheric chemical potential, along with the double-crest structure in electron density, may indicate that the electric field variation is a possible mechanism triggering the far-field PEIAs.

Regarding earthquake forecasting, we use ground and satellite data to study geomagnetic variations, ionospheric variations, Earth's surface temperature variations, GNSS crustal movements, and variations in subsurface radon concentrations. We aim to improve prediction accuracy by conducting detailed investigations into phenomena that show significant correlations with seismic activity and statistically verifiable precursory phenomena. Similar to evidence-based epidemiology, the emphasis

is shifting from individual case studies to statistically validated risk indicators and their integration into forecasting models. The presentation reviews the statistical significance and ROC-based forecasting skill of diverse precursory phenomena within the SensorWEB framework. It then discusses general approaches for evaluating and integrating statistically validated precursor information toward short-term earthquake forecasting. Finally, the current status, remaining challenges, and future prospects of data-driven multi-parameter earthquake forecasting are discussed.

Towards the Localization of Earthquake Preparation through Combined Seismo-Electromagnetic and Seismicity Analysis

Stelios M. Potirakis[1], Efstathios Kyriakis-Bitzaros[1], Sudipta Sasmal[2,1], Angelos Charitopoulos[1], Dionysios Dimakos[3,1], Yiannis Kokkaliaris[1]
[1] Department of Electrical and Electronics Engineering, University of West Attica, Egaleo-Athens, Greece
[2]Institute of Astronomy Space and Earth Science, Kolkata, India
[3]Hellenic Telecommunications and Post Commission (EETT), Maroussi-Athens, Greece
Corresponding author: spoti@uniwa.gr

1. Introduction

Earthquake (EQ) preparation is a complex, spatially distributed process that may manifest itself through changes in several observables, including seismicity, electromagnetic emissions and the lower ionosphere. A fundamental difficulty in the investigation of possible earthquake-preparation signatures is not only their detection but also their spatial localization. A seismic catalog covering a broad region may contain earthquakes associated with different tectonic structures, while ground-based seismo-electromagnetic observations are intrinsically constrained by the locations of the receivers (and transmitters in the case of VLF/LF subionospheric propagation anomalies).

Our seismo-electromagnetics research in Greece is developing towards the use of complementary precursors. On one hand, the hELlenic Seismo-ElectroMagnetics Network (ELSEM-Net) provides continuous monitoring of fracture-induced electromagnetic emissions (FEME/FEMR) in Greece [1], while a network of VLF/LF receivers, installed in Greece, Cyprus, and Israel, provides complementary monitoring of the lower ionosphere [2]. On the other hand, natural-time (NT) analysis has been applied not only to electromagnetic time series but also to seismicity, including the spatially resolved analysis of seismic activity within seismotectonic and seismic-hazard zones [3]. Most recently, the analysis of small-area seismic micro-catalogues, suggested by Matcharashvili and Chelidze [4], has provided a further possibility for identifying spatial differences in the evolution of seismicity.

The purpose of this contribution is to bring these developments together and to propose a multiscale approach for the localization of an evolving earthquake-preparation region.

2. ELSEM-Net and VLF/LF Subionospheric Monitoring

The hELlenic Seismo-ElectroMagnetics Network (ELSEM-Net) [1] is a distributed network of telemetric stations developed for the continuous monitoring of FEME/FEMR in Greece. The network was progressively developed during the 1990s and currently comprises 11 stations distributed at different locations throughout Greece. Its instrumentation, designed by our team, monitors selected kHz magnetic-field and MHz electric-field components. The physical motivation for ELSEM-Net derives from laboratory and field observations of electromagnetic emissions associated with the progressive fracturing of heterogeneous materials. Accordingly, the spatial distribution of ELSEM-Net stations provides an opportunity to investigate whether electromagnetic activity evolves coherently with the preparation of strong earthquakes.

The usefulness of this approach has been investigated in several EQ case studies. In particular, for the January–February 2014 Cephalonia EQ sequence, MHz electromagnetic emissions recorded by stations on Cephalonia and the neighboring island of Zakynthos exhibited critical characteristics before the earthquakes [3]. These characteristics were investigated using both the method of critical fluctuations and natural-time analysis. Importantly, the seismicity itself also exhibited critical characteristics when analyzed in natural time.

A complementary observation focusing on the lithosphere–atmosphere–ionosphere system is provided by VLF/LF subionospheric propagation measurements. Our VLF/LF infrastructure currently includes four receivers: two located in Athens, Greece (UWA &WAU) at University of West Attica, one in Nicosia, Cyprus (FRC) at Frederick University and one in Ashdod, Israel (SCE) at Shamoon College of Engineering. These receivers monitor signals transmitted by both relatively

close and distant VLF/LF transmitters. For example, previous studies have simultaneously analyzed the 29.7-kHz signal transmitted from Negev, Israel, at the three Attica receivers [2].

Changes in VLF/LF propagation characteristics can reflect perturbations of the lower ionosphere. The simultaneous availability of several monitored paths provides an important opportunity to distinguish global from local-sourced anomalies.

Thus, ELSEM-Net and the VLF/LF network provide two complementary seismo-electromagnetic observational windows: the former monitors direct electromagnetic emissions potentially associated with crustal fracturing, whereas the latter monitors possible perturbations of the lower ionosphere.

3. Natural-Time Analysis and Seismic-Zoning Polygons

Natural-time analysis provides a framework for studying the evolution of complex systems approaching criticality. For a sequence of N earthquakes, the natural time of the k-th event is defined as:

$$\chi_k = \frac{k}{N}, \tag{1}$$

and each event is assigned a normalized weight p_k, usually related to its seismic energy. A principal quantity is the variance of natural time,

$$\kappa_1 = \langle \chi^2 \rangle - \langle \chi \rangle^2, \tag{2}$$

where:

$$\langle f(\chi) \rangle = \sum_{k=1}^{N} p_k \, f(\chi_k). \tag{3}$$

The temporal evolution of such quantities can be used to investigate changes in the dynamical state.

This issue was explicitly addressed in our study of the 2014 Cephalonia EQ sequence. The seismicity was considered in relation to the existing seismotectonic and seismic-hazard zoning of the Ionian Islands, and natural-time analysis was performed with attention to the different spatial zones. The results indicated that the critical process associated with the EQ preparation appeared to be focused on the area corresponding to the western Cephalonia zone [3].

This observation suggests an important methodological principle: rather than applying natural-time analysis to an arbitrarily selected region around an EQ epicenter (circular or of other shape), which by the way is mainly an “a posteriori” approach, one can use the seismic-hazard zoning of a wider region and analyze the seismicity within gradually smaller unions of seismic-zoning polygons, until identifying the polygon from which criticality is sourced.

Such an approach provides a first level of spatial EQ localization, solely based on seismicity. The question becomes not simply whether the regional seismicity exhibits critical characteristics, but rather: “Which seismotectonic region is exhibiting the evolving critical behavior?” This distinction is particularly important if the objective is to investigate EQ preparation rather than merely to characterize the seismicity of a large geographical area.

4. Micro-Catalogues: An Alternative Solution or a Complementary one for Finer Spatial Resolution?

A natural extension of the polygon-based seismic-hazard zoning approach is to investigate the seismicity at a possibly finer spatial scale. A most recent study by Matcharashvili and Chelidze introduced the analysis of small-area seismic micro-catalogues along and near the San Andreas fault [4]. The basic hypothesis is that seismicity in the vicinity of an earthquake-preparation area should evolve differently from the seismicity occurring in surrounding areas. For example, not all parts of an entire large fault can be simultaneously and equally involved in the preparation of a strong earthquake. Therefore, by comparing dynamical characteristics of different smaller fault zone areas (micro-catalogues) one can recognize those, in which seismic process becomes significantly

different from the other ones. This may serve as an indication that in this micro-catalogue and/or adjacent area the strong EQ preparation approaches final stage [4].

In that study, small spatial regions were treated as individual seismic micro-catalogues, and characteristics related to cumulative time, spatial distance and released seismic energy were calculated. The seismic processes in neighboring micro-catalogues were subsequently compared using multivariate statistical measures, including Mahalanobis distance. The analysis reported significant changes in the characteristics of small-area seismic processes before several strong earthquakes.

The micro-catalogue approach is a data-driven approach of similar reasoning with the analysis using a priori known seismic-zoning. The latter incorporates geological and seismotectonic information into the spatial definition of the analysis, whereas the former allows the seismicity itself to identify a smaller region exhibiting anomalous dynamical behavior. Micro-cataloguing can be alternative to seismic-zoning, if the second is not available, or complementary to it if applied within a seismic zone to provide a finer spatial resolution, forming a hierarchical spatial analysis scheme.

In the latter case, the hierarchical procedure is important because the two spatial scales answer different questions. Natural-time analysis within seismic-zoning polygons asks where, at the regional/seismotectonic scale, the seismic system is approaching a critical state. Micro-catalogue analysis then asks where, within that region, the seismic process is becoming different from its surroundings.

However, one should take into account that the spatial resolution of the micro-catalogues cannot be selected independently of the detection and location capabilities of the seismic network deployed along the region of interest. In particular, the minimum magnitude of completeness, its spatial variability, the number of events available within each micro-catalogue, and the uncertainties of hypocentral locations must be considered when defining the micro-catalogue dimensions. Consequently, micro-cataloguing potential to provide a spatial scale finer than the seismotectonic zoning is dependent on the spatial resolution supported by the seismic network.

5. Towards a Multidisciplinary Localization of Earthquake Preparation

The localization resulted from seismicity can be combined with seismo-electromagnetic observations. If an evolving seismicity criticality is identified within a particular seismic-zoning polygon, and possibly further localized by the micro-catalogues, ELSEM-Net observations can be examined for electromagnetic activity consistent with the same region and time interval, or vice-versa. Similarly, VLF/LF observations can be examined in relation to the transmitter–receiver propagation paths crossing or approaching the candidate preparation region. Of course, any other available localization information coming from any seismo-electromagnetic (e.g., GNSS, ULF magnetic field) or atmospheric/chemical precursors can also be aggregated towards EQ localization.

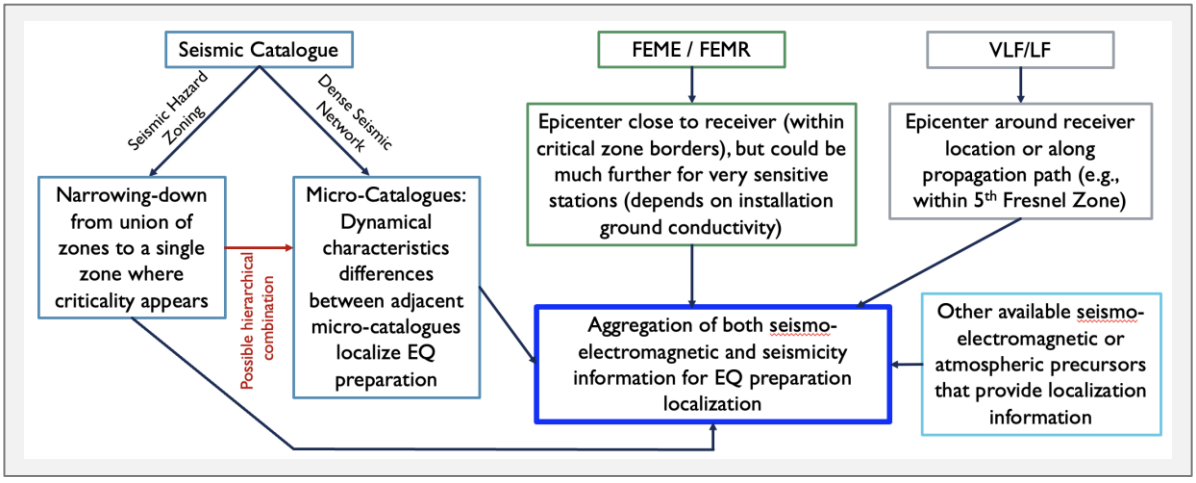


Figure 1. Multidisciplinary localization of imminent earthquake.

The important point is that the electromagnetic observations need not independently provide a precise EQ location. Rather, they can provide independent complementary evidence for a seismicity-based localization. Conversely, a seismicity-based localization can provide a physically motivated spatial constraint for interpreting electromagnetic or ionospheric anomalies.

The combination of the above approaches suggests a framework in which EQ preparation is investigated as a spatiotemporal evolution observed through multiple, partially independent channels.

6. Conclusions

ELSEM-Net and the VLF/LF receiver network provide complementary observational infrastructures for investigating possible electromagnetic and ionospheric manifestations associated with EQ preparation. The Cephalonia study demonstrated that natural-time analysis of seismicity, when performed with consideration of the underlying seismotectonic and hazard zoning, can provide information about the spatial concentration of a critical seismic process [3].

The recently proposed micro-catalogue methodology provides a natural next step by examining the seismic process at a much finer spatial scale and identifying areas whose temporal, spatial and energy characteristics differ from those of neighboring areas [4].

We propose combining these approaches into a multiscale localization framework: natural-time analysis within seismic-zoning polygons provides the first spatial constraint, micro-catalogue analysis possibly provides finer localization, and ELSEM-Net and VLF/LF observations provide independent complementary information from the electromagnetic and ionospheric domains.

The central objective is therefore not to infer an EQ from a single precursor, but to investigate whether consistent spatiotemporal changes across seismic, electromagnetic and ionospheric observations can identify and localize an evolving earthquake-preparation process. Systematic retrospective testing followed by prospective application will be required to establish the statistical significance, robustness and generality of this approach.

References

[1] P. Malkotsis, et al. “ELSEM-Net, a network of ground-based telemetric stations for the monitoring of fracture-induced electromagnetic emissions in Greece: Instrumentation, management and analysis of recent observations associated with strong earthquakes,” Annals Geoph., 66, 2023. https://doi.org/10.4401/ag-8985.

[2] D.Z. Politis, et al. “Possible pre-seismic indications prior to strong earthquakes that occurred in southeastern Mediterranean as observed simultaneously by three VLF/LF stations installed in Athens (Greece). Atmosphere, 14, 673, 2023. https://doi.org/10.3390/atmos14040673.

[3] S.M. Potirakis, et al. “Recent seismic activity at Cephalonia (Greece): a study through candidate electromagnetic precursors in terms of non-linear dynamics,” Nonlin. Proc. Geoph., 23, 223–240, 2016. https://doi.org/10.5194/npg-23-223-2016.

[4] T. Matcharashvili, T. Chelidze. “Changes in seismic processes in small areas along San Andreas fault prior to M > 7.0 earthquakes, 1980–2025,” Acta Geophysica, 74, 2026. https://doi.org/10.1007/s11600-026-01863-y.

Toward Continuous Earthquake Activity Forecasting Using Ionospheric Observations and End-to-End Deep Learning

Shinji Hirooka[1,2], Makio Tatsuno[1], and Masashi Hayakawa[2,3]
[1]HiSR Inc., Chiba, Japan
[2]QuakeInsight Tokyo, 1-1-1 Kojimacho, Chofu, Tokyo, Japan
[3]Advanced Wireless & Communications Research Center (AWCC), The University of Electro-Communications (UEC), 1-5-1 Chofugaoka, Chofu, Tokyo, Japan
Corresponding author: hirooka@hrl.jp

1. Introduction

Ionospheric disturbances preceding earthquakes have been investigated using total electron content (TEC), ionosonde parameters, and subionospheric radio propagation. Although numerous case studies have reported candidate anomalies, an important methodological gap remains between detecting anomalies around selected earthquakes and evaluating a continuously issued probabilistic earthquake forecast. A forecasting system must be assessed on all forecast issue dates, including non-earthquake periods, while preserving the event prevalence and preventing future information from entering training, preprocessing, model selection, calibration, or threshold setting. Subionospheric VLF/LF observations provide an important complementary line of evidence for seismo-ionospheric coupling. Hayakawa and colleagues reported VLF propagation anomalies associated with the 1995 Hyogo-ken Nanbu earthquake and subsequently conducted a seven-year statistical analysis of multiple propagation paths around Japan, finding a significant association between >2σ lower-ionospheric perturbations and shallow M > 6 earthquakes [4,5]. They also reported possible VLF/LF ionospheric perturbations preceding the 11 March 2011 Tohoku earthquake [6]. These studies motivate the broader use of ionospheric observations while also emphasizing the need to distinguish precursor detection from continuously evaluated probabilistic forecasting. We developed an End-to-End deep-learning module that learns predictive representations directly from continuous ionospheric and space-weather observations without manually assigned TEC precursor labels or manually selected earthquake-related periods. The module is jointly optimized against future cell- and forecast-horizon-specific earthquake labels and forms the observation-driven component of a two-stage probabilistic forecasting system. Background seismicity information is incorporated separately at the subsequent probability-integration stage. The system produces spatial earthquake-activity probabilities for Japan and the surrounding region for 7-, 15-, and 30-day forecast horizons. Its evaluation was designed as a leakage-controlled rolling-origin hindcast covering 12 consecutive years (2014–2025). The aim was not to claim deterministic earthquake prediction, but to test whether incorporating ionospheric observations provides incremental probabilistic forecasting information beyond strong seismicity-based reference models.

2. Data and Forecasting Task

The study region (20–50°N, 120–155°E) was divided into 80 spatial cells. For each daily forecast issue, the target was whether at least one earthquake of magnitude $M \geq 5$ and depth ≤ 50 km would occur in each cell during the following 7, 15, or 30 days. The continuous observational inputs comprised Global Ionospheric Map (GIM) vertical TEC, NmF2 derived from four Japanese ionosonde stations, and geomagnetic/solar indices. Historical earthquake activity was used as background forecast information. The ionospheric and space-weather observations were transformed by a trainable spatiotemporal representation module, and the resulting forecast information was combined with background information to obtain calibrated cellwise probabilities. Detailed implementation and fusion procedures are reserved for a separate full methodological report. For every evaluation year, only earlier observations and labels were available for model development. The two years immediately preceding each evaluation year were used for validation, while earlier years formed an expanding training set. A 30-day embargo, equal to the maximum forecast horizon, was imposed at temporal boundaries. Normalization, missing-value handling, baseline rates, model

selection, and probability calibration were estimated only within the corresponding training or validation periods.

3. Evaluation Design

The principal endpoint was Bernoulli log loss averaged with equal weight over all $M \geq 5$ forecast issue dates, 80 cells, and the three forecast horizons. Brier score and precision–recall area under the curve (PR-AUC) were also examined. Spatial performance was assessed under fixed alarm-area constraints. Comparators included an ionosphere-excluded system, a seismicity-only model, persistence forecasting, and a maximum-likelihood space-time epidemic-type aftershock sequence (ETAS) model. The evaluation comprised 3,993 daily forecast issues and 958,320 cell-horizon samples; the mean positive-label prevalence was 3.9873%. The evaluation-period catalog contained 1,371 non-duplicate $M \geq 5$ earthquakes. Uncertainty in paired log-loss differences was estimated using 4,000 hierarchical bootstrap replicates, with evaluation year as the upper-level cluster and 60-day moving blocks within years. This design was chosen to retain important temporal dependence rather than treating the large number of cell-horizon samples as independent observations. A matched input-ablation experiment was additionally conducted using the same model capacity, temporal splits, hyperparameter rules, and five random seeds; only the ionospheric input streams were disabled in the control arm.

The evaluation hierarchy was chosen to separate probabilistic forecasting performance from exploratory localization. The integrated $M \geq 5$ log loss across the three horizons was treated as the principal system summary, whereas horizon-specific scores and recall under a fixed alarm area were secondary measures. PR-AUC and related ranking measures were interpreted as complementary because they emphasize discrimination rather than probability calibration. This separation is relevant for rare-event forecasting: a model can rank locations effectively while assigning poorly calibrated probabilities, or conversely provide useful probability estimates without sharply localizing every event.

The three forecast horizons are not statistically independent: an earthquake occurring within seven days is also included in the corresponding 15- and 30-day targets. Accordingly, the integrated score is interpreted as a summary of three correlated operational horizons rather than as three independent experiments. The hierarchical bootstrap was used to reflect this dependence together with year-to-year variability and within-year temporal correlation. These choices were intended to avoid overstating precision simply because the gridded forecasting framework generates a very large number of cell-horizon observations.

4. Results

Across the three $M \geq 5$ forecast horizons, the full-modality system achieved a log loss of 0.115609, compared with 0.117785 for the ionosphere-excluded system and 0.117427 for the seismicity-only model. Defining the paired improvement as $\Delta L = L(\text{comparator}) - L(\text{full})$, the ionosphere-excluded comparison yielded $\Delta L = 0.002176$ (95% confidence interval, 0.001634–0.002862). Thus, under the leakage-controlled rolling-origin evaluation, inclusion of ionospheric information was associated with a statistically supported improvement in system-level probabilistic forecast performance.

5. Spatial and Robustness Analyses

At a fixed top-10% alarm area, spatial recall was 0.5387 for the full system, 0.5373 for the ionosphere-excluded system, and 0.5364 for ETAS. A declustered-mainshock sensitivity analysis yielded log loss values of 0.112704, 0.114900, and 0.113241 for the full, ionosphere-excluded, and ETAS forecasts, respectively. These results provide a basis for further improvement of localization using higher-resolution ionospheric observations.

6. Discussion

The main methodological contribution of this work is the transition from classification of selected precursor-event samples to an End-to-End observation-driven module embedded within a continuously issued, leakage-controlled probabilistic forecasting experiment. In this formulation, intermediate ionospheric precursor labels are not required: the observation representation is optimized directly against the future earthquake-activity forecasting objective. This is important because high classification accuracy in a selected case-control data set does not necessarily imply useful performance when forecasts are issued continuously across earthquake and non-earthquake periods.

The system-level comparison provides quantitative evidence that a forecasting configuration incorporating ionospheric observations can add predictive value beyond a corresponding ionosphere-excluded configuration. Importantly, this result was obtained across all forecast issue dates rather than from selected pre-earthquake intervals. The matched raw-input analysis showed point estimates in the same favorable direction for log loss and PR-AUC, providing additional motivation to investigate how ionospheric information is represented and preserved when combined with strong background seismicity predictors. The independent contribution of individual modalities remains a target for prospective confirmation.

The End-to-End formulation also provides a practical framework for future falsification. Once the input definition, forecasting target, architecture, and evaluation rules are frozen, the same system can be carried forward prospectively without redefining precursor thresholds after observing new earthquakes. Such prospective evaluation is particularly important for a field in which ionospheric variability is strongly influenced by solar and geomagnetic forcing and in which earthquake occurrence is highly clustered in space and time.

For radio-observation research, a broader implication is that candidate seismo-ionospheric signals can be evaluated not only as isolated anomalies but also as inputs to a formally scored forecasting experiment. This creates a common interface between observational studies and forecast verification: additional ionospheric measurements can be introduced as input streams and tested according to whether they improve prespecified probabilistic scores under the same chronological information boundary. Such a framework may help distinguish signals that are visually compelling in individual events from those that contribute reproducibly across many forecast issue dates.

Future extensions should also distinguish improvements in occurrence probability from improvements in spatial localization. The present 80-cell grid was designed for stable long-period evaluation rather than precise epicentral prediction. Higher-resolution regional TEC observations could provide additional spatial information, while the End-to-End objective could be extended to learn occurrence and conditional location representations separately. Importantly, such extensions should be specified before evaluating new earthquakes so that gains in localization can be interpreted prospectively rather than as retrospective optimization.

The present results also suggest a useful distinction between representation learning and forecast integration. The End-to-End module is intended to extract time-dependent information from the observational streams, whereas the subsequent integration stage supplies strong background information on where and when earthquakes are already more likely to occur. The marked reduction of the matched-ablation difference after this integration indicates that preserving weak observation-derived information in the presence of strong seismicity predictors is itself an important model-design problem. Future work should therefore examine integration strategies that retain complementary temporal information without allowing static spatial rate differences or recent seismicity to dominate the learned observation signal.

Another priority is prospective reproducibility. The present hindcast uses a fixed chronological evaluation framework, but final GIM and space-weather research products were reconstructed retrospectively and do not reproduce every latency that would have occurred in real-time operation. A prospective experiment should therefore record the exact data product available at each issue time, the acquisition timestamp, missing-data state, model version, and issued probability field. Such a

record would permit evaluation not only of statistical discrimination but also of calibration stability, false-alarm burden, lead-time distribution, and robustness to temporary observation outages. These operational quantities are essential if ionospheric observations are ultimately to contribute to disaster-resilience decision support.

Finally, the framework is deliberately modular with respect to the observing system. The current experiment uses GIM VTEC and four ionosonde stations because they provide long, relatively consistent records suitable for a multi-year hindcast. Regional GNSS networks and additional radio observations could provide finer spatial or altitude-dependent information, but their value should be judged by the same criterion: incremental improvement under a fixed forecasting protocol. This offers a pathway by which diverse radio-observation techniques can be compared within a common probabilistic framework rather than solely through visually selected pre-earthquake anomalies.

7. Conclusion

We evaluated a two-stage earthquake-activity forecasting framework containing an End-to-End deep-learning module for continuous ionospheric and space-weather observations over 12 consecutive years using rolling-origin information boundaries. The End-to-End formulation removes the need for manually assigned ionospheric precursor labels and links the learned observation representation directly to the future earthquake-activity objective. For $M \geq 5$ earthquakes, the full system achieved lower log loss than the ionosphere-excluded system, with a paired improvement of $\Delta L = 0.002176$ (95% confidence interval, 0.001634–0.002862). Matched input ablation also produced favorable point estimates for both log loss and PR-AUC when ionospheric inputs were included. These findings provide quantitative support for further prospective evaluation of ionospheric observations as a complementary information source for earthquake-activity forecasting, using prespecified model configurations, fixed information boundaries, and higher-resolution observations.

References

[1] G. C. Beroza, M. Segou, and S. M. Mousavi, “Machine learning and earthquake forecasting—next steps,” Nature Communications, vol. 12, 4761, 2021.

[2] A. A. Akyol, O. Arikan, and F. Arikan, “A machine learning based detection of earthquake precursors using ionospheric data,” Radio Science, vol. 55, e2019RS006931, 2020.

[3] T. C. Tsai et al., “Deep learning of detecting ionospheric precursors associated with M 6.0 or larger earthquakes in Taiwan,” Earth and Space Science, vol. 9, e2022EA002289, 2022.

[4] M. Hayakawa, O. A. Molchanov, T. Ondoh, and E. Kawai, “Anomalies in the sub-ionospheric VLF signals for the 1995 Hyogo-ken Nanbu earthquake,” Journal of Physics of the Earth, vol. 44, pp. 413–418, 1996.

[5] M. Hayakawa et al., “A statistical study on the correlation between lower ionospheric perturbations as seen by subionospheric VLF/LF propagation and earthquakes,” Journal of Geophysical Research: Space Physics, vol. 115, A09305, 2010.

[6] M. Hayakawa et al., “Possible precursor to the March 11, 2011, Japan earthquake: ionospheric perturbations as seen by subionospheric very low frequency/low frequency propagation,” Annals of Geophysics, vol. 55, 2012.

[7] Y. Ogata, “Statistical models for earthquake occurrences and residual analysis for point processes,” Journal of the American Statistical Association, vol. 83, pp. 9–27, 1988.

[8] S. Kon, M. Nishihashi, and K. Hattori, “Ionospheric anomalies possibly associated with $M \geq 6.0$ earthquakes in the Japan area during 1998–2010,” Journal of Asian Earth Sciences, vol. 41, pp. 410–420, 2011.

[9] J. N. Thomas, J. Huard, and F. Masci, “A statistical study of global ionospheric map total electron content changes prior to occurrences of $M \geq 6.0$ earthquakes during 2000–2014,” Journal of Geophysical Research: Space Physics, vol. 122, pp. 2151–2161, 2017.

[10] S. Hirooka, K. Hattori, M. Nishihashi, and T. Takeda, “Neural network based tomographic approach to detect earthquake-related ionospheric anomalies,” Natural Hazards and Earth System Sciences, vol. 11, pp. 2341–2353, 2011.

Advancing Disaster Risk Reduction through Ionospheric Guidance: A Multi-Hazard, Source-Resolved Framework for India

Abhriup Datta[1], Sudipta Sasmal[2,3,4], Masashi Hayakawa[3,5,6] and Yasuhide Hobara[6,7]

[1]Indian Institute of Technology Indore, Indore, India
[2]Institute of Astronomy Space and Earth Science, Kolkata, India
[3]QuakeInsight Tokyo, UEC Alliance Center, Tokyo, Japan
[4]Department of Electrical and Electronics Engineering, University of West Attica, Egaleo, Greece
[5]Hayakawa Institute of Seismo Electromagnetics, Co., Ltd., UEC Alliance Center, Tokyo, Japan
[6]Department of Information and Networking, The University of Electro-Communications, Tokyo, Japan
[7]Center for Space and Radio Engineering, The University of Electro-Communications, Tokyo, Japan
Corresponding author: meet2ss25@gmail.com

India faces a combination of high-impact geophysical and meteorological hazards, including Himalayan and Northeast Indian earthquakes, tropical cyclones over the Bay of Bengal and Arabian Sea, monsoon-related extreme rainfall, landslides, severe thunderstorms, and intense lightning activity. Independent ground-based networks and discipline-specific analysis systems generally monitor these hazards. Such horizontal monitoring is essential, but it does not fully exploit a second observational dimension: the vertical transfer of energy, momentum, electric fields, and electromagnetic disturbances from the lithosphere and lower atmosphere into the ionosphere. The proposed IONospheric Guidance for Urban & Rural Disaster Risk Reduction (IONGUARD) framework addresses this gap by treating the ionosphere as an active diagnostic layer within a multi-hazard disaster-risk-reduction system. Its objective is not deterministic prediction, but physically constrained identification, discrimination, and interpretation of hazard-related disturbances using coordinated ground- and space-based observations.

The scientific basis of IONGUARD is that different hazards can produce measurable ionospheric responses through distinct coupling pathways. Pre-seismic processes may be accompanied by crustal deformation, thermal and atmospheric anomalies, conductivity changes, electric-field perturbations, VLF/LF propagation anomalies, and changes in ionospheric plasma density. Intense convection and lightning can generate atmospheric gravity waves, broadband electromagnetic emissions, and lower-ionospheric perturbations, while tropical cyclones can excite coherent gravity-wave structures that propagate upward and appear as traveling ionospheric disturbances in GNSS-derived total electron content. The main challenge is therefore not simply to detect an anomaly, but to determine its source. A disturbance in TEC or VLF amplitude may arise from seismic preparation, cyclone-related gravity waves, lightning activity, geomagnetic forcing, meteorological variability, transmitter instability, local noise, or a mixed combination of these processes. Source attribution is therefore central to converting ionospheric observations into useful disaster-risk information.

IONGUARD develops a vertically integrated observational database in which GNSS/GPS total electron content and scintillation, VLF/LF transmitter-receiver propagation, ionosonde measurements, magnetometer data, low-Earth-orbit satellite plasma observations, thermal infrared and outgoing longwave radiation products, lightning occurrence, rainfall, cloud properties, meteorological reanalysis, cyclone tracks, earthquake catalogues, and GPS deformation fields are co-registered in space and time. Automated processing will generate TEC residual maps, TID and atmospheric-gravity-wave signatures, spatial coherence fields, VLF/LF day- and nighttime fluctuation indices, amplitude and phase perturbations, satellite plasma anomaly profiles, thermal anomaly fields, storm-forcing layers, and lightning-contamination masks. Each candidate anomaly

will be tagged with local time, geomagnetic condition, weather context, propagation-path geometry, and relevant hazard information, allowing the observational evidence to be evaluated within its physical environment rather than as an isolated signal.

A major advancement over conventional anomaly studies is the explicit physical-screening and exclusion stage. TEC disturbances will be tested against geomagnetic indices, solar-wind conditions, local-time behavior, spatial morphology, and AGW/TID propagation properties. VLF/LF anomalies will be checked for sunrise-sunset terminator effects, lightning along the propagation path, transmitter stability, day-night propagation regime, path sensitivity, and long-path modal effects. Thermal and OLR anomalies will be examined against cloud cover, rainfall, land-surface state, and synoptic meteorological conditions. These checks are intended to reduce false attribution and to distinguish hazard-related coupling from ordinary environmental or instrumental variability. The resulting analysis changes the guiding question from 'Was there an ionospheric anomaly?' to 'Which process generated the disturbance, through what coupling mechanism, and with what supporting evidence?'.

Machine-learning methods will be used in a constrained and interpretable role after physical screening. Candidate approaches include random forest, isolation forest, support vector machines, autoencoders, and temporal LSTM models for anomaly clustering, feature ranking, mixed-source separation, and confidence scoring. Inputs can include TEC residual magnitude, VLF fluctuation level, AGW spectral power, lightning density, rainfall intensity, geomagnetic state, satellite plasma deviation, and deformation proximity. Model outputs will be accepted only when they remain physically consistent with the observed pathway and environmental context. This design avoids dependence on black-box prediction and instead uses machine learning to organize complex multi-parameter evidence, quantify source likelihood, and identify combinations of signals that repeatedly occur under similar hazard conditions.

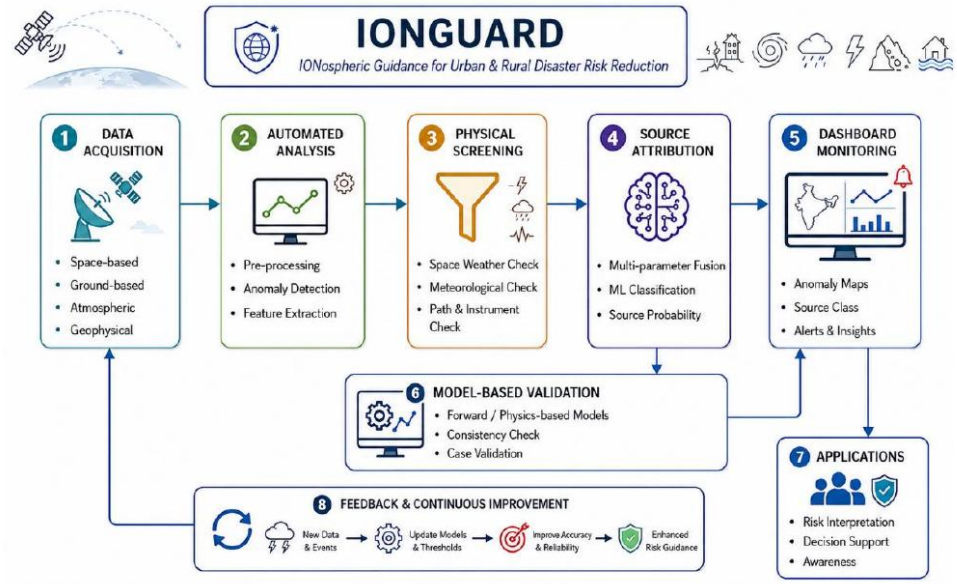


Figure 1. IONGUARD workflow for multi-source observation, automated anomaly extraction, physical screening, source attribution, model-based validation, dashboard monitoring, and continuous improvement.

The operational output is envisaged as a dashboard-type scientific monitoring and interpretation platform rather than a stand-alone alert generator. It will display TEC anomaly maps, VLF/LF disturbance indices, AGW/TID diagnostics, lightning and rainfall overlays, thermal anomaly layers, geomagnetic screening flags, satellite plasma tracks, and source-classification labels together with quality and confidence information. Such a platform can improve situational awareness for densely populated urban regions, rural

communities, cyclone-prone coastal sectors, and Himalayan or Northeast Indian mountain belts. The same architecture can support post-event analysis by tracing how a disturbance evolved from the source environment through the troposphere and middle atmosphere to the ionosphere, enabling systematic comparison between earthquakes, thunderstorms, cyclones, and space-weather episodes.

This framework's disaster-risk-reduction value lies in its emphasis on integration, reliability, scalability, and scientific interpretability. India already has substantial seismic, geodetic, meteorological, lightning, and satellite-data resources, and many required datasets are available from established national and international networks. IONGUARD therefore relies on intelligent fusion of existing observations, supplemented by durable, comparatively low-cost ground sensors where necessary, rather than a single expensive purpose-built infrastructure. This approach is particularly suitable for a country in which disaster exposure ranges from megacities and coastal corridors to remote rural and mountainous regions. It also provides a practical route for long-term monitoring because the same standardized analysis can be updated as new data, new event catalogs, and improved physical models become available.

In summary, IONGUARD advances disaster risk reduction by transforming ionospheric measurements from isolated anomaly indicators into a source-aware multi-hazard diagnostic system. The framework links observations across the lithosphere, atmosphere, and ionosphere; applies robust anomaly extraction and environmental screening; uses physically constrained multi-parameter fusion for source attribution; and delivers interpretable monitoring products suitable for scientific decision support. Its fundamental contribution is a better understanding of vertical Earth-system coupling under Indian geophysical conditions, while its applied contribution is a reproducible method to reduce false interpretation and strengthen evidence-based hazard monitoring. If validated across representative seismic, convective, cyclonic, and geomagnetic events, the approach can provide a scalable foundation for incorporating ionospheric observations into broader disaster-resilience strategies in India and other multi-hazard regions worldwide.

References

[1] K. Nanda, S. Sasmal, R. Hazra, A. Datta, P. Panchadhyayee, and S. M. Potirakis, “Study on the distribution of gravity wave (GW) activity in six Bay of Bengal tropical cyclones,” *Atmosphere*, vol. 16, Art. no. 235, 2025.

[2] K. Nanda, D. Mondal, S. Sasmal, Y. Hobara, A. K. Maurya, M. Hayakawa, S. M. Potirakis, and A. Datta, “Atmospheric impact of Typhoon Hagibis: A multi-layer investigation of stratospheric and ionospheric responses,” *Atmosphere*, vol. 17, Art. no. 167, 2026.

[3] Nanda, K., Brawar, B., Hayakawa, M., Hobara, Y., Potirakis, S.M., Maurya, A.K., Pandey, U., Datta, A. and Sasmal, S., “A Multi-Parametric Investigation of Seismogenic Signals: A Case Study of the 2018 Aomori Earthquake (Mw 6.2). Open Journal of Earthquake Research, 15, 11-38, 2026.

Milk Yield Variations in Dairy Cows and Earthquakes Previous Findings and Exploratory Lunar Phase Analysis

Hiroyuki Yamauchi
Earthquake Prediction Research Center, Tokyo, Japan

1. Background and previous findings

Continuous quantitative records are important for evaluating animal responses associated with earthquakes. Milk yield is a routinely recorded physiological and production indicator that permits long-term assessment. This presentation reviews previous findings and reports exploratory observations focusing on lunar phase and differences among farms.

A decrease in milk yield was observed 3–6 days before the 2011 Tohoku earthquake at a facility approximately 340 km from the epicenter [1]. An analysis of one year of records from a single farm in 2014 found that milk yield was negatively correlated with seismic activity occurring approximately three weeks later; a probability gain of 6.8 was obtained under one of the evaluated criteria [2]. Temporal relationships between milk yield and ultralow-frequency (ULF) magnetic field variations have also been examined [3]. For the 2021 northwestern Chiba earthquake, yield decreases differed in occurrence and timing among farms [4].

2. Milk yield indicator and observational methods

For the observations presented here, expected yield from a lactation curve was subtracted from each cow's daily yield. Heat effects were then adjusted where indicated by the relationship with the temperature-humidity index two days earlier. The mean of the preceding seven days of adjusted values was subtracted from each daily adjusted value, and these differences were averaged across cows with valid data at each farm. A low-yield day was defined as a farm-level value below the mean minus 1.5 standard deviations over the 31-day window including that day. Days with insufficient data were treated as missing. Relationships with new moons were examined retrospectively, using calendar dates in Japan Standard Time.

3. Observations in relation to lunar phase and farm location

Before the 1 January 2024 Noto Peninsula earthquake (M7.6), yield decreases at Matsumoto (approximately 155 km from the epicenter) occurred on 17–18 September, 15 October, 11–12 November, and 12–13 December 2023. Each interval fell within approximately three calendar days of a new moon (Fig. 1a). Yield decreases at Nasushiobara (approximately 246 km) on 21–22 December and at Fujinomiya (approximately 273 km) over 18–23 December occurred later than the 13 December new moon and approximately 9–14 days before the mainshock (Fig. 1b). At Matsumoto, a further decrease on 13–14 January 2024 occurred close to the 11 January new moon, after the mainshock (Fig. 1a). The locations of the three farms, the epicenter, and the GSI rectangular fault model are shown in Fig. 2.

4. Discussion and future validation

These observations motivate examination of lunar phase, recurrence, and differences in timing among farms. This case alone cannot determine whether farm differences reflect epicentral distance or farm-specific conditions. We discuss comparisons with the same farm in the corresponding months of the preceding year, farm-specific factors, replication in independent earthquake cases, and comparisons with electromagnetic observations to evaluate possible predictive utility.

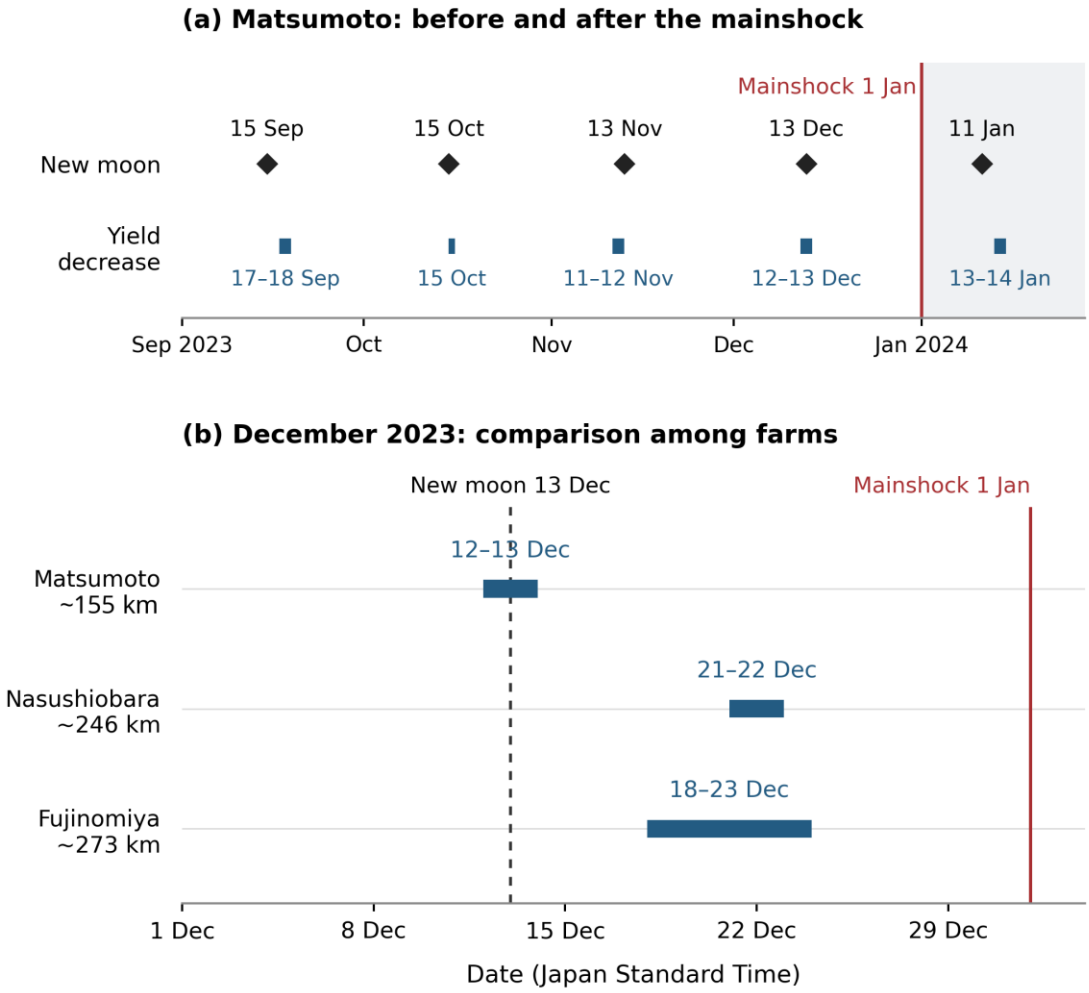


Figure 1. Selected low-yield periods and new moon dates around the Noto Peninsula earthquake. (a) Matsumoto: four periods before and one after the mainshock. Grey shading indicates the period after the mainshock. (b) Comparison among three farms in December 2023. Blue bars indicate the selected low-yield intervals; red lines mark the mainshock date. The Fujinomiya interval includes a temporary recovery. Distances are epicentral distances. The figure compares the timing of selected intervals; it does not show yield magnitudes or every low-yield day.

New moon dates (JST): National Astronomical Observatory of Japan, 2023 and 2024.

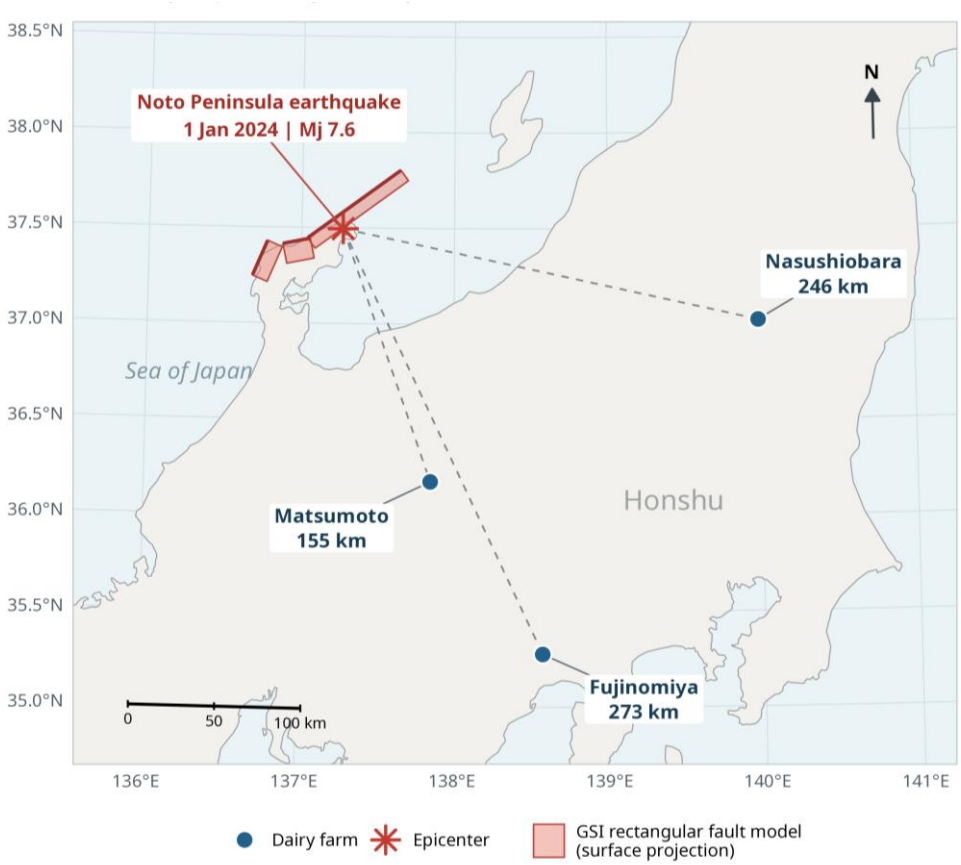


Figure 2. Locations of the three dairy farms, the epicenter, and the surface projection of the three-plane rectangular fault model estimated by the Geospatial Information Authority of Japan (GSI) [5]

References

[1] H. Yamauchi, H. Uchiyama, N. Ohtani, and M. Ohta, "Unusual Animal Behavior Preceding the 2011 Earthquake off the Pacific Coast of Tohoku, Japan: A Way to Predict the Approach of Large Earthquakes," Animals, vol. 4, pp. 131–145, 2014. doi: 10.3390/ani4020131

[2] H. Yamauchi, M. Hayakawa, T. Asano, N. Ohtani, and M. Ohta, "Statistical Evaluations of Variations in Dairy Cows' Milk Yields as a Precursor of Earthquakes," Animals, vol. 7, article 19, 2017. doi: 10.3390/ani7030019

[3] M. Hayakawa, T. Asano, A. Schekotov, and H. Yamauchi, "A Study on the Correlation of Milk Yield of Cows with Seismicity and ULF Magnetic Field Variations," Open Journal of Earthquake Research, vol. 5, pp. 206–218, 2016. doi: 10.4236/ojer.2016.54017

[4] M. Hayakawa and H. Yamauchi, "Unusual Animal Behavior as a Possible Candidate of Earthquake Prediction," Applied Sciences, vol. 14, article 4317, 2024. doi: 10.3390/app14104317

[5] H. Suito, H. Munekane, and M. Kuwahara, "Fault Model of the 2024 Noto Peninsula Earthquake," Journal of the Geospatial Information Authority of Japan, no. 138, pp. 33–38, 2024. doi: 10.57499/JOURNAL_138_05

Water vapor lidar observations of moisture transport into mesoscale convective systems in western Japan

Satoru Yoshida [1], Masahide Nishihashi [2], and Tetsu Sakai [2]
[1]Chiba University, Chiba, Japan
[2]Meteorological Research Institute, Tsukuba, Japan
Corresponding author: syoshida@chiba-u.jp

This presentation summarizes our recent studies and ongoing projects in water vapor lidar observations of moist low-level jets (MLLJs) into mesoscale convective systems (MCSs) over western Japan. Water vapor Raman lidar observations successfully captured detailed vertical moisture structures associated with heavy rainfall events in Kyushu. A case study on 9 July 2021 revealed enhanced low-level moisture within an MLLJ that contributed to the development of a back-building MCS, while data assimilation experiments demonstrated improved rainfall forecasts through the incorporation of lidar-derived moisture profiles. Observations on 14 July 2022 further identified a slant structure of almost saturated atmosphere and weak updrafts that supported sustained convective development. In addition, ongoing projects involving shipborne and compact water vapor differential absorption lidar systems are introduced, highlighting advances toward improved monitoring moisture structure and prediction of heavy rainfall.

1. Introduction

During rainy season in Japan, stationary fronts often appear around Japan, especially western Japan. These fronts are characterized by southerly or southwesterly moist low-level jet (MLLJ). The MLLJ sometimes triggers mesoscale convective systems (MCSs), consisting of a lot of thunderstorms. These MCSs are accompanied by heavy rainfall, occasionally causing heavy damage on our society. Improvement of forecast skill for these heavy rainfalls is essential for both our society and scientific field. Since the MLLJ fuels large amount of moisture into the MCS, understanding of moisture vertical structures of the MLLJ and data assimilation of the moisture structures are one of the important approaches to improve the forecast skills for heavy rainfalls associated with MCSs. We have been developing water vapor lidar systems, conducting observation campaigns in the west side of Kyushu, and performing data assimilation experiments. In this paper, we will show our research [1, 2] and ongoing projects.

2. Water vapor Raman lidar

We developed a water vapor Raman lidar (RL) that measure the vertical distribution of water vapor in the lower atmosphere [3]. The RL consists of an Nd:YAG laser, a beam expander, a 35-cm-diameter telescope, interference filters, photomultiplier tubes, and a digitizer. It emits vertically directed laser pulses at 355 nm and receives backscattered signals from aerosols at 355 nm (elastic scattering) and water vapor and nitrogen molecules at 407.5 nm (H_2O Raman) and 386.7 nm (N_2 Raman). Water vapor mixing ratio (WVMR) is retrieved from the ratio of H_2O to N_2 Raman signals. The observation range extends from approximately 200 m to 5 km altitude at night and to 2 km during daytime, with the reduced daytime range resulting from solar background radiation. The temporal resolution is 20 min. Two RL systems were deployed at Nomozaki, Nagasaki Prefecture, and Koshiki, Kagoshima Prefecture, from 2020 to 2022. Validation of RL-observed data with radiosonde observations showed the WVMR differences of less than 0.9 g kg^{-1} during nighttime observations [4].

3. A case study of 9 July 2021

On 9 July 2021, a stationary front extending from China to Japan produced a back-building MCS over southern Kyushu, resulting in heavy rainfall with a maximum 9-h accumulated rainfall of 585 mm. The RLs at Nomozaki and Koshiki succeeded in continuously observing the vertical profiles of WVMR (Figure 1).

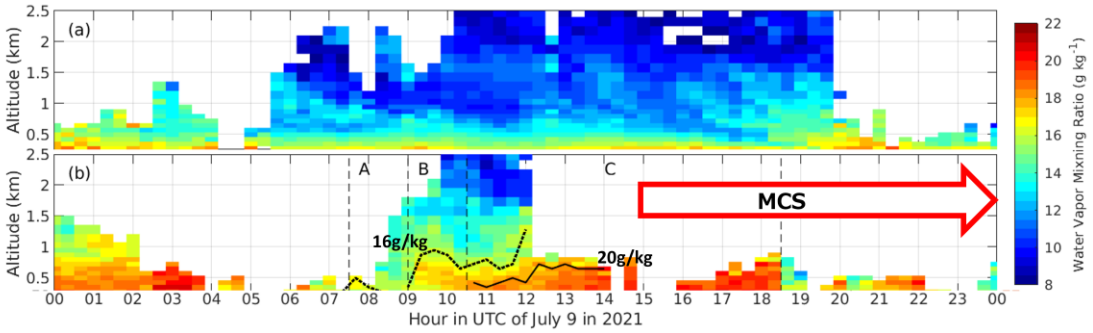


Figure 1: Vertical profiles of WVMR obtained with the RLs at (a) Nomozaki and (b) Koshiki on July 9.

The observations revealed a pronounced low-level moisture contrast prior to and during the onset of the MCS at Koshiki (between 09 UTC and 18 UTC). WVMR within the moist low-level jet (MLLJ) at Koshiki was substantially higher than that at Nomozaki between 0.2 and 1.6 km MSL. The mean WVMR differences between the two sites reached approximately 5 g kg^{-1} in this layer, whereas differences above 2 km MSL are about 2 g kg^{-1}, which is smaller than those in low-level. Operational radiosonde observation at 12 UTC at Kagoshima indicated that the convective mixing layer height (CMLH) was about 1.6-1.9 km MSL, suggesting that the enhanced moisture associated with the MLLJ was concentrated below the CMLH. These results demonstrate that a large amount of water vapor was confined to the lower troposphere within the MLLJ and likely provided the moisture supply for the development and maintenance of the MCS.

To evaluate the impact of the lidar observations on rainfall forecasts, a series of data assimilation experiments was conducted using the Japan Meteorological Agency's forecast and data assimilation system. Experiments assimilating the WVMR observations modified the moisture distribution near the MLLJ, strengthened the low-level convergence, and shifted the forecast rainfall area southward relative to the control experiment. As a result, the location of heavy rainfall became closer to observations. In addition, the forecasts with WVMR assimilation produced basically larger 9-h accumulated rainfall amounts and reduced errors in both rainfall intensity and location, although rainfall was still underestimated (Figure 2).

These results demonstrate that water vapor lidar observations can successfully capture the moisture structure of an MLLJ and that assimilation of the observed moisture profiles improves forecasts of heavy rainfall associated with MCSs.

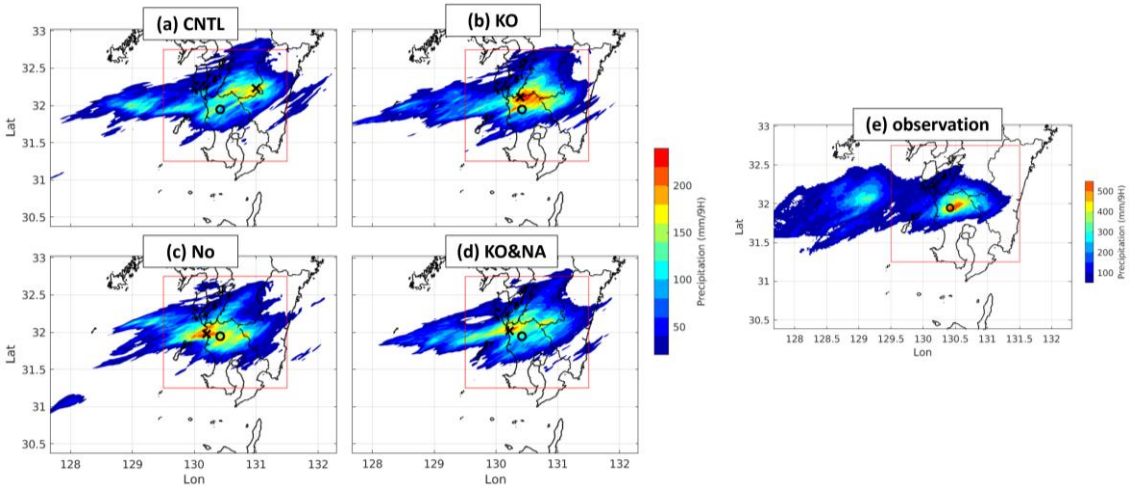


Figure 2: Nine hour accumulated rainfalls. (a-d) assimilation results. (a) No WVMR data from lidar is assimilated (CNTL). (b) WVMR data at Koshiki was assimilated (Ko). (c) WVMR data at Nomozaki is assimilated (No). (d) WVMR at both Koshiki and Nomozaki was assimilated (Ko&No). (e) radar-rain gaged analysis data. Cross and circle symbols indicate the locations of the highest 9-hour rainfall in the simulations and observations, respectively. Adapted from Yoshida et al. [1].

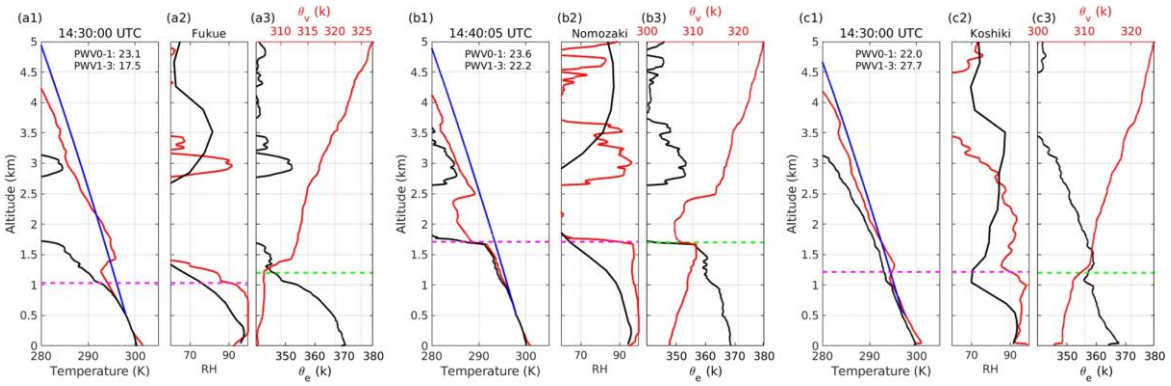


Figure 3: Vertical profiles from radiosonde observations at Fukue, Nomozaki, and Koshiki around 14:30 UTC on 14 July 2022, including temperature, humidity, and thermodynamic parameters (θ_e: equivalent potential temperature, θ_v: virtual temperature). Magenta and green dashed lines indicate RH90H and the convective mixing layer height, respectively. PWV values are also shown. Adapted from Yoshida et al. [2].

4. A case study of 14 July 2022

On 14 July 2022, a back-building MCS formed over southern Kyushu and produced more than 320 mm of rainfall in 6 hours. To investigate the moisture structure associated with the MCS, radiosonde observations were conducted every three hours at Fukue, Nomozaki, and Koshiki, together with the RL and Doppler lidar observations. The observation sites were located within a moist low-level jet (MLLJ) transporting moisture toward the MCS.

Figure 3 shows vertical profiles of relative humidity (RH), parcel temperature, and virtual potential temperature obtained around 14:30 UTC on 14 July 2022, prior to the onset of the MCS. Deep moist layers with RH exceeding 90% were observed at all sites. We defined RH90H as the altitude below which RH remained greater than 90%, representing the depth of the moist layer. Negative vertical gradients of equivalent potential temperature below the RH90Hs indicated potential instability. Nevertheless, parcels released from 500 m ASL reached their levels of free convection with little lifting but obtained only weak buoyancy because parcel and environmental temperatures were nearly identical below the RH90Hs. Despite the exceptionally moist lower troposphere, the environmental air was nearly as moist as the parcels, limiting buoyancy generation during ascent.

Figure 3 also reveals the vertical extension of moist absolute unstable layers (MAULs) at all observation sites. Comparisons between Fukue and Nomozaki show that both RH90H and the convective mixing layer height increased toward the MCS, indicating that the moist layer gradually deepened downstream and formed a slanted structure. Similar moist layers and MAULs were simultaneously observed at Nomozaki and Koshiki, implying a horizontal extent exceeding 80 km across the MLLJ. Doppler lidar observations at Koshiki further detected weak updrafts below cloud base, with slope angles comparable to that of the slanted moist layer. These observations suggest that persistent weak updrafts transported moisture upward and contributed to the formation and maintenance of the sloping moist layer.

The results indicate that the MCS was occasionally sustained by a broad, slantwise-rising moist layer within the MLLJ, which efficiently supplied moisture to the convective system and supported the occurrence of localized heavy rainfall.

5. Ongoing projects

Following the successful the RL observations, we have launched two projects related to water vapor lidars development and observations. Here, we introduce these two projects.

The first project is that we have been developing a compact diode-laser-based water vapor differential absorption lidar (DIAL), which has lower maintenance costs and can measure higher altitudes during the day than conventional RLs. The DIAL system employs alternating on-line (829.054 nm) and off-line (829.124 nm) wavelengths generated by distributed Bragg reflector laser diodes and amplified by a tapered semiconductor optical amplifier. Recent developments have

focused on increasing receiver transmittance, stabilizing transmitted laser power, improving wavelength control, and simplifying adjustment procedures. These improvements have enhanced operational stability and increased the observable altitude range. Field campaigns were conducted at Nomozaki during the summers of 2025 and 2026. Despite occasional operational issues, the DIAL operated stably for nearly three months. During several MCS events in August 2025, the system continuously detected high water vapor concentrations in the lower troposphere, consistent with mesoscale analysis data. Water vapor profiles were sometimes obtained up to an altitude of 2.5 km under clear-sky conditions.

The second project is to obtain longer forecast lead times for moisture transport from the ocean to the land, we are also conducting demonstration experiments with a ship-based coherent DIAL system (Figure 4) that simultaneously measure vertical profiles of water vapor and wind. Validation observations were conducted during seven cruises over the northwestern and tropical Pacific Oceans in 2024-2025. Comparisons with collocated radiosonde observations showed good agreement for both water vapor mixing ratio and wind profiles within the observation range between 0.2 and 1 km. Comparisons with the Japan Meteorological Agency Local Analysis also confirmed that the DIAL successfully captured temporal variations in lower-tropospheric moisture and wind fields.

6. Summary

Water vapor Raman lidar observations successfully revealed the vertical moisture structure of MLLJs associated with heavy rainfall events over Kyushu. Data assimilation experiments demonstrated that WVMR observations improved forecasts of rainfall. Radiosonde and lidar observations further revealed a broad sloping moist layer and weak updrafts that contributed to MCS development. Based on these results, compact ground-based and ship-based DIAL systems have been developed and deployed to expand moisture observations and improve heavy-rainfall forecasts.

Acknowledgment

This work was supported in part by a Grant-in-Aid from JSPS KAKENHI (Grants 22H00250 and 25H00697).

References

[1] S. Yoshida et al., “Observation of a slanted moisture structure with weak updraft leading to localized heavy rainfalls”, *Sci. Rep.*,**15**, 22979, 2025.

[2] S. Yoshida et al., “Water vapor lidar observation and data assimilation for a moist low-level jet triggering a mesoscale convective system”, *Mon. Wea. Rev.*, **152**, 1119–1137, 2024.

[3] T. Sakai et al, “Automated compact mobile Raman lidar for water vapor measurement: instrument description and validation by comparison with radiosonde, GNSS, and high-resolution objective analysis”, *Atmos. Meas. Tech.,* **12***,* 313–326., 2019.

[4] S. Yoshida et al., “Accuracy evaluation of water vapor mixing ratios obtained from water vapor Raman lidars and local analysis data”, *Journal of Laser Radar Society of Japan*, **6**, 1, 2-13, 2025.



Figure 4: Coherent DIAL (red circle) on the Research vessel Mirai. Overview of the vessel (left). Inside of lidar container (right).

Observational Insights into Lightning-Rainfall Coupling and Convective Evolution in Severe Thunderstorms

Debrupa Mondal[1,2], Yasuhide Hobara[2,3,4], Hiroshi Kikuchi[3], Jeff Lapierre[5]
[1]Indian Institute of Tropical Meteorology, Pune, India
[2]Graduate School of Information and Engineering, University of Electro-Communications, Chofu, Japan
[3]Center for Space Science and Radio Engineering, University of Electro-Communications, Chofu, Japan
[4]Research Center for Realizing Sustainable Societies, University of Electro-Communications, Chofu, Japan
[5]Advanced Environmental Monitoring, Germantown, MD, USA
Corresponding author: debrupamondaljam@gmail.com

In recent years, extreme weather events associated with heavy rainfall and severe convection have become an increasing global societal concern, with floods, landslides, and lightning causing substantial human and economic losses. According to the World Meteorological Organization, weather-related disasters have increased fivefold over the past 50 years, resulting in more than 2 million deaths and economic losses totaling approximately 400 trillion yen. These increasing impacts highlight the need for improved understanding of convective development and high-resolution monitoring of severe weather events. Previous studies by our group demonstrated a strong correlation (R=0.92) between IC activity and torrential rainfall (maximum intensity >100mm/h) in isolated and multicellular convective cells, with IC peaks preceding rainfall maxima by approximately 10 minutes [1,2]. A moving linear regression model demonstrated the potential for early warning and accurate nowcasting (correlation between actual and predicted rainfall reaching 0.94) of heavy rainfall using IC pulse rate [2]. Automatic convective cell identification and tracking using AITCC method further revealed a close spatio-temporal correspondence between lightning-frequent regions and rainfall cells, particularly during the mature stage of isolated convective systems [3]. Building upon these findings, the present study provides an observational overview of the relationship between total lightning activity and heavy rainfall in summer thunderstorms, with observations from Japan extended to preliminary case studies over India. In particular, this work also presents results from Eastern India, focusing on the co-evolution of atmospheric electric field, total lightning activity, and rainfall during premonsoon thunderstorm events in West Bengal.

References

[1] D. Mondal, Y. Hobara, H. Kikuchi, J. Lapierre, “Thunderstorms and Total Lightning Characteristics Causing Heavy Precipitation in Japan: A Case Study”, Radio Science Bulletin, 378, P. 70-76, Sept 2021

[2] D. Mondal, Y. Hobara, H. Kikuchi, J. Lapierre, P.L. Floch, O. Kameya, N. Kawaguchi, K. Motojima, K. Shiokawa, T. Eguchi, D. Okano, T. Nakamura, “Temporal Dependencies Between Total Lightning and Rainfall in Multicellular Systems: A Predictive Approach for Torrential Rain during Summer Thunderstorms in Japan”, Radio Science, 61, 2026

[3] D. Mondal, Y. Hobara, H. Kikuchi, J. Lapierre, “Assessing the Potential of Total Lightning for Nowcasting Ground Rainfall in Summer Thunderstorms Using Automatic Density-Dependent Tracking”, Atmosphere, 17(4), 364, 2026

Atmospheric Gravity Waves Excited by Convective Weather Systems

Shih-Sian Yang [1,2,3], Yasuhide Hobara [4,5,6], Sudipta Sasmal [2,3,7], Stelios M. Potirakis [8], and Masashi Hayakawa [2,3,9]

[1]Solar Sharing, Co. Ltd., Jhongli, Taoyuan City 320953, Taiwan
[2]Hayakawa Institute of Seismo Electromagnetics, Co., Ltd. (Hi-SEM), Chofu, Tokyo 182-0026, Japan
[3]QuakeInsight Tokyo, Chofu, Tokyo 182-0026, Japan
[4]Graduate School of Informatics and Engineering, The University of Electro-Communications (UEC), Chofu, Tokyo 182-8585, Japan
[5]Center for Space Science and Radio Engineering, UEC, Chofu, Tokyo 182-8585, Japan
[6]Research Center for Realizing Sustainable Societies, UEC, Chofu, Tokyo 182-8585, Japan
[7]Institute of Astronomy Space and Earth Science, Kolkata 700054, India
[8]Department of Electrical and Electronics Engineering, University of West Attica, 12241 Athens, Greece
[9]Advanced Wireless and Communication Research Center (AWCC), UEC, Chofu, Tokyo 182-8585, Japan
Corresponding author: yang.sirius.sian@gmail.com

Atmospheric gravity waves (AGWs) play an important role in atmospheric energy and momentum exchange. Convective weather systems are a main source of AGW excitation. In this study, we analyzed the stratospheric and lower mesospheric AGW activity excited by extreme convective systems, such as typhoons, extratropical cyclones, frontal systems, and mesoscale convection. We also used the very low frequency (VLF) data observed in Taiwan to investigate AGWs excited by two typhoons, as they passed across the VLF propagation path between Kyushu and Taiwan. Simultaneous observations of the atmosphere and ionosphere provide us with a hint of the coupling process between the atmosphere and the ionosphere through AGWs. By studying AGW spatio-temporal characteristics, we better understand how convective weather systems affect the upper atmosphere and ionosphere.

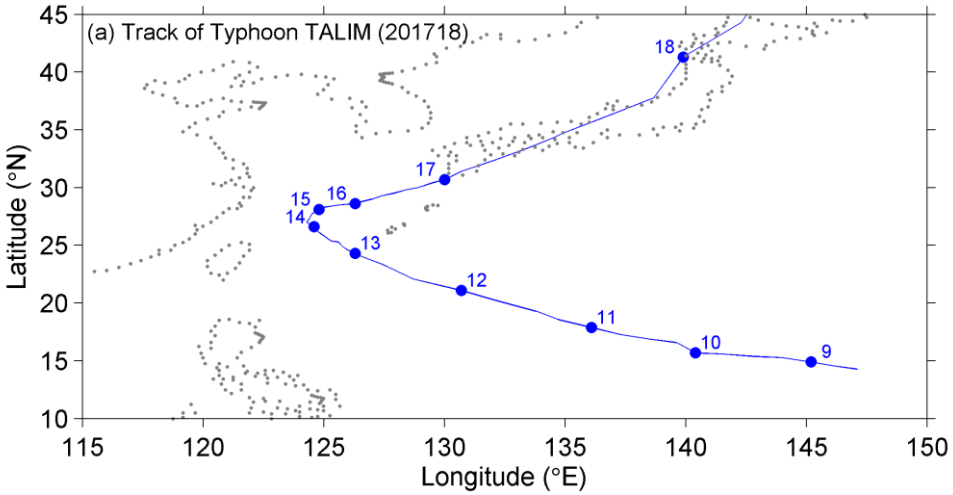


Figure 1. The track of Typhoon Talim (international ID: 201718). The blue circles indicate the locations of the typhoon center at 00Z on each day in September 2017.

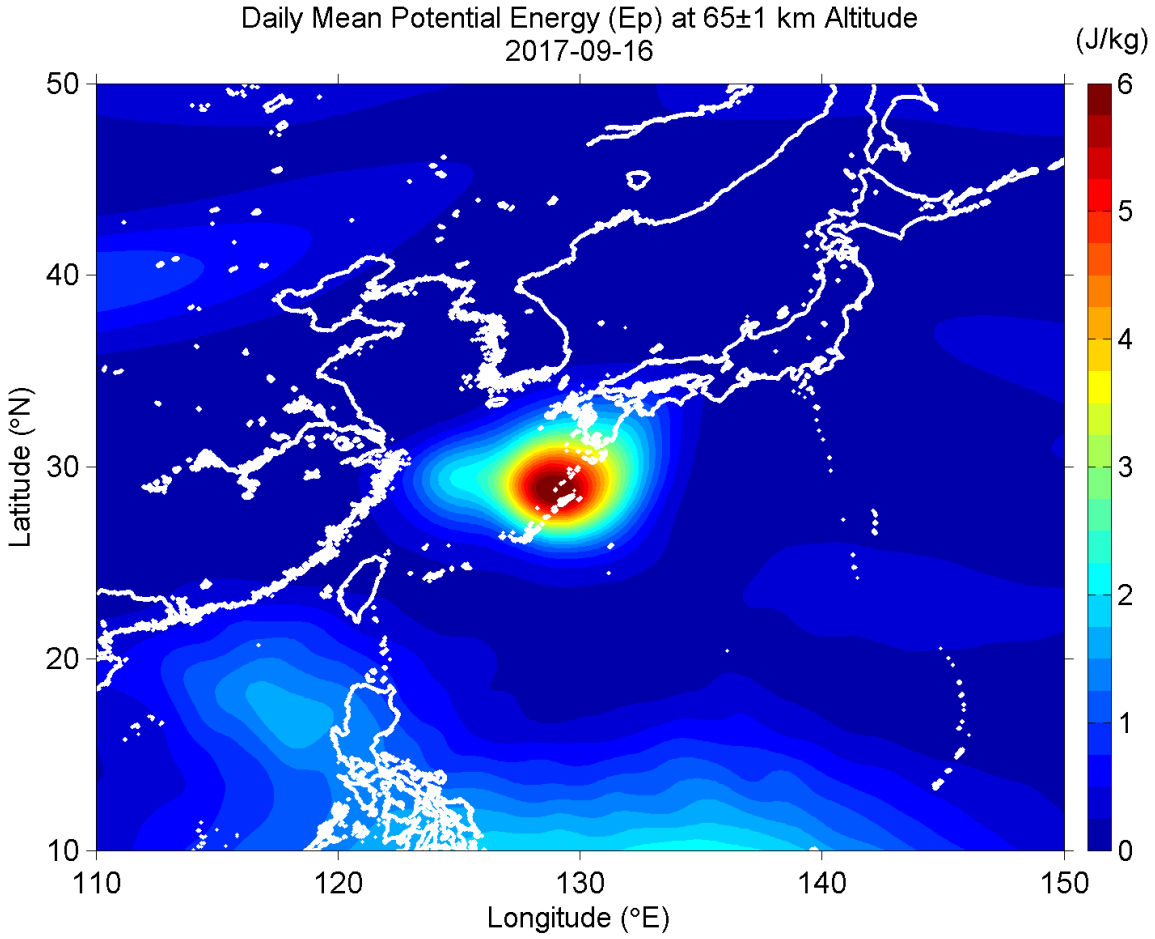


Figure 2. The atmospheric gravity wave (AGW) potential energy (E_P) at 65 km altitude on 16 December 2017. Strong AGW activity was found above Typhoon Talim.

Advanced Disaster Resilience via Lightning Observations: Multi-Scale Prediction of Heavy Rainfall and Spatiotemporal Mapping of High-Charge Flashes

Y. Hobara[1,2,3,4] and H. Kikuchi[3]

[1] Graduate School of Informatics and Engineering, The University of Electro-Communications (UEC), Japan
[2] Earth Environment Research Station, UEC, Japan
[3] Center for Space and Radio Engineering (SSRE), UEC, Japan
[4] Research Center for Realizing Sustainable Societies, UEC, Japan
Corresponding author: hobara@ee.uec.ac.jp

Extreme meteorological events, particularly line-shaped precipitation bands causing flash floods and landslides, pose growing threats under global climate change. Enhancing predictive capabilities with multi-scale lead times and monitoring high-energy lightning events are crucial for disaster resilience. This study presents an integrated framework combining lightning observations, GNSS water vapor data, atmospheric parameters, and Extremely Low Frequency (ELF) magnetic fields to investigate heavy rainfall dynamics and lightning electrical characteristics.

To improve short-term to half-day forecasts of heavy precipitation, including line-shaped bands in Japan, we analyze spatiotemporal relationships among cloud lightning (IC), cloud-to-ground lightning (CG), precipitable water vapor (PWV from GEONET), convective parameters (CAPE from ERA5), and rainfall radar data (XRAIN). Statistical and tracking analyses show that IC activity detected by the Japan Total Lightning Network (JTLN)/ LF lightning location system (deployed over the Kanto and Kyushu area) precedes heavy ground precipitation by 5–10 minutes, serving as a rapid indicator of convective development. On longer timescales, atmospheric parameters and spatial lightning distributions several hours prior exhibit strong morphological alignment with forming precipitation bands. By integrating these multi-source data into machine learning models, we help establish an advanced predictive system that forecasts severe rainfall events from immediate nowcasting (minutes) to half-day lead times.

Additionally, we evaluate the electrical properties of severe lightning—specifically high charge moment changes (Qds) and peak currents (Ip)—which cause major power grid failures and severe hazards. Utilizing ELF magnetic field observations and lightning network data, we mapped the spatiotemporal and seasonal distributions of these high-energy flashes during winter lightning in Japan and across Southeast Asia. The results reveal significant regional and diurnal variations in Qds and Ip, providing crucial insights into convective structures and lightning generation mechanisms under varying meteorological conditions.

By unifying rapid lightning nowcasting, machine-learning-based precipitation forecasting, and severe lightning hazard mapping, this comprehensive observational framework bridges radio and atmospheric physics with practical disaster prevention, supporting early warning systems and infrastructure protection.